

University of Alberta

Influence of tunnel jet-grouting on ground deformations at the  
Aeschertunnel, Switzerland

by

Steven Ninian Patrick Coulter



A thesis submitted to the Faculty of Graduate Studies and Research in partial  
fulfillment of the

requirements for the degree of Master of Science

in

Geotechnical Engineering

Department of Civil and Environmental Engineering

Edmonton, Alberta

Fall 2004



Library and  
Archives Canada

Bibliothèque et  
Archives Canada

Published Heritage  
Branch

Direction du  
Patrimoine de l'édition

395 Wellington Street  
Ottawa ON K1A 0N4  
Canada

395, rue Wellington  
Ottawa ON K1A 0N4  
Canada

*Your file* *Votre référence*

*ISBN: 0-612-95728-4*

*Our file* *Notre référence*

*ISBN: 0-612-95728-4*

The author has granted a non-exclusive license allowing the Library and Archives Canada to reproduce, loan, distribute or sell copies of this thesis in microform, paper or electronic formats.

L'auteur a accordé une licence non exclusive permettant à la Bibliothèque et Archives Canada de reproduire, prêter, distribuer ou vendre des copies de cette thèse sous la forme de microfiche/film, de reproduction sur papier ou sur format électronique.

The author retains ownership of the copyright in this thesis. Neither the thesis nor substantial extracts from it may be printed or otherwise reproduced without the author's permission.

L'auteur conserve la propriété du droit d'auteur qui protège cette thèse. Ni la thèse ni des extraits substantiels de celle-ci ne doivent être imprimés ou autrement reproduits sans son autorisation.

---

In compliance with the Canadian Privacy Act some supporting forms may have been removed from this thesis.

Conformément à la loi canadienne sur la protection de la vie privée, quelques formulaires secondaires ont été enlevés de cette thèse.

While these forms may be included in the document page count, their removal does not represent any loss of content from the thesis.

Bien que ces formulaires aient inclus dans la pagination, il n'y aura aucun contenu manquant.

# Canada

## **ACKNOWLEDGEMENTS**

I would like to thank my parents, Terence and Vanessa for their support throughout my education, and in particular during my master's studies. Thanks to my supervisor, Dr C. Derek Martin, for the help and advice in the development of ideas that were used in this thesis. Also, I would like to acknowledge the funding provided by NSERC. Thanks to my friends for believing in me, and to everyone who challenged me during my university education.

# TABLE OF CONTENTS

<b>1</b>	<b>INTRODUCTION .....</b>	<b>1</b>
	1.1 Objective .....	2
	1.2 Scope .....	2
	1.3 Outline of Thesis Content .....	2
<b>2</b>	<b>LITERATURE REVIEW .....</b>	<b>4</b>
	2.1 Soft Ground Tunneling.....	4
	2.1 Response of silty and dense sands to tunneling.....	9
	2.2 Jet-grouting.....	12
	2.2.1 Factors affecting the size of jet-grout columns .....	13
	2.2.1 Composition of jet-grout & soil mixture .....	16
	2.2.2 Properties of jet-grout.....	17
	2.3 Portland Cement .....	20
	2.3.1 Chemistry .....	20
	2.3.2 Hydration Process.....	22
	2.3.3 Material Behavior .....	24
	2.4 Summary .....	26
<b>3</b>	<b>Laboratory Testing of Jet-grout Properties.....</b>	<b>28</b>
	3.1 Mix Design.....	28
	3.2 Grout Mixing & Casting Procedure .....	29
	3.2.1 Cylinder Design.....	29
	3.2.2 Insulation Design.....	30
	3.3 Tests Performed .....	34
	3.3.1 Shear Vane Tests .....	34
	3.3.2 Uniaxial Compression .....	34
	3.3.3 Tensile Strength.....	35
	3.3.4 Residual Strength.....	36
	3.4 Testing results .....	37
	3.4.1 Unconfined Compressive Strength.....	37
	3.4.2 Tensile Strength.....	39
	3.4.3 Failure Envelope.....	41
	3.4.4 Young's Modulus .....	41
	3.4.5 Heat of Hydration .....	45
	3.4.6 Residual Strength.....	49
	3.4.7 Vane Shear Tests .....	50
	3.4.8 Grout Density .....	50
	3.5 Summary .....	51

<b>4</b>	<b>Aeschertunnel .....</b>	<b>53</b>
	<i>4.1 Geology.....</i>	<i>56</i>
	4.1.1 Bedrock.....	56
	4.1.2 Till .....	57
	4.1.3 Surficial layer .....	58
	<i>4.2 Instrumentation.....</i>	<i>59</i>
	<i>3.3 Construction Methods.....</i>	<i>62</i>
	4.3.1 Rock.....	62
	4.3.2 Fill area .....	62
	4.3.3 Glacial till .....	62
	4.3.3.1 Blade Shield .....	63
	4.3.3.2 Jet-Grout.....	64
	<i>4.4 Observations During Tunnel Construction.....</i>	<i>70</i>
	4.4.1 Blade Shield Tunneling .....	70
	4.4.2 Jet-Grout Over-pressurization .....	72
	4.4.3 Observed settlements when using the jet-grout technique .....	73
	<i>4.5 Summary .....</i>	<i>79</i>
<b>5</b>	<b>Analysis of Surface Settlements over the Aeschertunnel.....</b>	<b>80</b>
	<i>5.1 Back Analysis Techniques.....</i>	<i>81</i>
	<i>5.2 Empirical Analysis.....</i>	<i>83</i>
	<i>5.3 Numerical Analysis.....</i>	<i>88</i>
	5.3.1 Factors affecting the width of the settlement trough in a FEM.....	92
	5.3.2 Elastic Analysis .....	93
	5.3.3 Elastic Plastic Analysis.....	96
	5.3.4 Effect of reduction in softening area on trough width.....	99
	5.3.5 Elevated grout pressures in excess of overburden.....	101
	5.3.6 Elevated grout pressures & strain softening soil model .....	105
	<i>5.4 Evaluation of the liner loads.....</i>	<i>116</i>
	<i>5.6 Summary .....</i>	<i>119</i>
<b>6</b>	<b>Conclusions and Recommendations .....</b>	<b>121</b>
	<i>6.1 Conclusions.....</i>	<i>121</i>
	<i>6.2 Recommendations .....</i>	<i>123</i>
	6.2.1 Future research .....	124
<b>7</b>	<b>Bibliography.....</b>	<b>125</b>
<b>A.</b>	<b>APPENDIX Aeschertunnel Field Investigation.....</b>	<b>133</b>
<b>B.</b>	<b>APPENDIX Laboratory testing of grout .....</b>	<b>142</b>

**C. APPENDIX Numerical modeling ..... 146**

## LIST OF FIGURES

Figure 2.1 - Typical centerline settlement development .....	5
Figure 2.2 - 3D distribution of tunneling induced settlements.....	6
Figure 2.3 – Typical overlapping forepoles used to provide support over the tunnel face.	8
Figure 2.4 - Behavior of dense soil ( $N > 30$ ) above ground water level, modified from Heuer (1987).....	10
Figure 2.5. - Groutability of soils .....	12
Figure 2.6 - Jet-grouting procedure.....	13
Figure 2.7 - Soil erodibility as a function of soil type .....	15
Figure 2.8 - Relationship between uniaxial compressive strength (UCS) and water to cement ratio, by weight, data from Kauschinger (1992).....	18
Figure 2.9 - Relationship between unconfined compressive strength and Young's modulus for single fluid jet-grout, data from Kauschinger (1992) .....	19
Figure 2.10. - Strength of Portland cement constituents, data from Bye (1983) .....	21
Figure 2.11. - Heat generation rate for normal Portland cement (Taylor 1990) .....	23
Figure 3.1 - Grout cylinder design .....	30
Figure 3.2 - Unconfined compressive strength (UCS) of grout as a function of time .....	37
Figure 3.3 - Grout cylinders after unconfined compression testing.....	38
Figure 3.4 - Tensile strength of grout with time .....	39
Figure 3.5 - Relationship between tensile strength and unconfined compressive strength for grout.....	40
Figure 3.6 - Grout specimen after tensile testing .....	40
Figure 3.7. - Mohr-Coulomb failure envelope for grout .....	41
Figure 3.8 - Young's modulus of grout as a function of time.....	42
Figure 3.9 - Relationship between strength and stiffness .....	43
Figure 3.10 - Typical grout stress-strain curves for grout aged 10.3 hours or less .....	44
Figure 3.11 - Typical grout stress-strain curves for grout aged 10.3 hours or more.....	44
Figure 3.12 - Grout temperature change with time.....	45
Figure 3.13 - Rate of heat generation of grout due to cement hydration .....	46

Figure 3.14 - Rate of grout temperature change of grout.....	47
Figure 3.15 - Comparison between total heat generation and UCS .....	48
Figure 3.16. - Early strength development of grout measured with the vane shear test. ..	50
Figure 3.17. - Density of grout samples .....	51
Figure 4.1 - Aeschertunnel route.....	53
Figure 4.2 - Aeschertunnel profile .....	54
Figure 4.3. - Tunnel profile of the Basel and Luzern axes in the region of Aesch .....	55
Figure 4.4 - Excavation of the tunnel face showing the till .....	57
Figure 4.5 - Grain size distribution from the Eggraintunnel (Kleboth 2000) .....	58
Figure 4.6 - Location of convergence points .....	59
Figure 4.7 - Plan view of the settlement points in the vicinity of the Tantenholz portal ..	60
Figure 4.8 - Plan view of the settlement points in the vicinity of Aescherbach.....	61
Figure 4.9 - Tantenholtz portal (Southeast) showing tangent pile wall .....	63
Figure 4.10 - Blade shield use in heading excavation.....	63
Figure 4.11 - Jet-grouting installation in the tunnel heading .....	64
Figure 4.12 - Tunnel profile using jet-grout technique .....	65
Figure 4.13 - Tunnel cross section using jet-grout technique. ....	65
Figure 4.14 - Lattice girders prior to installation .....	66
Figure 4.15 - Jet-grout installation sequence for Luzern profiles 1 & 2 .....	67
Figure 4.16 - Jet -grout installation sequence for Basel profiles 1 & 2 .....	68
Figure 4.17 - Development of shotcrete uniaxial compressive strength (UCS) with time	69
Figure 4.18 - Settlement profile along the centerline using the blade shield at Luzern tunnel meter 74.....	71
Figure 4.19 - Settlement profile along the centerline using blade shield & jet-grout at Luzern tunnel meter 142.....	72
Figure 4.20. - Centerline settlement development – Profiles 1 and 2 .....	74
Figure 4.21 - Settlement Development 12m North of Basel axis .....	74
Figure 4.22 - Settlement and heave measured at the profile 12m South of Basel axis. The heave was coincident with the installation of jet-grout. ....	75
Figure 4.23 - Settlement development 20m South of Basel axis. ....	76



Figure 4.24 - Settlement development 32m South of Basel axis (Centerline Luzern axis)	76
.....	
Figure 4.25 Settlement development 12m South of Luzern axis	77
Figure 4.26 - Convergence – Luzern tunnel meter 1020	78
Figure 4.27 - Convergence – Basel tunnel meter 998	78
Figure 5.1 - Gaussian curve used to describe the settlement trough	84
Figure 5.2 - Failure mechanisms observed in centrifuge model tests of a tunnel in clay and sand (Mair 1997)	85
Figure 5.3 - The effect of a pre-vault observed in centrifuge tests of a tunnel in sand	85
Figure 5.4 - Observed vs. empirical fit settlements for Basel profiles 1 and 2	87
Figure 5.5 - Typical Phase2 model showing material properties and jet-grout installation sequence	90
Figure 5.6. - Trough width overestimation with FEM in sand overlying clay Modified from Stallebras (1996)	92
Figure 5.7 – The finite element grade triangular mesh used in the elastic analysis	94
Figure 5.8 - Modeled vs. measured settlements for Basel profile 2, elastic model	95
Figure 5.9 - Elastic model convergence	96
Figure 5.10 - Mesh used in the elastic-plastic analysis	97
Figure 5.11 Trial 2 - Yielded elements in elastic-plastic model	98
Figure 5.12 - Modeled vs. measured settlements for Basel profile 2, elastic-plastic model .....	98
Figure 5.13 - Elastic plastic model convergence	99
Figure 5.14 - Effect of a reduced softening area, expressed as a percentage of the tunnel cross sectional area, on the trough width	101
Figure 5.15 - Evidence of grout over pressurization near profiles 1 and 2	102
Figure 5.16 - Model results using grout pressures in excess of overburden	105
Figure 5.17 - Finite element mesh for strain softening model with high grout pressures .....	106
Figure 5.18 - Finite element mesh for strain softening model with high grout pressures – Detail of excavation area	107
Figure 5.19 - Strain softening modeled settlement profile using the best fit parameters	109

Figure 5.20 - Strain softening model profile showing modeling parameters and jet-grout installation sequence for the best fit (iteration 3). The varied parameters are shown in red type. ....	109
Figure 5.21 - Modeled deformation during installation of jet-grout columns 16 – 22 ...	110
Figure 5.22 - Modeled deformation during installation of jet-grout columns 23 – 29 ...	111
Figure 5.23 - Modeled deformation during installation of jet-grout columns 9-15 .....	111
Figure 5.24 - Modeled deformation during installation of jet-grout columns 30 - 37 ....	112
Figure 5.25 - Modeled deformation during installation of jet-grout columns 1 - 8 .....	112
Figure 5.26 - Yield development by stage (additional elements) .....	113
Figure 5.27 - Modeled axial force in the shotcrete liner with and without the presence of the jet-grout arch.....	117
Figure 5.28 - Modeled bending moment in the shotcrete liner with and without the presence of the jet-grout arch .....	118
Figure 5.29 - Modeled shear force in the shotcrete liner with and without the presence of the jet-grout arch.....	118
Figure A.1 Tunnel section.....	139
Figure A.2 Heading detail - grout .....	140
Figure A.3 Heading detail .....	141

## LIST OF TABLES

Table 2.1 - Tunneling ground classification, from(Terzaghi 1950).....	11
Table 2.2 - Single fluid jet-grouting paramaters .....	14
Table 2.3 - Suggested jet-grout mechanical properties (Mussger 1987) .....	18
Table 2.4 - Proportions of constituents in high early strength Portland cement,(Taylor 1990).....	20
Table 3.1 - Assumed thermal properties .....	32
Table 3.2 - Sensitivity of simulation to variation in insulation thermal properties.....	33
Table 3.3 - Sensitivity of temperature to variation in grout thermal properties.....	33
Table 3.4 - Residual Strength of grout .....	49
Table 4.1 - Depth to feature (m).....	56
Table 4.2 - Bedrock properties.....	56
Table 4.3 - Jet-grout sequencing and timing for Luzern profile 1 .....	67
Table 4.4 - Jet-grout sequencing and timing for Luzern profile 2 .....	67
Table 4.5 - Jet-grout sequencing and timing for Basel profile 1.....	68
Table 4.6 - Jet-grout sequencing and timing for Basel profile 2.....	68
Table 4.7 - Jet-grouting parameters during tunnel construction .....	70
Table 4.8 - Normal distribution fit parameters for the centerline settlement measured at Profiles 1 and 2.....	73
Table 5.1 - Observed settlements, centerline and 12m north (12) and south (-12) of Basel & Luzern profiles 1 & 2 .....	80
Table 5.2 - Range of volume loss ( $V_l$ ) for different construction techniques and soil conditions (Mair 1997).....	86
Table 5.3 - Empirical parameters for a Gaussian fit to the measured settlements.....	87
Table 5.4 - Base soil properties used in finite element model .....	91
Table 5.5 - Liner properties used in finite element model .....	91
Table 5.6 - Elastic model - Inital and best fit (final) model parameters .....	93
Table 5.7 - Elastic-plastic model - Inital and final (best fit) model parameters.....	97
Table 5.8 - Effect of reduced softening area on the trough width parameter (i).....	100
Table 5.9 - Model staging with high grout pressures.....	104

Table 5.10 - Parameters for elastic plastic model with elevated grout pressures .....	104
Table 5.11 - Strain softening model parameters - iteration 1 .....	107
Table 5.12 - Strain softening model parameters - iteration 2.....	108
Table 5.13 - Strain softening model parameters - iteration 3.....	108
Table 5.14 - Stages used in the Phase2 strain weakening model and the associated yielding due to the jet-grout process. ....	114
Table A.1 Grout installation sequence - Luzerne.....	134
Table A.2 Grout installation sequence - Basel.....	135
Table A.3 Observed settlement – Profile 1 .....	136
Table A.4 Observed settlement – Profile 2 .....	137
Table A.5 Observed settlements - Tantenholz .....	138
Table B.1 Uniaxial testing results .....	143
Table B.2 Residual grout tests .....	144
Table B.3 Vane shear tests.....	145
Table C.1 Liner component properties.....	147
Table C.2 Modelled grout timing and parameters .....	149

# 1 INTRODUCTION

In soft ground tunneling the construction of large non-circular tunnels is particularly challenging. The construction method must provide worker safety as well as meet stringent design requirements. In an urban environment one of the design requirements is that the construction method must control surface settlement within specified tolerances. In Europe, a popular construction method for large non-circular tunnels utilizes sub-horizontal jet-grout columns to form a protective fan (vault) of cemented soil ahead of the excavation face. Jet-grouting has an advantage over many other construction techniques in its ability to be used in varying ground conditions and tunnel geometric configurations.

The process of jet-grouting is a high energy process that replaces the soil with soil-cement slurry and, after hardening creates a 0.6-m-diameter column of soil-cement. As a result, in shallow tunnels the jet-grouting process may induce surface settlements that exceed the design requirements.

The Aeschertunnel in Canton Zurich, Switzerland, was excavated with a top heading ( $75\text{m}^2$ ) that utilized 35 sub-horizontal jet-grout columns for primary excavation support. The tunnel was designed to accommodate highway traffic with a completed cross sectional area of  $135\text{m}^2$ . The tunnel was excavated in glacial till, (a relatively dry medium-dense silty sand) at a depth that caused surface settlements. This thesis investigated the effect of the jet-grouting process on the surface settlements recorded at Aeschertunnel.

### **1.1 Objective**

The objective of this thesis was to determine how horizontal jet-grouting as support ahead of the excavation face of a tunnel affects the surface settlements. This thesis uses data and information collected from the Aeschertunnel in Canton Zurich, Switzerland as a basis for evaluating the ground response to the construction of a tunnel using this technique.

### **1.2 Scope**

To determine the role that the use of jet-grouting has on the surface settlement above the excavation of a tunnel, the material properties of the jet-grout must be quantified. Laboratory testing was performed to determine the development of strength and stiffness of jet-grout as a function of time. The development of the strength and stiffness with time were determined through uniaxial compression tests and Brazilian splitting tests. The testing also considered the effect of ground temperature on the curing of the grout.

The material behavior determined in the laboratory tests was incorporated in a finite element model of the Aeschertunnel. This finite element model was used to evaluate the possible mechanisms causing the pattern of the observed settlement.

### **1.3 Outline of Thesis Content**

Chapter 1 is a general introduction in the use of jet-grouting for excavation support in tunneling. The objective of the thesis and the scope of the scope required to attain this objective are presented.

Chapter 2 presents a literature review of the important issues involved in the analysis of the surface deformations when using jet-grouting as excavation support for the Aeschertunnel. Some soft ground tunneling methods are presented and the response of silty and dense cohesionless soils, such as the soils encountered in the construction of the Aeschertunnel, to tunneling works is reviewed. The jet-grout technique, jet-grout properties, and the development of strength and stiffness in Portland cement with time are presented.

Chapter 3 includes the testing procedures and results that were used to characterize the material properties of jet-grout. The testing involved producing a grout in the laboratory that would have the same proportions as the grout in a jet-grout column. Temperature modeling was carried out in order to determine how the material properties of jet-grout columns change with time.

Chapter 4 covers the field investigation of the Aeschertunnel. This includes the geology, construction procedures, and observations.

Chapter 5 presents the evaluation of the surface deformations measured at the Aeschertunnel. The deformations were evaluated using an empirical method and the finite element method. The finite element modeling incorporated the material properties of the grout determined in Chapter 3.

Chapter 6 presents the conclusions of the role of using jet-grouting in surface deformations in construction of the Aeschertunnel. Additionally topics of further research are identified.

## 2 LITERATURE REVIEW

### 2.1 Soft Ground Tunneling

Many tunnels must be constructed in weak materials, such as sands and clays. These tunnels tend to be at shallow depths and near urban infrastructure so surface settlements must be minimized. Tunneling in these conditions has led to the development of specialized tunnel boring machines (TBM's) and developments in more conventional excavation methods that provide greater ground control. The three approaches to limit the surface settlement that have received special attention in conventional soft ground tunneling techniques are;

- 1) improving the ground conditions ahead of the advancing tunnel face with ground modification techniques,
- 2) reinforcing the tunnel face with soil nails, and
- 3) providing a protective vault over the tunnel face.

All of these approaches attempt to limit surface settlements by reducing the deformations that occur ahead of the tunnel face by providing support to the soil ahead of the advancing face.

With conventional tunneling methods, such as the New Austrian Tunneling Method (NATM), it is often observed that 50% of the maximum center line settlement is developed directly over the tunnel face (Figure 2.1). When there is significant face support, most of the settlement occurs behind the tunnel face. With earth pressure balance (EPB) shield tunneling, as little as 25 to 30% of the final settlement occurs over the tunnel face (Mair 1997). The development of center line settlement in shallow tunnels can be assumed to have the shape of a normal cumulative distribution function (Attwell 1985).



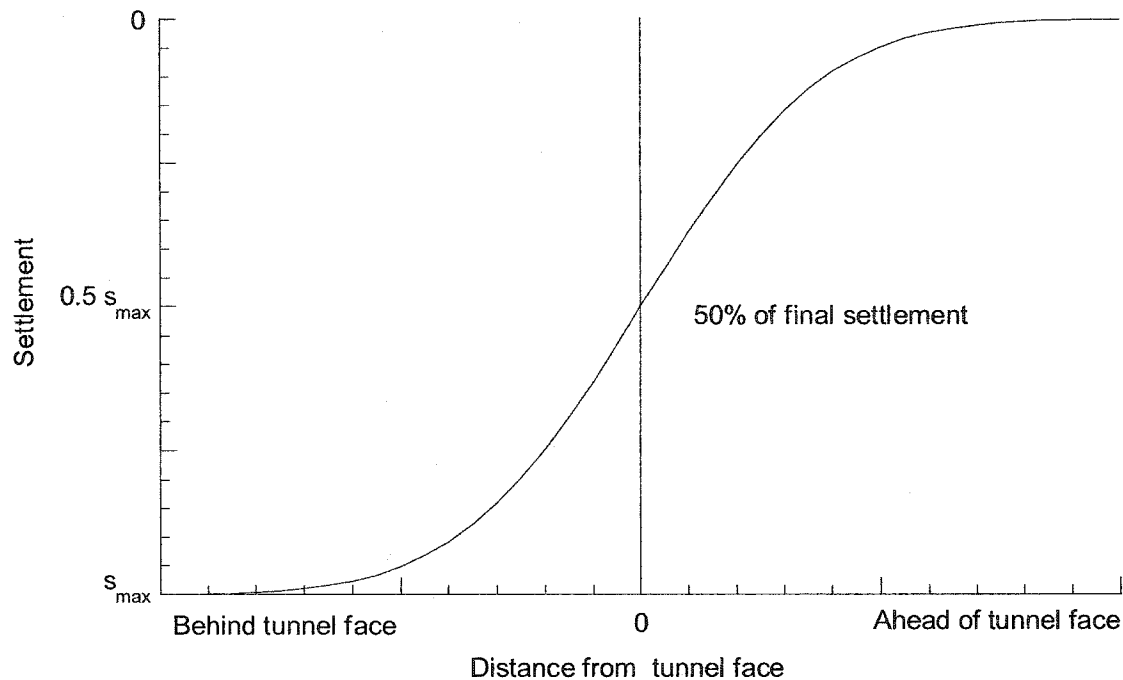


**Figure 2.1 - Typical centerline settlement development**

The standard deviation of the distribution describes the steepness of the settlements; a smaller standard deviation corresponds to steeper centerline settlements. If 50% of the final settlements occur over the tunnel face this corresponds to the normal cumulative distribution function having a mean of zero. The actual percentage of settlement that is developed over the tunnel face depends upon the construction procedure. Providing support ahead of the tunnel face or using ground modification techniques, may result in smaller percentage of the maximum settlement at the tunnel face. The distribution of the surface settlements perpendicular to the direction of the tunnel axis can be described with a normal probability function, with the standard deviation describing the steepness of the settlement trough (Peck 1969).

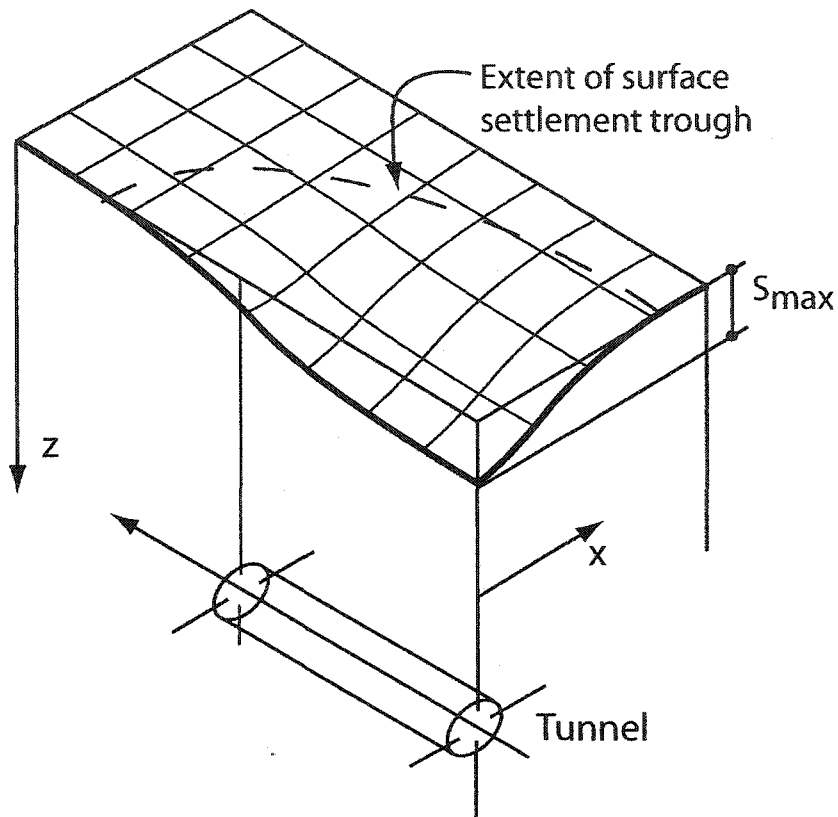


**Figure 2.2 - 3D distribution of tunneling induced settlements**

*Ground Modification*

The ground deformation shown in Figure 2.2 can be reduced with grouting techniques such as compaction grouting and permeation grouting to modify the strength and deformation characteristics of the ground. Compaction grouting uses a thick grout that has sufficient viscosity so that it will not fracture the ground, creating a bulb of grout that applies radial stresses to the soil that results in soil compaction (Bruce 1987). Permeation grouting increases the strength of the soil by filling the voids with grout, ideally maintaining the original volume and structure of the soil. The major problem with permeation grouting is that its effectiveness is very dependent on the soil permeability. For less permeable, finer grained soils, low viscosity chemical grouts may be necessary, for which there are environmental concerns. In addition, the placement of the grout is very sensitive to anisotropy and non-homogeneity of the soil (Bruce 1987).

### *Reinforced Tunnel Face*

The tunnel face can be supported with the placement of reinforcing elements. The reinforcement of the face in this manner prevents extrusion of the tunnel face and as a result limits the radial convergence and subsequent surface settlements (Lunardi Accessed 2002). In addition it also can prevent the collapse of the face in any soil. The face can be reinforced with fiberglass rods or horizontal jet-grouting. The reinforcing elements are excavated with the soil as the tunnel advances.

### *Tunnel Vault*

To provide excavation support the installation of a vault ahead of the tunnel face may be performed with Tubes-a-Manchette, jet-grouting, hydro-fracture grouting, forepoling or pretunneling. The effect of providing a vault is to reduce the radial deformations ahead of the tunnel face with the vault forming an arch to carry the excavation induced loads. The soil ahead of the tunnel face receives less of the excavation loads reducing extrusion of the face and as a result, reducing surface settlements due to volume loss (Di Cervia 2000). The formation of the vault also prevents loosening of the soil above the crown as it is placed in-situ, thus reducing additional liner loads due to loss of shear strength of the soil (Mussger 1987). The formation of a vault offers improved safety during construction as it provides soil support in the roof. With these methods the subdivision of the excavation of the face into multiple openings as seen in the New Austrian Tunneling Method (NATM) can be omitted, simplifying the construction cycles and placement of the primary liner support.

Finite element comparisons of tunnel face stability for tunnels with and without a pre-vault show that the pre-vault has very little effect on tunnel face stability in cohesionless material (Leca 2000). This has also been shown in centrifuge tests (Skiker 1994). However the face failure in a tunnel in cohesionless soils without a pre-vault will result in the propagation of the failure to the surface. When a pre-vault of sufficient length is used, the vault restrains the failure area to the soil mass directly ahead of the tunnel face (Chambon 1994). It can be concluded that the main benefit of the pre-vault is to limit ground deformations around the face, thus reducing surface settlements.

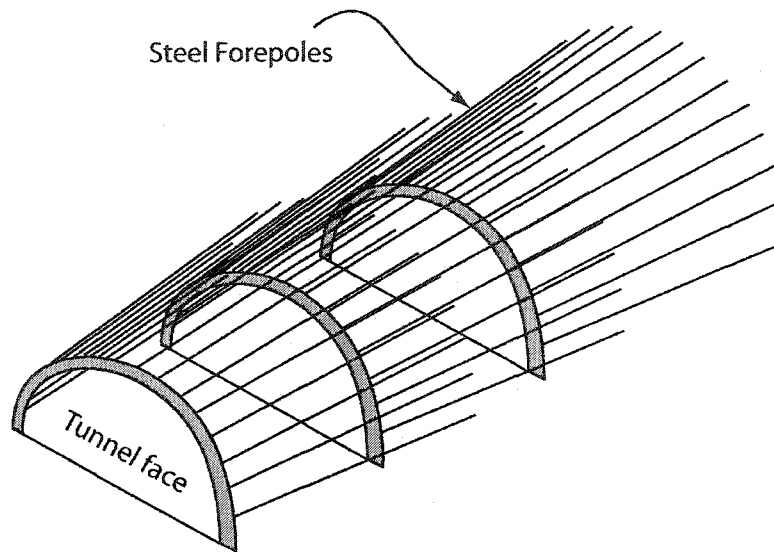


**Figure 2.3 – Typical overlapping forepoles used to provide support over the tunnel face**

Forepoling involves the installation of steel tubes as shown in Figure 2.3. The advantage of this method is that it provides immediate reinforcement. The pretunnelling system uses a chainsaw to excavate an arch ahead of the tunnel face. The chainsaw passes through an arc with the concrete being pumped in behind the excavation. The hydro-fracture technique uses high grout pressures to fracture the soil and create a set of lenses of grout in the shape of the tunnel vault. The hydro-fracture technique hasn't been widely accepted in North America due to the difficulty in controlling it, and possible damage to nearby structures due to the potential for ground heave.

The vault is often formed with the sequential installation of horizontal jet-grout columns. If the tunnel cover is very low care has to be taken to prevent hydro-fracture and heaving induced by the jet-grouting (Mussger 1987). The jet-grout columns may also be reinforced with the installation of reinforcing pipes before the grout has hardened (Di Cervia 2000).

Gioda (1999) presented observations of the construction of the Monteolimpino 2 tunnel in Italy that used an arch formed from horizontal jet-grout columns. This tunnel is a two track tunnel with a radius of 5m that passes through an alluvial deposit of sand and silty sand at an average depth of 35m. The jet-grout arch was made up of 35, 0.6m diameter, 10m long columns with 3m of overlap to form an arch for the upper ½ of the tunnel. Sub vertical jet-grout columns were installed under the base of the jet-grout arch where larger settlements were expected. The addition of these footings reduced the total settlement from 50mm to 15mm above the centerline of the tunnel (Gioda 1999).

Robinson (1991) presented the experiences in constructing the Bad-Godesburg Tunnel in Germany. A 500m long tunnel with a diameter of approximately 11m was driven in sandy gravel, and the depth of the crown below ground surface ranged from 3.5 to 6.8m. The construction method used an arch of 0.6m diameter sub-horizontal jet columns and steel forepoling. During the installation of the first columns surface heave was observed due to the minimal surface coverage and the over-pressurization of the borehole. Reducing the grout pressure and grout volume reduced ground heave to a maximum of 10mm. Final settlements of 10mm were observed in the regions where a continuous arch of jet columns was installed (Robinson 1991).

From the literature review there is ample evidence that while the creation of the vault reduces the surface settlements, the construction of this vault with the use of jet-grout columns may lead to significant heave, particularly for shallow tunnels.

## **2.1 Response of silty and dense sands to tunneling**

The Aeschertunnel was constructed in glacial till that can be characterized as dry silty sand. The response of this soil to tunneling can be difficult to predict as such soils may or may not exhibit significant stand up time.

Clayey and silty sands may exhibit apparent cohesion due interlocking grains, high densities, cementation, or locked in stresses due to a previous high overburden pressure. When tunneling above the ground water level this type of soil generally exhibits a very low tensile strength, and may fail quickly when undercut. Experience in this type of soil

has shown that if failure of the face occurs the failure zone moves upward at a slope of 4V:1H or steeper (Heuer 1987). These cohesive granular soils may also have a significant standup time, where there is a delay between the excavation and loss of strength. Heuer (1987), using Terzaghi's ground classification (Table 2.1), observed that when the unconfined compressive strength of these soils is greater than 6 times the overburden pressure the ground will be firm, at a ratio of 5:1 to 4:1 the behavior will be slow raveling. If the ratio of soil strength to overburden pressure is less than 4:1 the behavior will be fast raveling (some standup time) to running (almost no standup time).

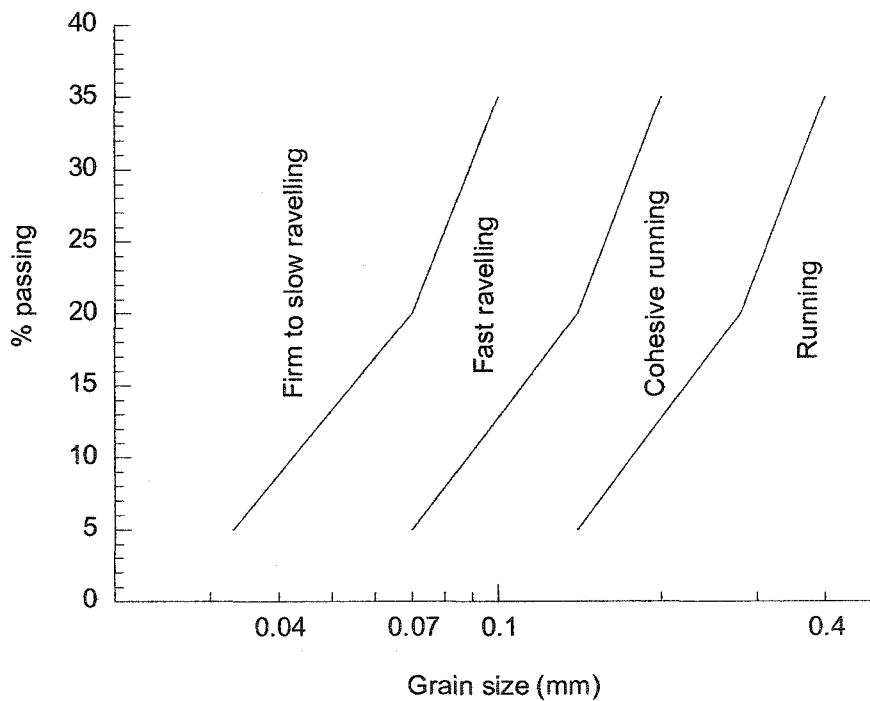


**Figure 2.4 - Behavior of dense soil ( $N > 30$ ) above ground water level, modified from Heuer (1987)**

**Table 2.1 - Tunneling ground classification, from(Terzaghi 1950)**

Classification	Ground behavior
Firm	Tunneling can advance without support
Fast Raveling	Soil begins to fall from the crown or face within a few minutes
Slow Raveling	Soil begins to fall from the crown or face after a few minutes
Cohesive Running	The material stands for a brief time of raveling followed by running
Running	Cohesionless soils run until the slope is at the angle of repose
Flowing	Soil and water enter the tunnel in a fluid manner and can completely fill the tunnel

Often cohesive granular soils display a strain-softening behavior; they show a decrease in strength with increasing deformation after reaching their peak strength. This is due to the loss of cohesion at low strains. In dense granular soils it has been observed in laboratory compression tests that the loss of strength takes place in localized areas of high strain within the sample, not throughout the sample (Sterpi 1999). This strain localization takes the form of narrow shear bands where the structure of the soil becomes highly disturbed. The sand in the shear bands may dilate, reducing the relative density and thus the frictional resistance.

Shallow tunnels constructed in this type of soil generally have a brittle deformation response at failure. When modeling tunnels in this type of soil, a strain weakening soil model is often assumed. For example Gioda (1999) performed an elastoplastic FEM analysis with a strain weakening soil, assumed to have a peak friction angle of  $40^\circ$  and residual of  $30^\circ$  to model the ground response to a 12m diameter tunnel. The mode of deformation in both models was the formation of shear bands that ran nearly vertically from the shoulders of the tunnel to the surface, resulting in a very narrow settlement trough (Sterpi 1999). Sterpi (1999) also observed the formation of shear bands using a strain softening soil model in the analysis of the collapse of a model tunnel. He concluded that tunnels without shear band formation have the formation of a larger plastic zone that extends diagonally away from the tunnel shoulders to the surface, resulting in wider settlement troughs. Hence when modeling a tunnel in this type of soil it is important to consider strain weakening soil behavior.

## 2.2 Jet-grouting

Jet-grouting was developed in the 1970's in Japan, where it was initially called "chemical churning pile" (Brill 2003; Shibasaki 2003), as an alternative to chemical grouting in low permeability soils. It was introduced in Europe first, and was in use in North America by the 1980's. The original system used single fluid system of grout comprised of Portland cement and water. In contrast to permeation grouting, which is very sensitive to the type of soils being treated, jet-grouting can be used to treat almost any soil (Bruce 1987) (Figure 2.5).

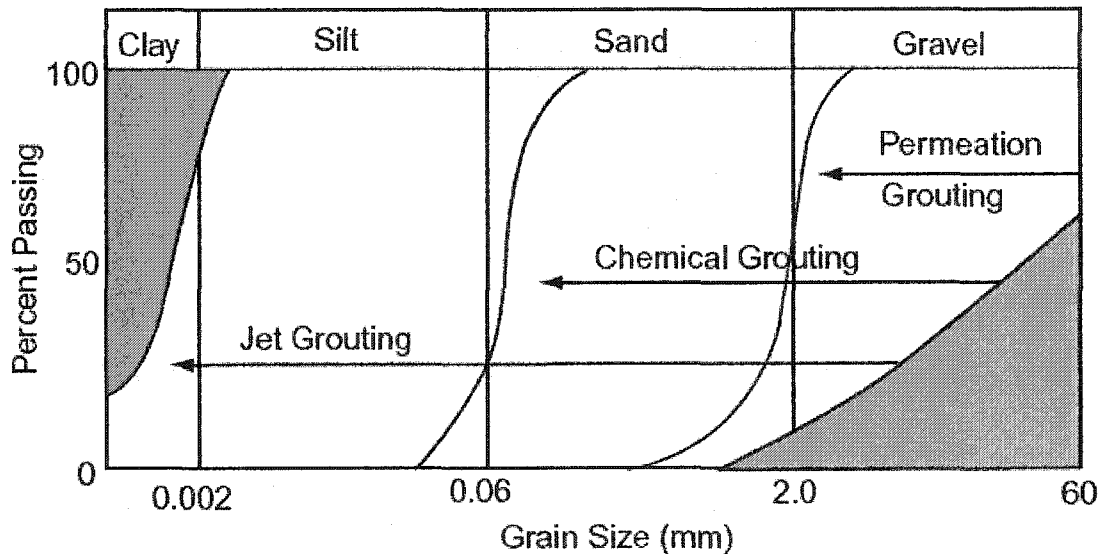
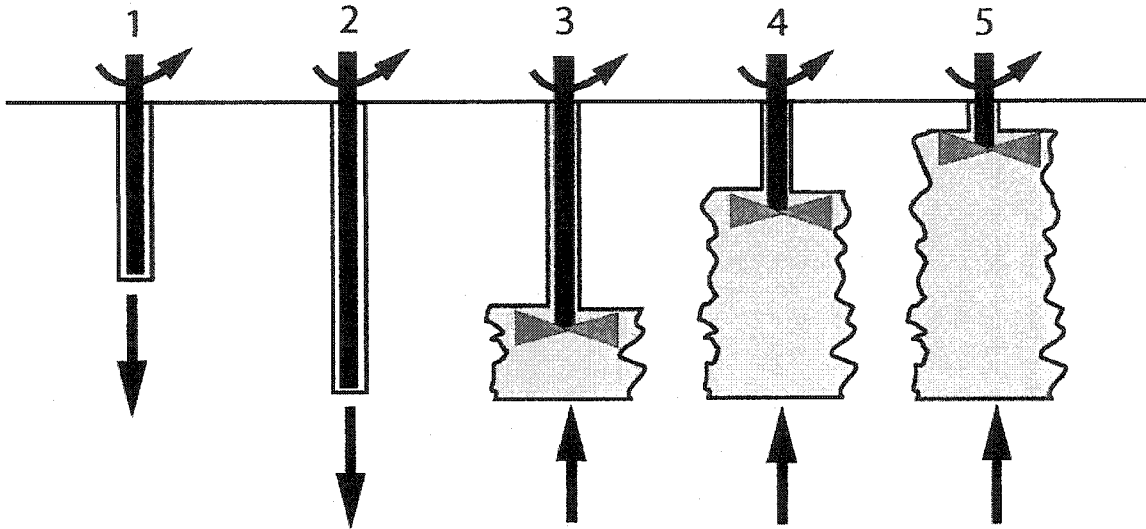


Figure 2.5. - Groutability of soils <sup>1</sup>

Jet-grouting is performed in two phases (Mussger 1987). In the first phase the drill string is advanced by rotary drilling (Figure 2.6, stages 1&2). In the second phase the jetting is started and the drill string is withdrawn in lifts and rotated (Figure 2.6, stages 3-5). The jet-grout column is produced by the in-situ erosion of soil with a high-energy fluid jet (Brill 2003). The fluid velocity is gained by forcing high-pressure grout through a small nozzle, just behind the drill bit. The drill bit has a larger diameter than the drill string, creating an annular space that permits the return of spoil. The single fluid system can produce columns up to 50 to 100 cm in diameter (Kauschinger 1992).

<sup>1</sup> Data from [http://www.haywardbaker.com/services/jet\\_grouting.htm](http://www.haywardbaker.com/services/jet_grouting.htm)





**Figure 2.6 - Jet-grouting procedure**

Double fluid and triple fluid jet-grouting are used to make larger diameter columns, up to 200 and 300cm respectively (Kauschinger 1992; Pellegrino). Double fluid jet-grouting uses a shroud of air around the grout jet. The air prevents the attenuation of the energy of the jet by the soil cement mixture; thus the jet behaves as if it is in open air (Brill 2003). The greater the velocity of the air provided, the less attenuation from the soil cement and therefore the creation of larger columns. Triple fluid jet-grouting uses a water jet in an air shroud to cut the soil prior to grout injection. The use of double and triple fluid jet-grouting is limited to columns aligned less than  $30^{\circ}$  from vertical due to the difficulty of the return of air through the annulus (Brill 2003). Because of this the double and triple fluid systems are not used in horizontal jet-grouting for tunnel support.

### **2.2.1 Factors affecting the size of jet-grout columns**

The mechanical interaction between the soil and the grout is the source of the greatest uncertainty and variability in the production of a jet-grout column. The diameter and properties of the jet grout column depend upon the soil conditions, the grout properties and the grouting parameters (Mussger 1987). Ensuring reliable jet-grouting requires that the process creates columns of uniform diameters and that the soil mixing is homogeneous and complete.

The means for controlling the size of the jet-grout column is via the amount of energy that is transferred from the jet to the undisturbed soil (Kauschinger 1992). The energy transferred to the soil depends mostly on the dynamic injection pressure, the flow rate of the grout, the rotational speed of the jet and the number of rotations performed at each lift (Brill 2003).

Increasing the pressure of the jet-grout injection results in columns of larger diameters, to a practical limit of about 60 MPa (Mussger 1987). Tests in sand and clay at various pressures have showed that the dynamic jet pressure must be greater than the compressive strength of the soil in order for the jet to have an effective eroding distance (Brill 2003). If the pressure is lower than this critical pressure extending the exposure time to the jet still results in greater extent of soil erosion.

Increasing the exposure time of the soil to the grout jet also increases the amount of energy transferred to the soil. Slowing the rotation rate and the lifting rate results in larger diameter columns, to a limit. Shibazaki's (2003) experiments on loose sand showed that at more than 5 repetitions the column diameter didn't increase significantly (Brill 2003). This is due to the complete loss of jet energy to the soil grout mixture. Increasing the grout injection rate will also increase the column diameter and the use of low viscosity grouts will produce larger more homogenous columns due to less energy loss (Bruce 1987). Typical single fluid jet-grouting parameters are given in Table 2.2.

**Table 2.2 - Single fluid jet-grouting paramaters**

Parameter	Range	Typical
Borehole diameter	76-115 mm	
Number of jets	2-4	
Nozzle diameter	1.5-3 mm	2 mm
Grout pressure	30-60 MPa	40 MPa
Grout W:C	0.8-2.0:1	1:1
Drilling rod rotation rate	10-20 rpm	15 rpm
Withdrawal rate	0.25-0.5 m/min	0.4 m/min
Grout injection rate	5-8 m <sup>3</sup> /hour	

The grout column diameter also depends on the type of soil (Figure 2.7). Cohesionless soils are more easily erodible than cohesive soils, and produce larger, more homogeneous columns.

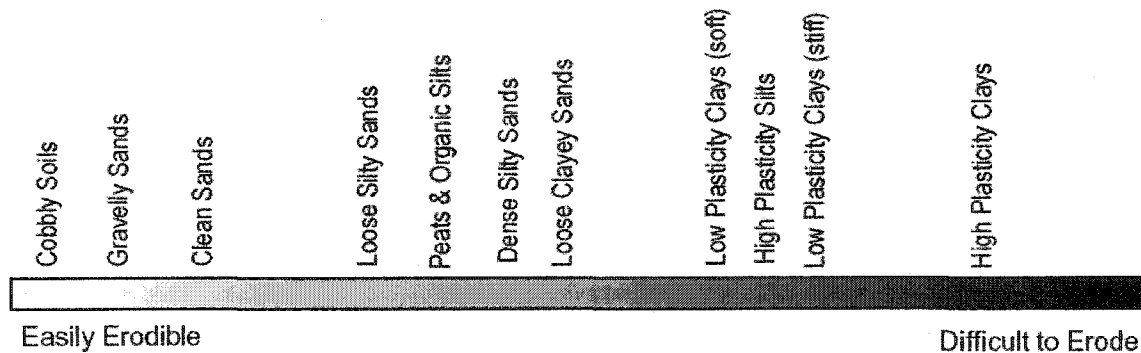


**Figure 2.7 - Soil erodibility as a function of soil type**<sup>2</sup>

The pressure head in vertical jet-grouting is equal to the weight of the cuttings around the drill rod, and frictional losses due to the flow of the spoil in the annular void. Controlling the spoil return is particularly important; if the return of spoil is stopped the resulting pressure increase can decrease the erosive effect of the jet and may cause the soil to hydro-fracture. This is particularly significant when the grouting in clays, as the clay may form a seal around the drill rod (Kauschinger 1992). Using a lower viscosity grout or reaming the hole out during the installation of a column can assist the return of spoil.

There is evidence that the jet-grout column tends to become pressurized. Despite the “open-hole” technique used to install the drill rod (Powderham 2002) noted during jet-grouting in clays that heave of up to 1m occurred and grout was boiling out of the surface 50m away due to hydro-fracturing the soil. In the back-analysis of a tunnel using horizontal jet-grouting as preliminary tunnel support Otto (1991) determined that the grout was exerting a local pressure of 1.5 to 4.8 MPa on the soil. The installation of jet-grout columns has also been noted to cause horizontal displacements in nearby retaining walls (Wong 2000). The result of this over-pressurization of the ground is that the sequence of installation is very important, i.e., the order of the installation of columns can affect the final deformations of the ground. For example, if underpinning a foundation,

<sup>2</sup>modified from [http://www.haywardbaker.com/services/jet\\_grouting.htm](http://www.haywardbaker.com/services/jet_grouting.htm)

the work should progress from low soil stresses to high soil stresses to minimize surface deformations (Brill 2003).

### **2.2.1 Composition of jet-grout & soil mixture**

Single fluid jet-grouting has been described as a soil replacement method and also a partial soil replacement method. The composition of jet-grout is dependent on the soil being treated. The analytical calculation of the composition of jet-grout isn't possible in practice because of the complex processes of erosion, mixing, replacement, filling of pore space and the jet grouting parameters (Croce 2000). During the cutting and mixing there is also spoil return with unknown composition. The prediction of the jet-grout composition must then be based upon observations.

Based upon the conservation of mass Croce (2000) proposed the following equation to predict the composition of jet-grout,

$$V = \frac{\alpha}{\delta(n + \beta - n\beta)} V_j \quad (2.1)$$

where  $V$  is the jet column volume per unit length,  $\alpha$  is the volumetric percentage of grout retained by the subsoil,  $\delta$  is the percentage of pores filled with grout,  $\beta$  is the volumetric percentage of soil removed by the jet action,  $n$  is the original soil porosity, and  $V_j$  is the volume of injected grout per length of treatment. This formulation for predicting the composition of cured grout doesn't include any volume changes due to loss of bleed water or the contraction during hardening. Most often, excluding the case of jet-grouting in clean gravels, the pores can be assumed to be completely filled with grout ( $\delta=1$ ).

Kaushiger (1992) reported that the grouted soil outflow ranged from 0 to 80% of the injected grout volume. In general the percent outflow is less than 50%, with a typical value of 30%. Complete retention (0% outflow) would only be expected in clean gravels, where the grout will permeate through the voids (Croce 2000). Croce (2000) reported that the grout volume was 60 to 80% of the treated volume for single fluid jet-grout

columns. If complete mixing is assumed within the column and a porosity of 0.35 is used, this corresponds to 70 to 80% of the grout volume being retained.

The condition of complete mixing would result in the percent of the grout retained within the column be equal to the percent of soil retained within the column, ( $\beta=1-\alpha$ ). Croce (2000) found that the percent soil removal ( $\beta$ ) ranged from 30 to 60%, and the percent of grout retained ( $\alpha$ ) was 65 to 90% in field trials of single fluid jet-grouting on sandy gravel and silty sand. The expelled soil grout mixture had a greater proportion of soil than the columns. Their findings confirm that single fluid jet-grouting is a partial soil replacement ground improvement technique, it doesn't completely replace the soil, nor does it completely mix it (Kauschinger 1992).

The percentage of soil removal in vertical jet-grouting decreases with increasing depth (Kauschinger 1992; Croce 2000). This may be due to greater hydraulic pressure limiting spoil expulsion at greater depth, or the continuous erosion of the annular void. It may also be an apparent effect, seen due to the settling of the soil particles in the suspension. The result is that vertical jet-grout columns have a higher density and thus strength at their bases.

### ***2.2.2 Properties of jet-grout***

Jet-grout behaves much like Portland cement concrete. It generally has a non-linear elastic response followed by a brittle failure. Its strength has a cohesive and a frictional component. Triaxial testing of specimens produced in silty sands had a cohesion of 4.2 MPa and a friction angle of  $35^\circ$  (Fang 1994). The Japan Jet-grout Association reports that the mean strength tested under uniaxial compression of sandy soils is 12.7 MPa and for cohesive soils 2.8 MPa (Brill 2003).

The most important parameter controlling the strength of cured jet-grout is the dry density (Fang 1994). The grout strength increases with increasing dry density (Kauschinger 1992). Cohesive soils tend to produce weaker jet-grout than non-cohesive soils

**Table 2.3 - Suggested jet-grout mechanical properties (Mussger 1987)**

Soil Type	UCS (MPa)	E (GPa)
Clayey silt	0.3-0.5	0.06-0.45
Sandy silt	1.5-5	0.5-2
Fine sand	5-10	2-5
Gravelly sand	5-15	3-11
Sandy gravel	5-20	4-20

In coarser, more permeable soils more of the excess water in the grout mixture can be expected to be forced from the jet-grout structure than for finer grained soils resulting in denser jet-grout. This is the primary reason for treated sandy soils having greater strength than less permeable finer grained soils (Bruce 1987). Higher water to cement ratios also reduces the dry density resulting in weaker grouts as shown in Figure 2.8.

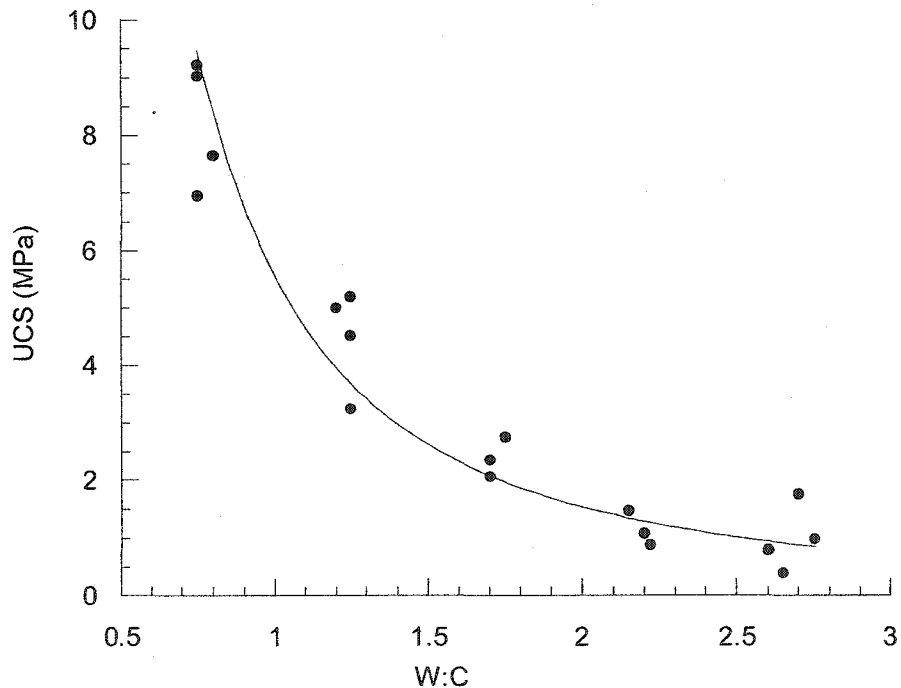


**Figure 2.8 - Relationship between uniaxial compressive strength (UCS) and water to cement ratio, by weight, data from Kauschinger (1992)**

The tensile strength of jet-grout increases with increasing unconfined compressive strength. Tests on jet-grout produced from sandy soils showed that the tensile strength was approximately 3 to 10% of the unconfined compressive strength, while the Poisson's ratio varied between .12 and 0.32 with a mean value of 0.2 (Fang 1994). There appears to be no effect from the dry density of the jet-grout mix on the Poisson's ratio. The Young's modulus increases with increasing jet-grout strength, and tends to be between 100 and 300 times the unconfined compressive strength (Kauschinger 1992; Fang 1994).

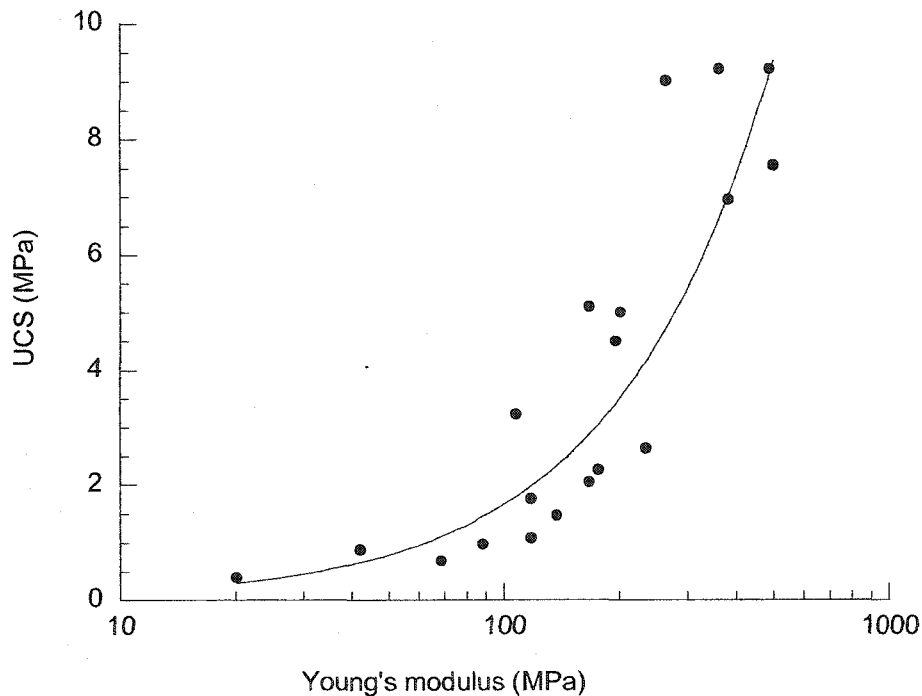


**Figure 2.9 - Relationship between unconfined compressive strength and Young's modulus for single fluid jet-grout, data from Kauschinger (1992)**

Incomplete mixing of the grout and soil produces a variable jet-grout, resulting in unpredictable material behavior. If mixing is complete a stronger structure will result. Croce (2000) compared the strength of well produced homogeneous jet-grout with hand mixed specimens and found that samples with the same dry density had the same strength.

## 2.3 Portland Cement

### 2.3.1 Chemistry

The main phases present in Portland cement are tricalcium silicate ( $C_3S$ ), dicalcium silicate, ( $C_2S$ ), tricalcium aluminate ( $C_3A$ ) and smaller amounts the ferrite phase ( $C_4AF$ ) and periclase ( $MgO$ ). There are minor components of phosphates, fluorides and heavy metal oxides due to impurities in the limestone used to manufacture the cement. In addition gypsum ( $CaSO_4$ ) is added as a retarder to prevent flash set.

The strength of grout using Portland cement is mainly due to the hydration of  $C_3S$  and  $C_2S$ .  $C_3S$  reacts quickly and is the greatest contributor to strength of hardened cement pastes. High early strength (Type 30) is obtained by increasing the content of  $C_3S$  and also by grinding the clinker to produce smaller cement particles, providing a higher specific surface area. High early strength cement provides high strength in a week or less and is used when the strength is required quickly due to the early removal of the forms or use in colder weather (Kosmatka 1995). The composition of typical ASTM Type III Portland cement (CSA type 30) is shown in Table 2.4.

**Table 2.4 - Proportions of constituents in high early strength Portland cement (Taylor 1990)**

	%
$C_3S$	53
$C_2S$	19
$C_3A$	11
$C_4AF$	9
$MgO$	2



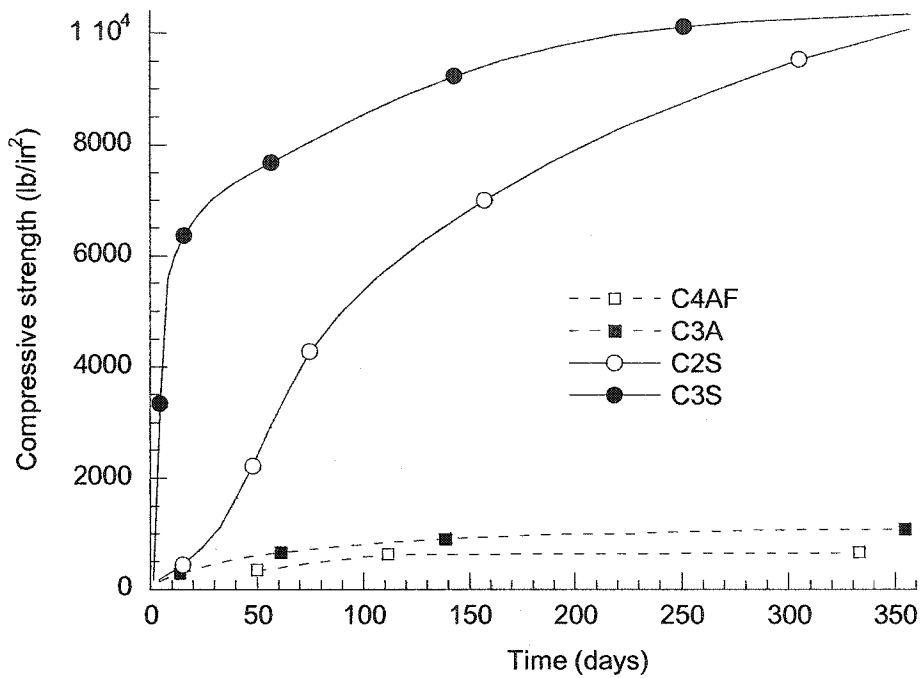


**Figure 2.10. - Strength of Portland cement constituents, data from Bye (1983)**

The calcium silicates hydrate to form calcium silicate hydrates (CSH, also referred to as tobermorite) which provides almost all of the strength of Portland cement. The aluminates react quickly in Portland cement. The calcium aluminates hydrate quickly to form calcium aluminate hydrates (CAH) but provide very little strength.

C<sub>2</sub>S reacts much more slowly than C<sub>3</sub>S and correspondingly provides significant strength gain only after long periods of time. The faster reaction of the C<sub>3</sub>S may be explained by the ions in the C<sub>2</sub>S being much more densely packed (Bye 1983). The composition and structure of the CSH gel changes through the course of hydration and with variation in the temperature of hydration.

### **2.3.2 Hydration Process**

The setting and hardening of Portland cement paste results from the reaction products forming a gel. This gel acts as a solid and is formed as a cohesive dispersed medium with two components; the dispersed component and the dispersion medium (Taylor 1990). The gel may have a thixotropic behavior, in this state the gel is able to regain its strength after being disturbed.

The mixing of water with cement results in the dispersion of the cement particles. The reaction of the cement with the water quickly produces hydration products on the surfaces of the cement particles. This process results in the consumption of water and cement grains with the reaction product occupying the space left behind. As hydration continues the hydrated surfaces of the grains continue to grow so that the hydration products meet each other and the gel is formed. This is described as the initial setting. This generally occurs after a few hours at room temperature. As the hydration continues, the gel continues to form and the cement hardens.

Setting of Portland cement is the change of the behavior from a fluid to a solid. Hardening is the development of strength in a set cement paste. The initial reaction upon contact with water of unretarded Portland cement is very rapid, with a large amount of heat production. This can lead to flash set of the cement paste. False set is the early stiffening of the cement paste, which can be overcome by remixing the paste. The use of high water or cement ratios and extended mixing periods will prevent false set. Little total heat is produced in false set.

The hydration of cement pastes exhibits at least two and sometimes three peaks of heat generation. The first peak is produced immediately after the mixing of the cement with water. The rate of heat generation in this first cycle reaches a maximum at about 5 minutes and then rapidly falls off, due to the water becoming saturated with gypsum. The heat generated in this cycle is due to the hydration of  $C_3A$ . During the first peak the cement may produce enough heat to flash set if it isn't sufficiently retarded. During the hydration of cement in adiabatic conditions, this first peak is followed by a period of 1 to

6 hours where the rate of heat generation is very low, but still greater than zero (Bye 1983). During this low period the rheology of the paste remains fairly constant. Figure 2.11 shows the heat generation rate for isothermal hydration for normal Portland cement at room temperature.

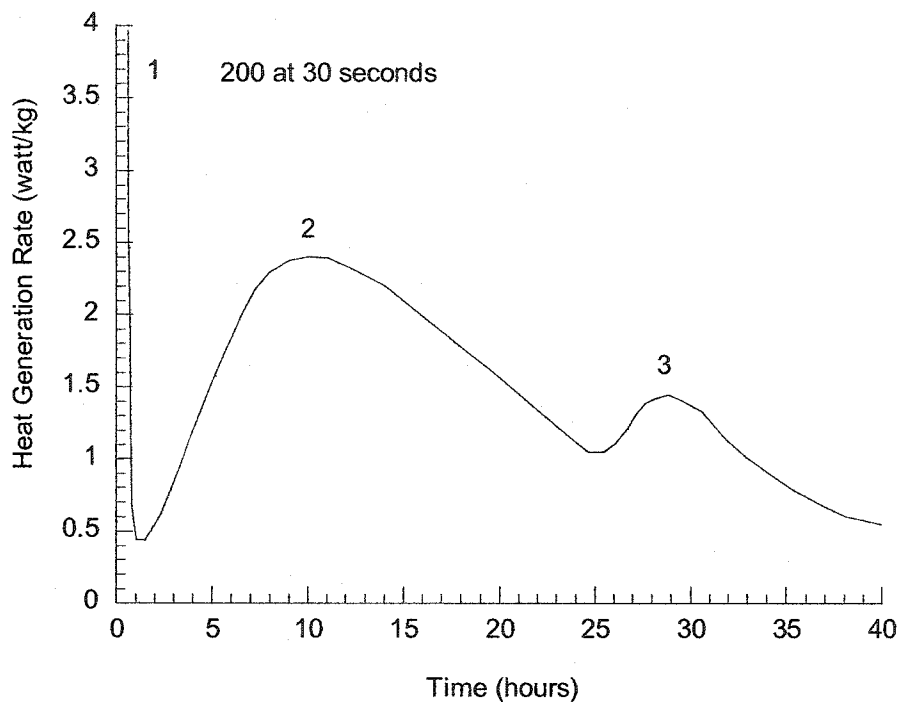


**Figure 2.11. - Heat generation rate for normal Portland cement (Taylor 1990)**

The second cycle starts at 1 to 3 hours after mixing, and the peak is observed from 6 to 10 hours after mixing and then slowly decreases (Bye 1983). During this cycle the heat generation is due to the hydration of  $C_3S$ . The decrease in the rate of heat generation after this peak is due to two causes: the decreasing surface area of the cement particles and the inhibiting effect of the CSH gel coating the particles. The time of initial set occurs on the rising side of this second peak and final set usually occurs shortly after this peak. The time of initial set occurs when the CSH gel begins to interlock.

The overall rate of heat generation is influenced by the water:cement ratio. A higher water:cement ratio will produce a faster rate of heat generation, although when the cement is first mixed with water, the rate of heat generation is independent of the water:cement ratio. The surface area of the cement influences the rate at this time. As the hydration continues the available space for the hydration products decrease, so for a higher water to cement ratio there will be greater space and thus a faster heat generation rate.

In addition Taylor (1990) noted that higher curing temperature increased the degree of hydration, but the nature of the strength-porosity relationship was different for samples cured at different temperatures. They concluded that the strength depended not only on the porosity but also on the type of hydrated materials. A cement paste hydrated at higher temperatures will have a better-defined crystalline structure. They suggested that the hydrated cement with an ill-defined crystalline structure had greater solid to solid bonds.

### **2.3.3 Material Behavior**

Concrete will deform due to elastic stresses, temperature changes, creep and drying induced shrinkage. Concrete in the process of hardening will experience a volume loss due to bleeding of excess water and the difference in the volume of the hydration products and reactants.

The stress-strain curves for concrete generally have non-linear behavior due to the interaction of the cement paste and the aggregate. The Canadian Portland Cement Association (Kosmatka 1995) suggests that the Young's modulus ( $E$ ) of concrete may be estimated as shown in Equation 2.2.

$$E = 4500\sqrt{f_c'} \quad (2.2)$$

Where  $f_c'$  is the 28 day uniaxial compressive strength of the concrete in MPa. Aggregate has a higher Young's modulus than the hardened cement paste, a Portland cement aggregate mix has Young's modulus between the two. The Young's modulus of the cement paste component is dependant on the porosity, as shown Equation 2.3 (Bye 1983).

$$E = E_o(1 - \varepsilon)^3 \quad (2.3)$$

Where  $E_o$  is the Young's modulus of the gel and  $\varepsilon$  is the porosity. As the cement hydrates and the porosity is reduced, the gel stiffens. The Poisson's ratio for concrete has a value between 0.15 and 0.25 depending upon the aggregate used, moisture content, age and compressive strength (Kosmatka 1995).

The amount of creep depends on the magnitude of the applied stress, age and strength of the concrete, and the duration of the applied stress (Kosmatka 1995). Shrinkage increases with increasing water to cement ratios and increasing fines content and occurs if the concrete is allowed to dry. Drying shrinkage of 0.3% was observed in experiments with a water to cement ratio of 0.72 (Kosmatka 1995).

Bleeding is the release of water from the unhardened cement due to the sedimentation of the cement particles and corresponding upward migration of water. The rate of bleeding and the bleeding capacity, (percent volume loss due to release of bleed water) increase with higher water cement ratios, pressures and concrete height (Kosmatka 1995). Well-graded aggregates and finer cements reduce the bleed volume. A slight contraction takes place during the hydration of cement due to the hydration products occupying less space than the reactants. These expansions and contractions are not of significant proportions (Taylor 1990).

The strength of a cement paste can be described by Bal'Shins equation (Taylor 1990), given as,

$$\sigma = \sigma_o(1 - \varepsilon)^4 \quad (2.4)$$

where  $\sigma_0$  is the strength of the gel,  $\varepsilon$  is the porosity of the gel including all unused reactants, and  $A$  is a constant with a value of 2.7 to 3. As the cement paste hydrates its porosity drops and the hydrate structure replaces the free water. Above a water to cement ratio of about 0.3 there will be incomplete consumption of the water and the excess water will give a lower strength, high porosity concrete. As the porosity of the paste drops during hydration, the cement paste gains strength. This relationship assumes that the most important requirement for developing strength is the filling of the void spaces with gel, and is not concerned with the gel structure.

A more complete assessment of the strength of a cement paste includes the composition of hydration products and reactants, which is also dependant upon the curing temperature (Taylor 1990). The dependence of curing temperature has been observed in cements hydrated to the same degrees but at different temperatures. Thus the rate of heat generation isn't solely dependent on the degree of hydration and current temperature. This suggests that the strength is also dependent by the time-temperature path that the state of hydration is reached.

## **2.4 Summary**

This literature review presents the use of jet-grout in the preliminary support of tunnel excavations, the jet-grout technique, and the composition and properties of jet-grout and Portland cement. The following conclusions are presented:

- 1) The jet-grout technique has become increasingly used in difficult tunneling conditions in recent years. Jet-grouting has an advantage over many other construction techniques in its ability to be used in varying ground conditions and tunnel geometric configurations.
- 2) The process of jet-grouting is a high energy process that may be considered to be a partial replacement soil treatment. The result of the nature of the process is that it may be applied to nearly any type of soil, yet the quality of the construction is very dependant on the jet-grouting parameters and workmanship.

- 3) Care must be taken during the jet-grouting process to ensure that the soil is well mixed and grout pressures within the column are kept to a minimum to prevent heaving of the ground.
  
- 4) The hydration of Portland cement is an exothermic reaction. The rate of hardening is dependent upon the chemical composition and the temperature. The strength and stiffness of Portland cement is dependent upon its chemical composition, mix proportions and the time-temperature path that it experiences. Also the strength of jet-grout columns will depend on these factors.

### 3 Laboratory Testing of Jet-grout Properties

The use of horizontal jet-grouting to form a stiff arch ahead of the excavation of a tunnel requires that the grout's short term strength and stiffness be determined in order to understand how the settlements are affected by these parameters. To characterize the behavior of jet-grout, 41 specimens were tested to determine the development of strength and stiffness. The testing was performed on 76mm diameter samples that were insulated to simulate the heat flow from a 600mm diameter jet-grout column installed in sand at 8°C (the same temperature as the ground at the Aeschertunnel). The tests were performed at 9 time intervals, starting at 6 hours to 28 days after mixing the grout. In addition the ability of jet-grout to recover strength after being tested to failure was evaluated. This was done to determine how strong grout would become after it had been disturbed before significant strength gain.

#### 3.1 Mix Design

The water to cement ratio of the jet-grout tested was 1:1 by weight. The grout was proportioned to be the same as jet-grouting with 50% soil removal. The assumed in-situ density of the soil was 18 kN/m<sup>3</sup>, with the soil solids having an assumed specific gravity of 2.65. The specific gravity of the cement solids was assumed to be 3.15 (Kosmatka 1995). This corresponds to an aggregate to cementing materials ratio of 9:5 by weight. The initial density of the grout mix is then 19 kN/m<sup>3</sup>. All of the materials were stored at 8°C.

The aggregate used was sand from a glacial outwash deposit in the Edmonton area. The sand was collected from the 4100 block of Whitemud Drive, where a slide occurred in October 1999. As the sand was slightly cemented it was broken up in the University of Alberta Laboratory and then screened through a #16 sieve to remove any particles larger than 1.18 mm. The sand was oven dried and stored in a sealed container.



The cement used was CSA type 30 high early strength Portland cement. This was supplied by Inland Cement Limited. The water used was tap water from the University of Alberta Laboratories.

### **3.2 Grout Mixing & Casting Procedure**

The grout was mixed in a heavy duty commercial mixer with a 15 liter capacity. The aggregates, cement and water and the insulating rings were stored in the temperature controlled room to ensure that their temperatures were all consistently 8°C. Mixing was performed for 5 minutes. Following mixing the grout was poured into the cylinders (Figure 3.1). This was done by pouring the grout through a funnel connected to a glass tube. The glass tube was inserted through the holes in the spacers that would form the ends of the cylinders. The filling of the cylinders proceeded from the bottom to the top to avoid the formation of air pockets. After the filling of the cylinders a thermistor was placed into the top portion of the grout in one of the samples and the top caps inserted. The insulation rings were then placed over the completed samples and they were taken to the temperature controlled room 20 minutes after mixing commenced. The cylinders were placed on the shelf in a horizontal position so that the bleed water would rise to the side of the samples so smooth tops and bottoms of the samples would be formed. The cylinders were placed in sets of 2, end to end, with 76mm of insulation at each end of the set. This was done to more closely approximate radial heat flow. The sample with the thermistor had the end containing the thermistor against the next sample as this would provide the closest approximation to radial heat flow.

#### **3.2.1 Cylinder Design**

The cylinders used to form the casts of grout were 76 mm inner diameter by 305mm long acrylic tubes. The acrylic tube was cut along one edge to minimize the disturbance of the grout during removal. Plastic spacers, 19mm thick were inserted into the acrylic tubes 152mm apart so that a 2:1 height to diameter ratio sample would be obtained. The spacers were used so that samples with smooth, square ends would be produced. This eliminated the need to cap or cut the samples. Capping was ruled out because the

additional time required and heat provided by the sulfur capping compound may have resulted in further hydration and hence strength and stiffness gain. Cutting the end of the samples wasn't used because of the difficulty in handling the weak samples. The spacers had two 12mm holes to enable the placement of the grout. The imperfections on the ends of the samples resulting from these holes were easily removed with a metal scraper. The insulation around the cylinders was extruded polystyrene. This was supplied in sheets 38mm thick. The insulation was cut into 200mm outer diameter rings with a 76mm hole in the center. The insulation was manufactured by Owens Corning.

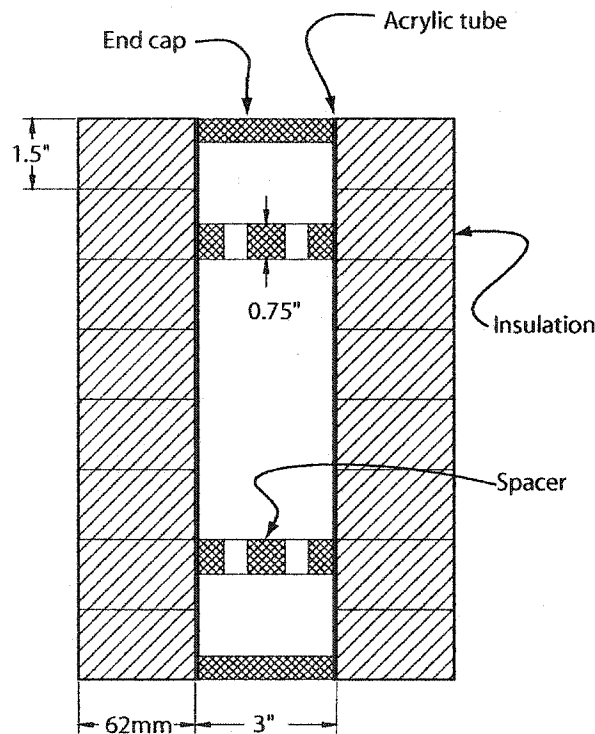


**Figure 3.1 - Grout cylinder design**

### **3.2.2 Insulation Design**

The laboratory testing was performed to simulate the development of strength of jet-grout in-situ. Because the strength of hardened cement depends on the time-temperature history that it experiences, the laboratory tests were scaled so that they would have a similar time-temperature history as a jet-grout column installed in the field.

The scaling could not be done in an analytical manner due to the different thermal properties of the soil in-situ and the laboratory insulation. The scaling used the finite difference technique to simulate radial heat flow from a cylindrical source (jet-grout column, laboratory sample) into an insulator (soil in-situ, laboratory insulation). Prior to commencing testing the heat flow from 76mm diameter laboratory sample was simulated with a cylindrical insulating cylinder of expanded polystyrene. The field condition simulated was assumed to be a 600mm diameter column installed in saturated sand. The thermal conductivity and volumetric heat capacity of the grout was assumed to be constant throughout the grout hydration process for the simulation of both the field conditions and the laboratory tests. The heat generation rate due to the hydration of the cement was also assumed to be constant throughout the test.

The medium surrounding the grout was assumed to be saturated sand, with a dry density of  $18 \text{ kN/m}^3$ . The thermal conductivity ( $k$ ) and the volumetric specific heat ( $C_p$ ) for this soil are  $0.0025 \text{ kJ/m}^\circ\text{C}$  and  $2520 \text{ kJ/m}^{3^\circ}\text{C}$  respectively (Lunardini 1981).

Due to the change in the chemistry of the grout as it hydrates its thermal conductivity and the volumetric heat capacity are not constant. The volumetric heat capacity of the grout used in the finite difference technique was based on an average value of the volumetric heat capacity of cured concrete ( $2150 \text{ kJ/m}^{3^\circ}\text{C}$ ), (US Army Corps of Engineers 1988) and the volumetric heat capacity of the initial mix ( $3100 \text{ kJ/m}^{3^\circ}\text{C}$ ), (Kosmatka 1995). The thermal conductivity was based on the average value the thermal conductivity of cured low density concrete ( $0.0007 \text{ kJ/m}^\circ\text{C}$ ), (US Army Corps of Engineers 1988) and the initial thermal conductivity acting like a saturated fine grained soil ( $0.0018 \text{ kJ/m}^\circ\text{C}$ ), (Lunardini 1981). The thermal properties used in the finite difference model are shown in Table 3.1. The assumed heat generation rate was  $0.65 \text{ kJ/m}^3\text{s}$  for the grout, based upon experiments on type 30 Portland cement (Zielenkiewics 2001).

**Table 3.1 - Assumed thermal properties**

Material	k	C <sub>p</sub>
	$\text{kJ}/(\text{s} \cdot \text{m} \cdot ^\circ\text{C})$	$\text{kJ}/(\text{m}^3 \cdot ^\circ\text{C})$
Grout	0.00125	2625
Insulation	0.000032	41
Sand	0.0025	2500

The finite difference technique used was an implicit differentiation. This method uses the current temperature of a node to calculate the temperature of the neighbouring nodes, rather than the explicit technique which uses the temperature at the last time step. The implicit method is unconditionally stable (Poulikakos 1994), whereas the explicit method suffers from the need to be careful in selecting the time and distance steps. If they are chosen incorrectly, the solution will be unstable, and not converge to a unique solution. The numerical differentiation chosen was first order in time and second order in the radial distance.

The difficulty in the implicit finite difference solution is that a large set of equations are generated. The problem of radial heat flow is one dimensional ( $r$ ), so that each equation has 3 unknowns, the temperature at node  $n$ ,  $n-1$  and  $n+1$ . In matrix form, these equations can be expressed as a tridiagonal matrix. These equations may be solved with matrix methods or iterative methods. The method used to solve the system of equations was the Thomas algorithm (Poulikakos 1994).

The thickness of the insulation was varied in the finite difference model until the grout in the laboratory simulation and field simulation had a similar average temperature history for the initial 24 hour period. The average temperature is the average temperature in the radial direction in the finite difference simulations at each time interval. The temperature profiles cannot be exactly matched due to the lack of an analytical solution that could be used to scale the test. This is due to the difference between the temperature gradients on either side of the grout/insulator interface in the laboratory simulation and the temperature gradients on either side of the grout/sand interface in the field simulation. The thickness of polystyrene insulation decided upon was a ring with an outer diameter

of 200mm and inner diameter of 75mm. This provides a temperature history that has an average temperature over 24 hours of 3.5% higher for the laboratory condition than the field condition, with a range of +8.5% to -4.9%.

The temperature was measured with thermistors. This data was recorded with a data Dolphin at 10 minute intervals. The room temperature was recorded with a thermistor placed in glycol to prevent reading fluctuations.

A sensitivity analysis was performed to evaluate the dependence of the finite difference matching technique on the assumed thermal properties. The sensitivity of variations of the properties of the polystyrene insulation is shown in Table 3.2. The sensitivity of variations of the properties of the grout is shown in Table 3.3. The errors are expressed as how many percent higher the laboratory simulation temperatures were than the field simulation temperatures.

**Table 3.2 - Sensitivity of simulation to variation in insulation thermal properties**

Temperature change	Cp kJ/(m <sup>3</sup> *°C)		k kJ/(s*m*°C)		Insulation radius mm	
	High val.	Low val.	High val.	Low val.	High val.	Low val.
	61	21	0.000035	0.0000175	110	90
Maximum (%)	7.7	9.3	7.2	10.1	9.7	7.3
Minimum (%)	-5.2	-4.6	-9.8	0.5	0.0	-10.5
Average (%)	2.9	4.1	0.5	6.6	6.2	0.2

**Table 3.3 - Sensitivity of temperature to variation in grout thermal properties**

Temperature change	Cp kJ/(m <sup>3</sup> *°C)		k kJ/(s*m*°C)		Q kJ/(m <sup>3</sup> *s)	
	High val.	Low val.	High val.	Low val.	High val.	Low val.
	3100	2150	0.0018	0.0007	0.9	0.5
Maximum (%)	7.9	9.2	12.3	4.3	8.5	8.5
Minimum (%)	-3.5	-6.8	2.4	-15.9	-4.9	-4.9
Average (%)	3.7	3.0	8.9	-4.1	3.5	3.5

The sensitivity of the finite difference solution to changes in the insulation properties appears to be minimal. While this technique doesn't explore the effects of changing more than one variable at a time, the values chosen for the ranges are the extremes for extruded polystyrene (Turner 1981). The effect of variation in the insulation diameter and changing the grout properties has a minimal effect on the error. The rate of heat generation also appears to have no effect on the error.

### **3.3 Tests Performed**

#### **3.3.1 Shear Vane Tests**

Shear vane testing was used to determine approximately the time at which the samples could be removed from the moulds and tested. The unconfined compression tests commenced when the shear strength provided from the vane shear tests was in excess of 20 kPa, as this was considered to be the weakest at which the samples could be handled without damage. The grout that was used in the vane shear tests was placed in a 102mm diameter container 51mm deep. The grout was kept at room temperature.

#### **3.3.2 Uniaxial Compression**

The young's modulus and uniaxial compressive strength was tested on a loading frame manufactured by Engineering Laboratory Equipment Limited, a Tritest 50 model. This loading frame is a displacement controlled type. The loading rate for all tests was 0.5mm per minute. The load applied to the lower strength samples (<9hrs) was measured with a 2.23 kN load cell, that was amplified to provide greater resolution. The load applied to the higher strength samples (>9hrs) was measured with a 22.3 kN load cell. The axial strain was measured with an LVDT.

The tests were performed at approximately 6, 7, 8.5, 10.5, 13.75, and 18.5 hours, and also at 1, 2, 3 and 28 days. The 2, 3 and 28 day samples were removed from the cylinders at 1 day and curing was continued in a moisture controlled room in the University of Alberta laboratories. The geometry and weight of samples was measured after they were removed from the cylinders.

### **3.3.3 Tensile Strength**

The tensile strength was measured with the smaller samples from the ends of the moulds. The Brazilian test was performed to determine this. The same loading frame and test conditions used in the uniaxial compression tests were used.

The Brazilian test method followed ASTM C496-71. This test provides an indirect measurement of the tensile strength of cylindrical concrete specimens. When a grout specimen is tested in this manner the tensile stresses are uniform and perpendicular to the loading direction. The magnitude of the tension is given by Equation 3.1.

$$T = \frac{2P}{\pi ld} \quad (3.1)$$

Where  $P$  is the compressive load,  $l$  is the specimen thickness and  $d$  is the specimen diameter. The vertical stress induced in the specimen is non-uniform, with a minimum at the center of the sample and increasing towards the edges. According to Griffith's failure criterion, failure initiates at the center of the sample when the compressive stress induced at the center of the sample is three times the magnitude of the tensile stress (Goodman 1989). The Brazilian test provides greater values of tensile strength than the direct tension test. This may be due to the observation that fissures weaken a direct tension test more than they do a Brazilian test.

### **3.3.4 Residual Strength**

The residual strength and stiffness was determined for samples that hadn't undergone the majority of hydration. This testing was performed on samples that had a plastic post peak failure response. The samples that had a brittle post-peak failure couldn't be evaluated because of their destruction during testing.

The uniaxial compressive test, as described earlier, was the only test performed. The tensile test wasn't performed because of the destruction of these samples. The residual tests were performed on 6, 7 and 8.5 hour old samples. The tests were performed at a constant strain rate of 0.5 mm/min until the peak load had been reached and continued to deform plastically to ensure that the failure had occurred. The load applied was measured with the amplified 2.23kN load cell. The geometry and weight of samples was measured after they were removed from the cylinders.

After failure had occurred the samples were placed in the moisture controlled room until they were 24 hours old. At 24 hours the samples were removed and again measured for weight and geometry. The uniaxial compression test was performed. The load applied was measured with the 22.3 kN lb load cell.

As a control for these residual strength experiments, 6 samples were cast and 2 were removed from the casts at 6, 7 and 8.5 hours and immediately placed in the moisture controlled room. These were allowed to cure until 24 hours since initial mixing had passed, and then the uniaxial compression test was performed.

The control was necessary because the samples that were removed from the cylinders and placed in the moisture controlled room wouldn't follow the same temperature history as the samples allowed to cure in insulation. The samples in the moisture controlled room may experience a higher or lower temperature history than the insulated samples, resulting in a greater or lesser degree of hydration, respectively, than the 24-hour insulated samples.



### 3.4 Testing results

#### 3.4.1 Unconfined Compressive Strength

The unconfined compressive strength is observed to initially increase with time with a power type of relationship: the rate of strength gain is increasing with time. This is observed in Figure 3.2 as the straight line portion up to approximately 10.5 hours at which the rate of strength gain is at its greatest. Beyond 10.5 hours the rate of strength gain slows with time. This can be observed as the curved part when the time is greater than 10.5 hours. The 28 day strength has a mean of 14.2 MPa and a standard deviation of 0.75 MPa.

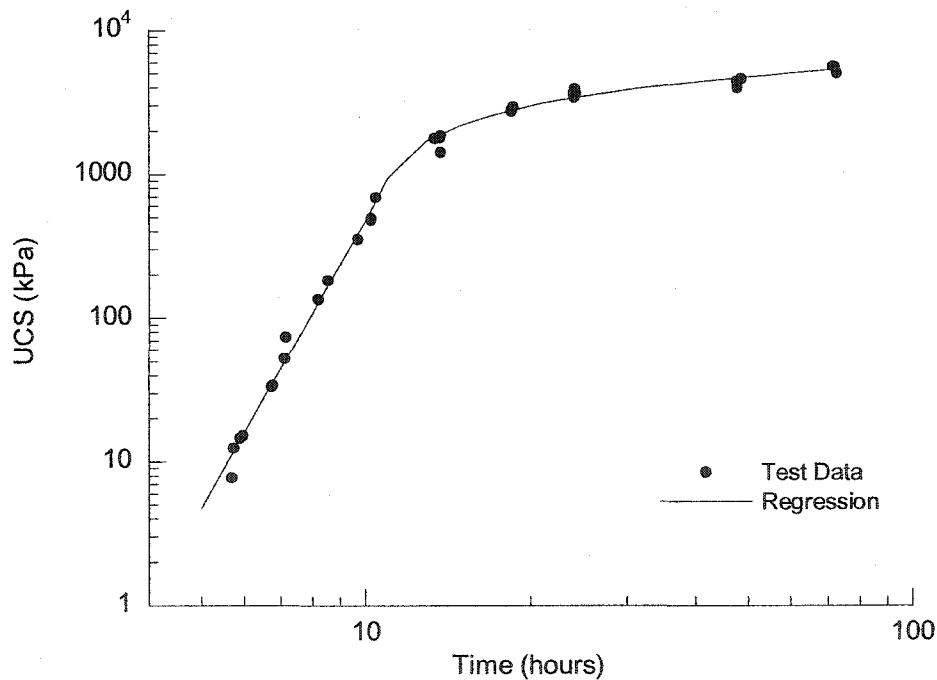


Figure 3.2 - Unconfined compressive strength (UCS) of grout as a function of time

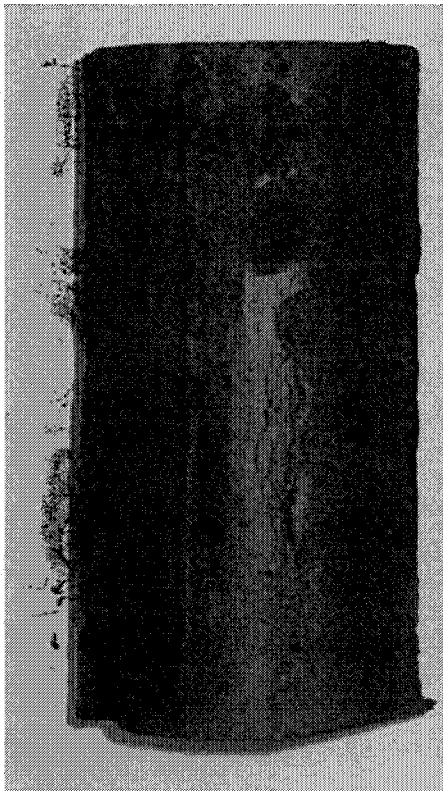
For the purpose of using the strength in a numerical model, the relationship of strength with time was regressed with a least squares fit. Equation 3.2 represents the strength for times less than 10.5 hours. The coefficient of determination ( $R^2$ ) is 0.99. Equation 3.3

represents the strength for times greater than 10.5 hours. This equation was forced to have the same unconfined compressive strength at 10.5 hours as Equation 3.2. The coefficient of determination for Equation 3.3 is 0.97. The units for time ( $t$ ) are in hours and the units for unconfined compressive strength ( $UCS$ ) are in kPa. The decision to use 10.5 hours as the transition between curve fits was chosen because it appeared to be the time when the rate of strength gain began to decrease.

$$UCS = 1.088 \times 10^{-4} \cdot t^{6.638} \quad <10.5 \text{ hours} \quad (3.2)$$

$$UCS = 1380 \cdot \ln(t - 8.34) - 408.7 \quad >10.5 \text{ hours} \quad (3.3)$$

The 6 hour samples were very soft and careless handling would result in impressions of fingers due to the samples' weight alone.



6 Hour



10.5 Hour

**Figure 3.3 - Grout cylinders after unconfined compression testing**

### 3.4.2 Tensile Strength

The tensile strength development (Figure 3.4) can be seen to have a similar shape as the unconfined compressive strength development in Figure 3.2, but with a greater scatter in the data. The relationship between tensile strength and unconfined compressive strength is shown in Figure 3.5, and the ratio of tensile strength to compressive strength is 0.133. The 28 day tensile strength had a mean of 1.4 MPa and a standard deviation of 0.1 MPa. This gives a ratio of tensile strength to compressive strength of 0.1. The Brazilian tests for samples tested at all times resulted in the formation of a crack parallel to the direction of loading.

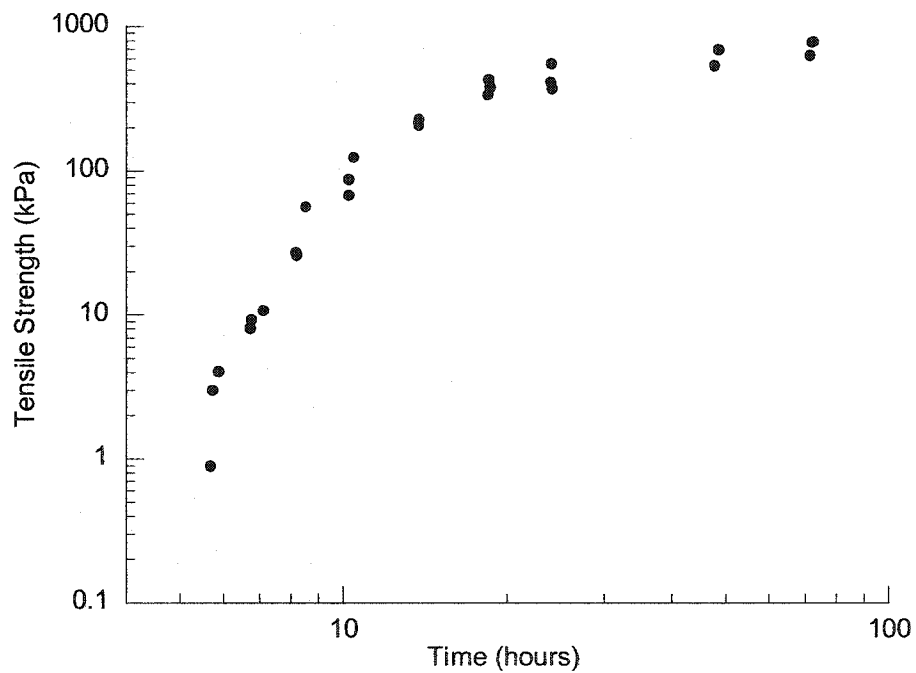
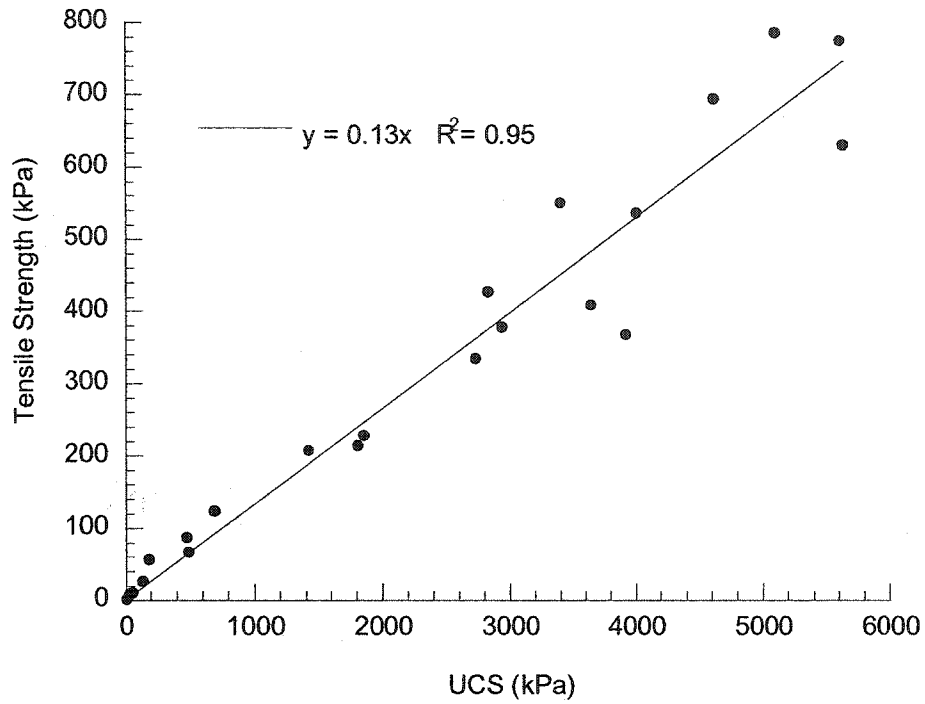
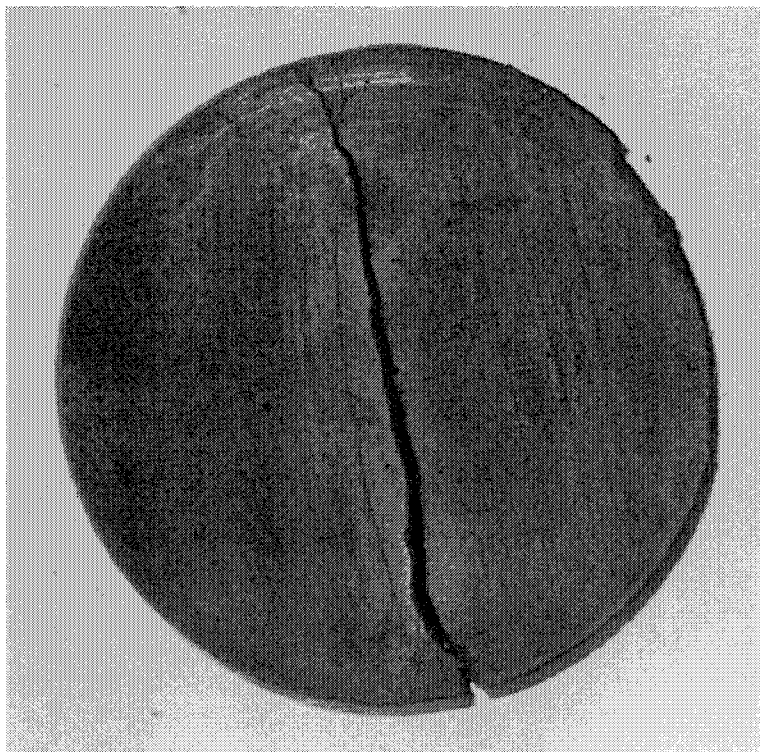


Figure 3.4 - Tensile strength of grout with time



**Figure 3.5 - Relationship between tensile strength and unconfined compressive strength for grout.**



**Figure 3.6 - Grout specimen after tensile testing**

### 3.4.3 Failure Envelope

The linear relationship between the tensile strength and unconfined compressive strength suggests that a Mohr-Coulomb failure envelope can be generated with the friction angle being independent of time. Using the regressed relationship of the tensile strength being 13% of the unconfined compressive strength, and the theoretical compressive stress at the center of the specimen in the Brazilian test being three times the tensile stress, the friction angle of the grout was found to be  $40^\circ$ . The cohesion is 0.23 times the unconfined compressive strength. The resulting failure envelope for a unitary unconfined compressive strength is shown in Figure 3.7.

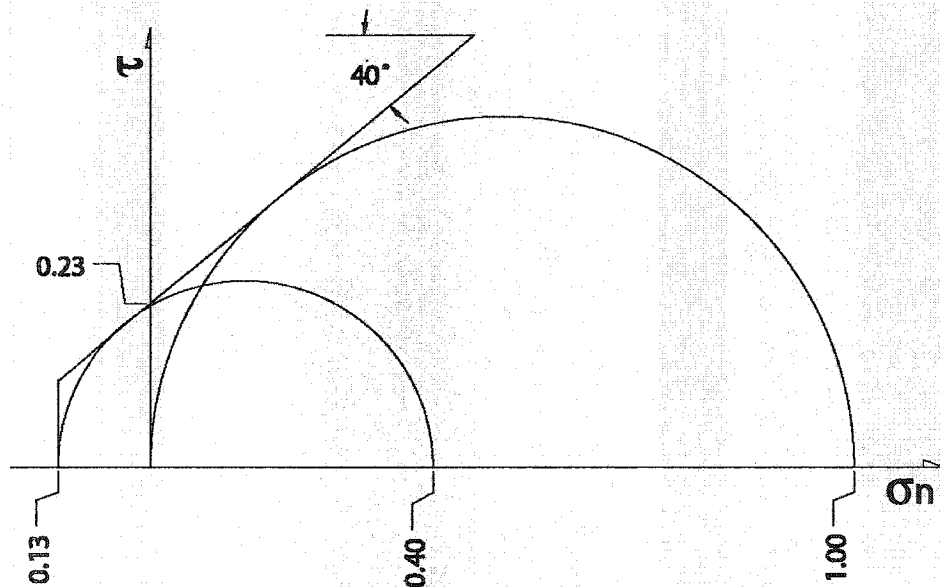
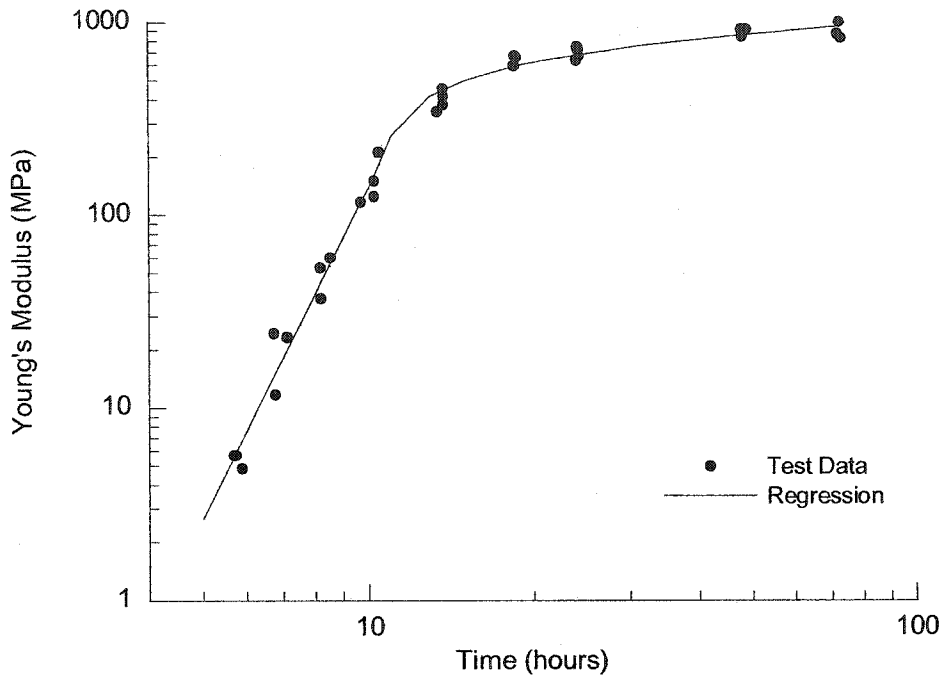


Figure 3.7. - Mohr-Coulomb failure envelope for grout

### 3.4.4 Young's Modulus

The Young's modulus was calculated as the tangent stiffness at 50% failure strain. The development of the Young's modulus with time (Figure 3.8) has a similar shape as the development of strength with time. The Young's modulus is observed to initially increase with time with a power type of relationship. This is seen as the straight line portion up to approximately 10.5 hours at which the rate of stiffness gain is at its greatest. Following this the rate of stiffness gain slows with time. This is observed as the curved portion when the time is greater than 10.5 hours.



**Figure 3.8 - Young's modulus of grout as a function of time**

For the purpose of using the Young's modulus in a numerical model, the relationship between stiffness and time was regressed with a least squares fit. Equation 3.4 represents the Young's modulus for times less than 10.5 hours. The coefficient of determination is 0.97. Equation 3.5 represents the stiffness for times greater than 10.5 hours. This equation was forced to have the same stiffness at 10.5 hours as Equation 3.4. The coefficient of determination for Equation 3.5 is 0.95. The units for time ( $t$ ) are in hours and the units for the Young's modulus ( $E$ ) are in MPa. Again the decision to use 10.5 hours as the transition between curve fits was chosen as it appeared to be the time when the rate of stiffness gain began to decrease.

$$E = 2.775 \times 10^{-4} \cdot t^{5.697} \quad < 10.5 \text{ hours} \quad (3.4)$$

$$E = 184.3 \cdot \ln(t - 9.51) + 183.7 \quad > 10.5 \text{ hours} \quad (3.5)$$

The relationship between strength and stiffness is shown in Figure 3.9. The Young's modulus follows a power type of relationship with the strength. This relationship can also be seen in the stress-strain curves in Figures 3.10 & 3.11. These figures clearly show that the failure strain increases with increasing peak strength, illustrating how the rate of strength gain is greater than the rate of stiffness gain.

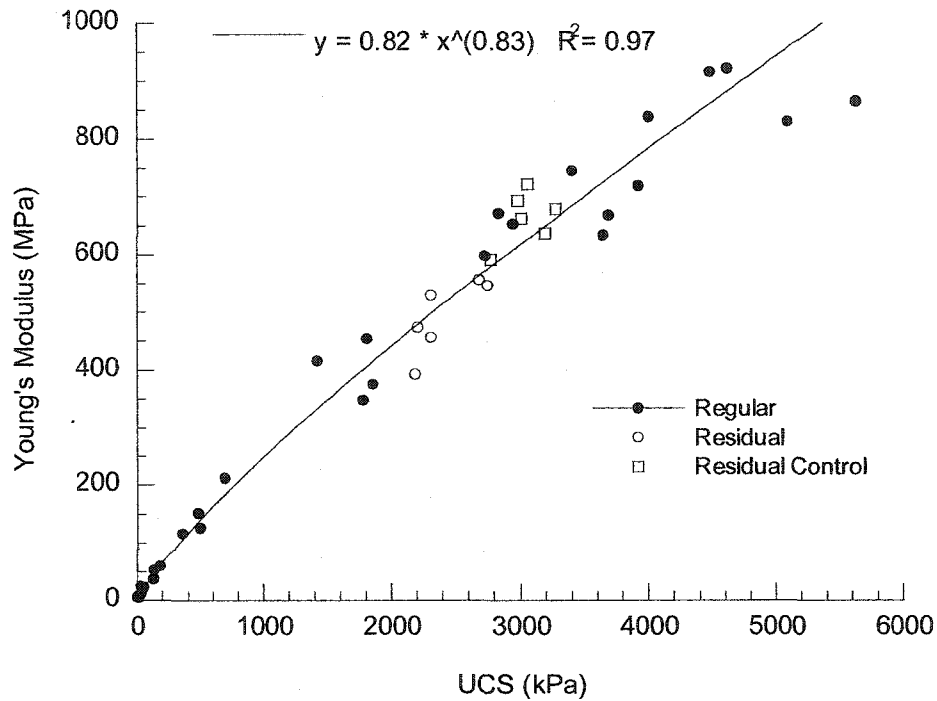


**Figure 3.9 - Relationship between strength and stiffness**

The stress-strain behavior of the early samples, those tested at times less than 10.5 hours or less, is shown in Figure 3.10. These samples have a ductile post-peak behavior. The transition to a brittle type of failure seems to occur at 10.5 hours, when the unconfined compressive strength is approximately 650 kPa. The samples that were tested at 10.5 hours or less remained in one piece that could be removed from the testing apparatus, whereas the samples older than 10.5 hours failed in a manner that when they were removed, the sample was in more than one piece.

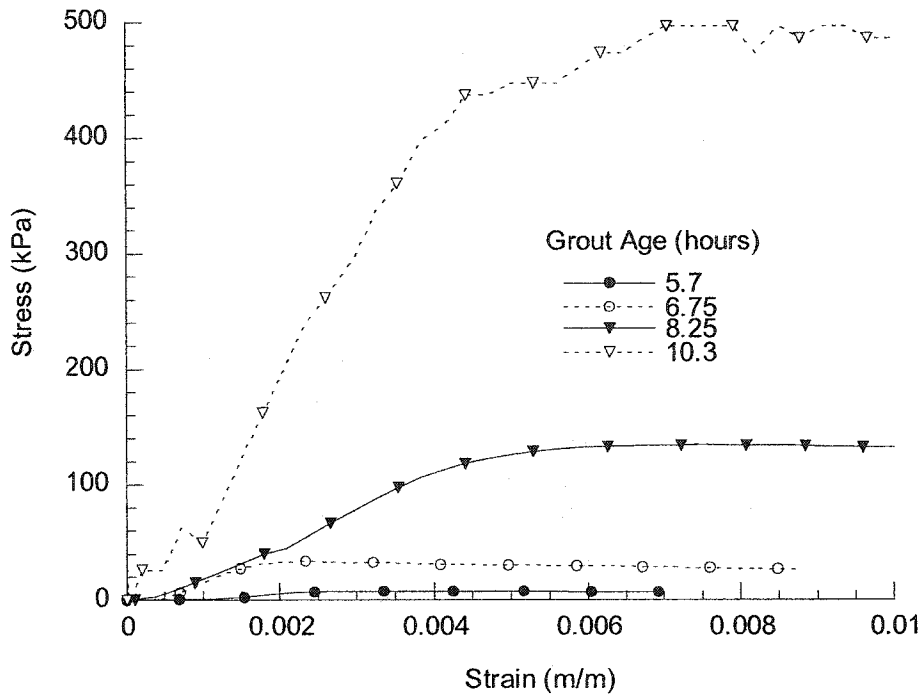


Figure 3.10 - Typical grout stress-strain curves for grout aged 10.3 hours or less

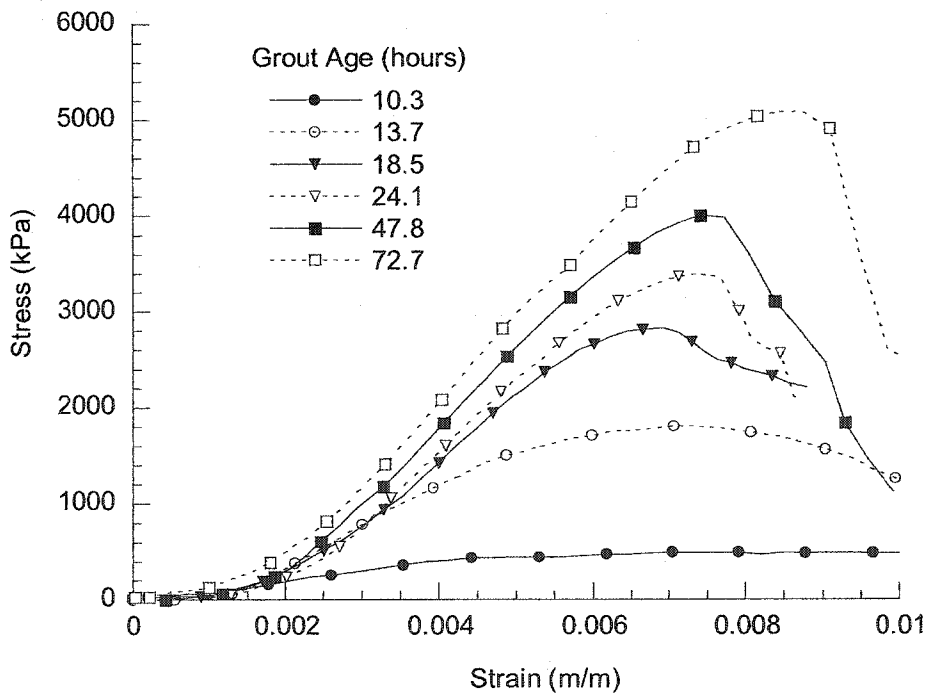


Figure 3.11 - Typical grout stress-strain curves for grout aged 10.3 hours or more



### 3.4.5 Heat of Hydration

The mean room temperature during the course of the testing was 8.3°C, with a standard deviation of 0.25 °C. As shown in Figure 3.12, the immediate hydration raises the grout temperature by 8.8 °C. This is followed by approximately 5 hours of steady temperature and then a significant temperature gain up to 15 hours with a maximum temperature gain of 22.2 °C followed by cooling. The rate of temperature gain reaches a peak value at approximately 11 hours as shown in Figure 3.13.

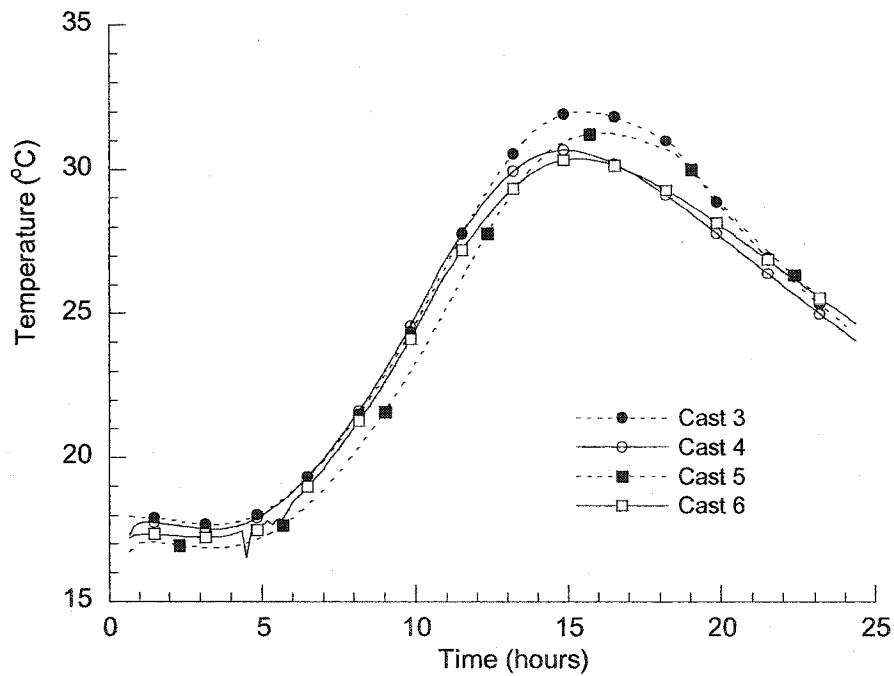
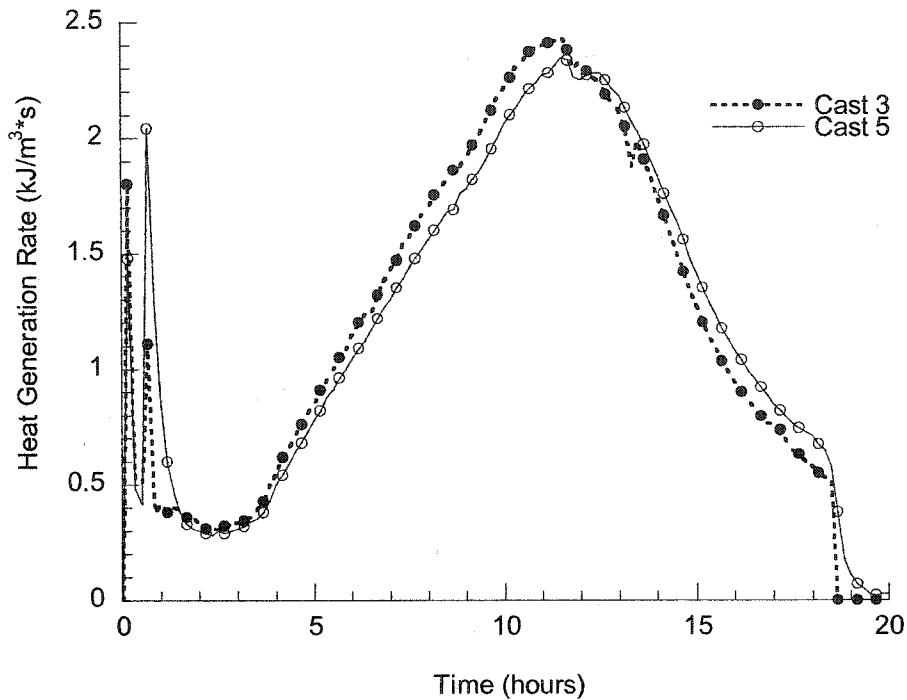


Figure 3.12 - Grout temperature change with time



**Figure 3.13 - Rate of heat generation of grout due to cement hydration**

The temperature gain data was used to back-analyze the heat generation rate and the total heat gain as illustrated in Figures 3.13 & 3.15. This was done using the finite difference procedure for radial heat flow described earlier. In this model of heat flow the heat generation rate was adjusted at each time step so that the grout temperature generated in the finite difference models matched the grout temperature observed during the laboratory tests. As before, the specific heat and thermal conductivity of the grout was assumed to be constant for all stages of hydration. While this may be a simplification, the results are useful in a qualitative sense.

The rate of temperature increase has the same general shape as the rate of heat generation. For the purpose of comparing the heat of hydration observed to other researchers accounts, the rate of heat generation provides a better comparison as it includes the heat that is lost from grout to the surrounding environment. The time of peak rate of temperature change of course corresponds to the peak rate of heat generation, this being at 11 hours. The deviation in form increases as the temperature difference between the grout and the environment increases, due to greater heat transmission rate at higher temperature gradients.

In Figures 3.14 & 3.13, the rapid drops in the rate of temperature gain and heat generation rate correspond to the removal of the 18.5 hour sample that was adjacent to the end of the 24 hour sample that had a thermistor at its end. At this point the heat flow deviates from a radial type due to the removal of the adjacent grout sample.

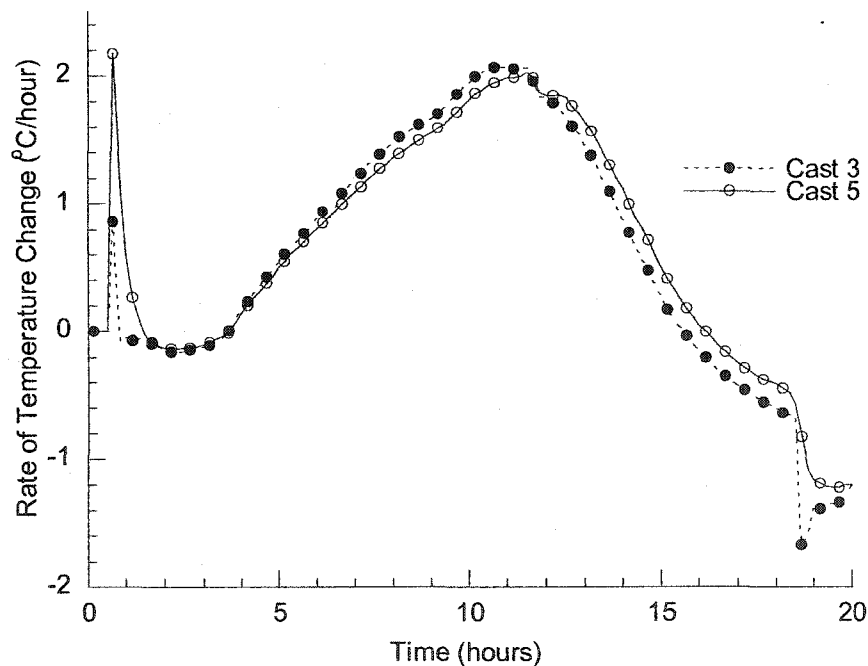
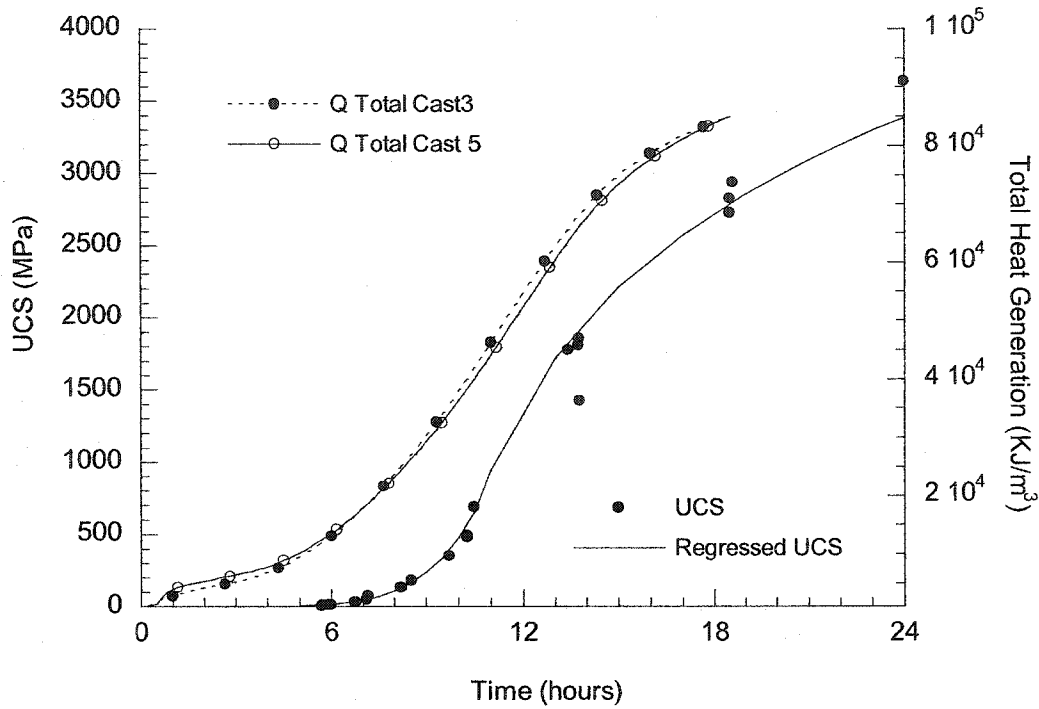


Figure 3.14 - Rate of grout temperature change of grout



**Figure 3.15 - Comparison between total heat generation and UCS**

The total heat generated due to cement hydration is related to the unconfined compressive strength (Figure 3.15). The difference between the initial development of strength at approximately 6 hours and the total heat generation may be explained by the need for sufficient hydration to occur before the gel starts to become connected between particles. At times less than 6 hours, the hydration doesn't contribute to strength gain because the cement gel is still discontinuous as it grows from surrounding the cement particles to interconnecting them. The energy required to do this corresponds to a total heat generation 10000 kJ/m<sup>3</sup> as shown in Figure 3.15. The analysis for the total heat generation relies upon the back analyzed values for the heat generation rate and thus has the same limitations and is mainly of qualitative use.

### 3.4.6 Residual Strength

The residual strength testing showed that the later that failure occurs, the less strength and stiffness will be recovered. Table 3.4 summarizes the residual strength tests. Because the samples were placed in the moisture controlled room at 6, 7 or 8.5 hours, the average temperatures that they experienced were lower than the temperatures experienced by the 24 hour samples allowed to cure in insulation. To account for this, Equation 3.3 was used to calculate the equivalent time that the residual samples has experienced. The equivalent time was calculated by taking the average strength at the 24 hour tests for each of the 6, 7 and 8.5 hour control samples and finding the corresponding time on the regression curve for each.

Although the percent retained strength appears to be greater than the percent retained Young's modulus, from the relationship between strength and stiffness illustrated in Figure 3.7, the residual strength and stiffness appears to follow the trend of the regular tests. The stiffness of the residual control tests appears to be generally greater than the expected trend (Figure 3.9). This may be due to the higher unit weight of these tests (Figure 3.17).

**Table 3.4 - Residual Strength of grout**

Test Time (hours)	Young's Modulus (% retained)	UCS (% retained)	Equivalent Time (hours)
6	88.0	94.0	20
7	74.1	75.2	22
8.5	61.8	69.6	24

### 3.4.7 Vane Shear Tests

The form of the strength development in the vane shear tests (Figure 3.14) is the same as the form observed for the unconfined compression tests performed at times 10.5 hours or less. This data can't be used in conjunction with the UCS data due to the difference in temperature history. The temperature of these samples was room temperature (approximately 20°C) whereas the average temperature in the first 5 hours in the insulated UCS tests was 17.4°C. The similarity of the forms may be of use in justifying the use of Equation 3.2 to extrapolate strengths at times less than tested. For example the use of a 2 kPa UCS at 4.4 hours may be used in modeling.

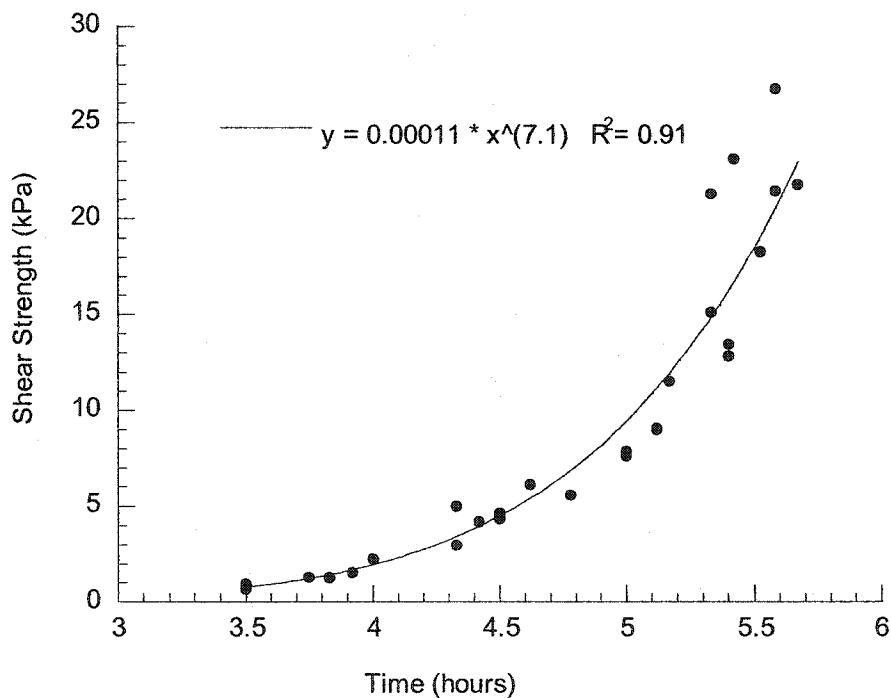
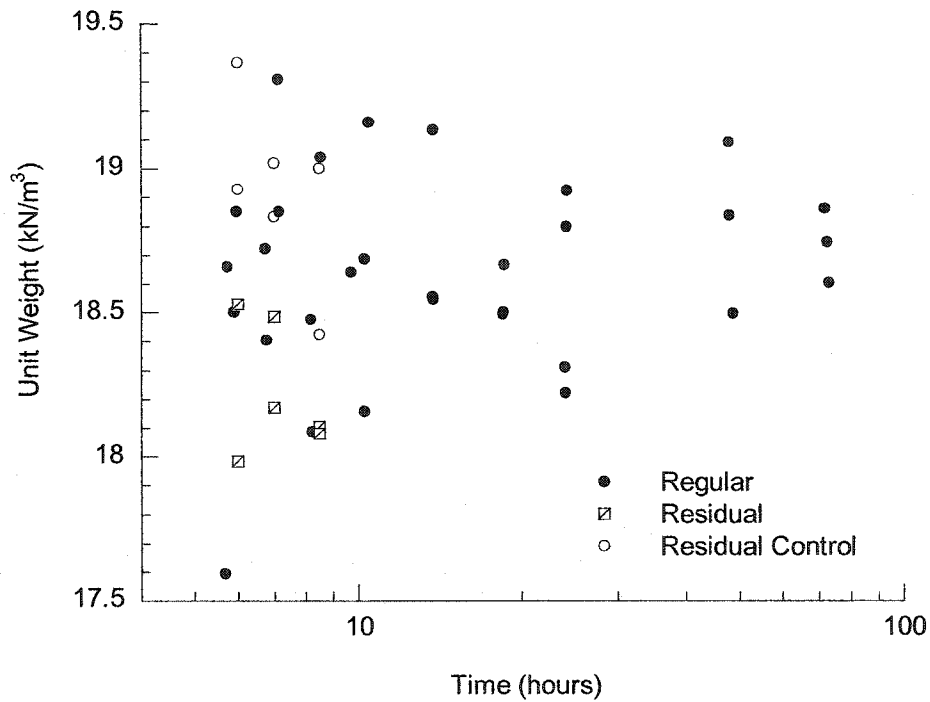


Figure 3.16. - Early strength development of grout measured with the vane shear test.

### 3.4.8 Grout Density

The grout density was calculated for all of the unconfined compression samples. The results are shown in Figure 3.17. The figure shows the initial weight for samples of different ages. There appears to be no significant bias that may result from the specimens having an undesired trend in the unit weight.

The regular tests are unconfined compression tests that were tested to failure and discarded. The residual tests and the residual control test are shown separately. The mean unit weight for the regular tests was  $18.8 \text{ kN/m}^3$  with a sample standard deviation of  $0.3 \text{ kN/m}^3$ . The residual control tests have higher unit weights than the residual control tests. The mean unit weights for the residual tests and the residual control tests were  $18.4 \text{ kN/m}^3$  and  $18.9 \text{ kN/m}^3$  respectively.



**Figure 3.17. - Density of grout samples**

### 3.5 Summary

The testing program determined the time and temperature dependent material properties for a grout column 600mm in diameter installed in sand.

From the laboratory testing program the behavior of the grout is summarized:

- 1) The unconfined compressive strength starts to develop approximately 6 hours after mixing. This is followed by a rapid increase in strength up to about 18 hours, where the rate of strength generation slows.

- 2) The tensile strength of the grout follows a similar development rate as the unconfined compressive strength. The linear correlation between tensile strength and compressive strength leads to the development of a Mohr-Coulomb failure envelope to be used in the finite element modeling stage.
- 3) The development of stiffness of the grout has a similar shape to that of the development of grout strength.
- 4) The shape of the heat generation curve closely resembles reported heat generation curves for the hydration of high early strength Portland cements. The delay between the generation of strength and stiffness and the generation of heat is due to the gel structure requiring an amount of development before it starts to become continuous. In addition the match in the expected shape and magnitude to the back-analyzed shape suggests that the finite difference approximations for the radial heat flow were reasonably accurate.
- 5) The residual tests for the samples that had failed before a brittle type of failure showed the ability to regain strength and stiffness. This was up to 90% for samples that had failed just after the onset of setting (6hrs) and 65% for 8.5 hour old samples after 24 hours.
- 6) There is no correlation between the unit weight and test time. Because it is known that higher density concrete will be stronger, this shows that there is no bias introduced into the tests from a systemic experimental error.



## 4 Aeschertunnel

The Aeschertunnel is a part of the Zurich west bypass project. This project is comprised of three tunnels that meet at the town of Wettswil, approximately 8km southwest from Zurich city center. The Aeschertunnel is comprised of parallel, two-lane highway tunnels passing under two chains of hills. The Basel axis lies to the north of the Luzern axis, carrying traffic in the direction of Basel, to the northwest, and the Luzern axis carries traffic in a southeast direction, towards Luzern.

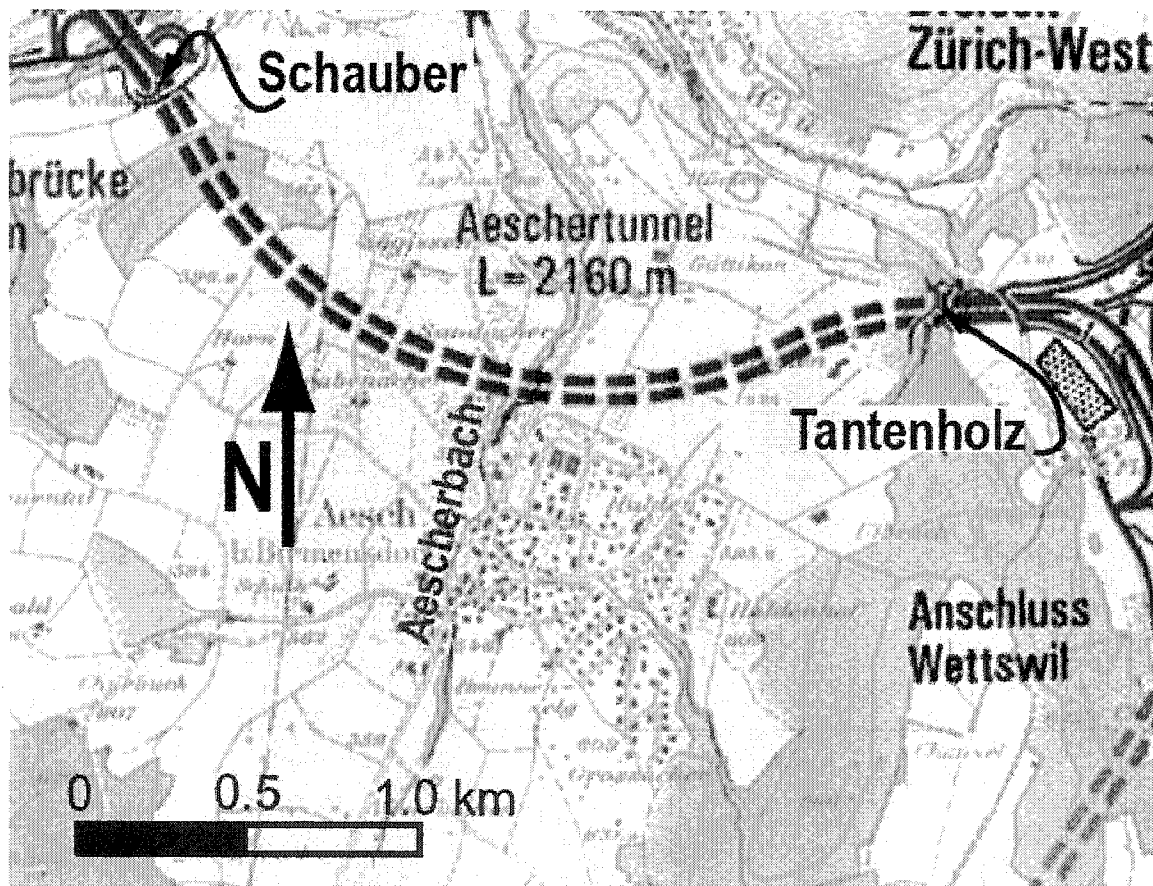


Figure 4.1 - Aeschertunnel route<sup>3</sup>

The Basel axis is 2055m long and the Luzern axis is 2090m long. The tunnels are spaced at 32m centerline to centerline, with up to 70m of overburden. The area of each

<sup>3</sup>Modified from;  
[www.westumfahrung.ch/html/index.html?wu\\_content\\_frame=/html/westumfahrung/projekt/birmensdorf/aescher\\_tunnel\\_plan.html](http://www.westumfahrung.ch/html/index.html?wu_content_frame=/html/westumfahrung/projekt/birmensdorf/aescher_tunnel_plan.html)

completed tunnel cross-section is 135m<sup>2</sup>, widening to 340 m<sup>2</sup> where there is an exit from the Basel axis. Excavation volumes are 360 000m<sup>3</sup> of bedrock and 245 000 m<sup>3</sup> of soil. The tunnels were driven using a heading and bench technique.

Construction of the portal and staging area commenced in early 1998 and the excavation of the tunnel started in mid 1999. The tunnels are expected to be completed by the summer of 2006. The tunnels are being driven from both the southeast (Tantenholz) and the northwest (Schauber) portals, with most of the tunneling from the southeast portal.

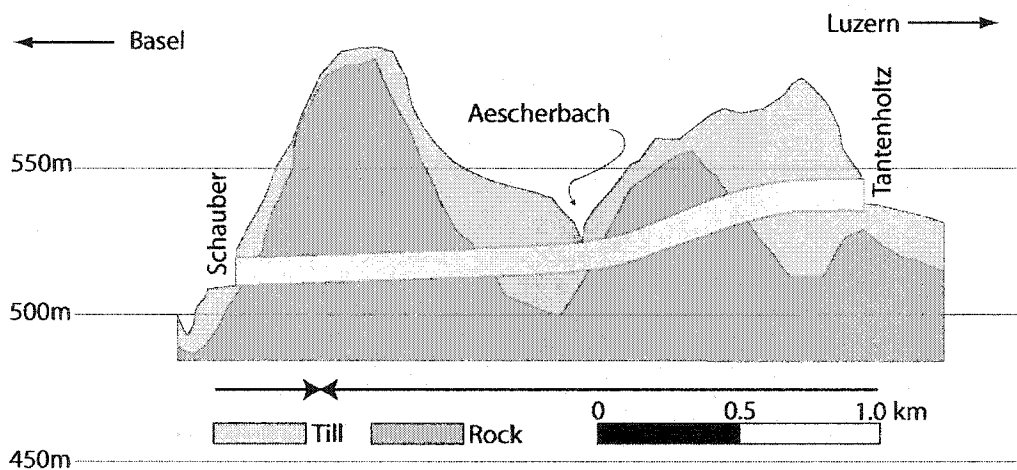


**Figure 4.2 - Aeschertunnel profile**

In May 2003 (the time of the data collection) the heading of the Basel axis was nearing completion, and breakthrough was close for the Luzern axis. At this time the bench had only limited excavation, at the southeast portal of the Basel axis and commencing from within the tunnel in the Luzern axis. Further reference to tunnel meters refers to the tunneling distance from the southeast portal.

In this section the settlement during jet-grouting, in particular soil and settlement profiles 1 and 2 at Basel tunnel meters 1000 and 1009, and Luzern tunnel meters 1013 and 1022 respectively (Figure 4.3), is reviewed. This corresponds to settlement points along F2 to F16 for profile 1, and F3 to F17 for profile 2 (Figure 4.7).

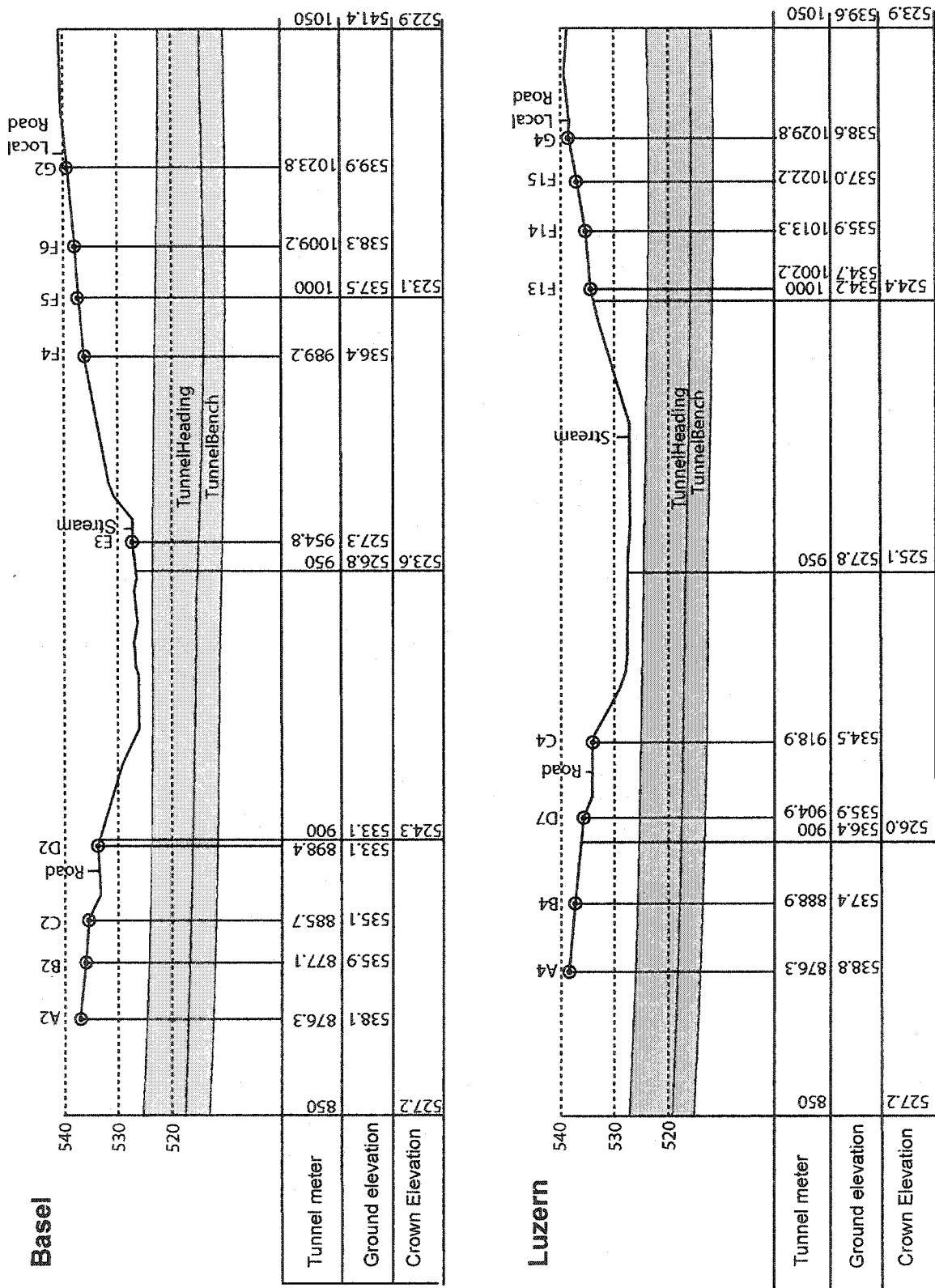


Figure 4.3. - Tunnel profile of the Basel and Luzern axes in the region of Aesch

## 4.1 Geology

The geology that the Aeschertunnel passes through is rock and soft ground. The rock type changes several times throughout the tunnel drive. The soft ground tunneling is in glacial till that is overlain by a sandy surficial deposit near profiles 1 and 2. Table 4.1 summarizes the depth of the surficial layers, till and depth to the bedrock and the tunnel crown.

**Table 4.1 - Depth to feature (m)**

	Till	Bedrock	Tunnel crown
Basel 1	6.9	36.3	14.7
Basel 2	7.7	37.9	15.5
Luzern 1	4.4	33.4	13.0
Luzern 2	5.4	35.4	14.2

### 4.1.1 Bedrock

The bedrock is layered sandstone, siltstone, marl and clay marl. The typical elastic modulus of the bedrock is 2 GPa. The swelling pressures in the bedrock were estimated to be between 100 and 180 kPa by the tunnel geologist. The typical parameters for the bedrock were estimated as; density of 25 kN/m<sup>3</sup>, a friction angle of 40° and cohesion of 1 MPa.

**Table 4.2 - Bedrock properties<sup>4</sup>**

	Density (kN/m <sup>3</sup> )	Friction angle (deg)	Cohesion (kPa)	Young's modulus (GPa)
Weathered Clayshale	22	14	25	na
Shale	24	28	2500	1
Siltstone	25	43	2500	12
Sandstone	25	49	4500	20

<sup>4</sup>personal communication with the Aeschertunnel project geologist, May 2003

#### 4.1.2 Till

The till consists of a lightly coloured clayey sand and silt, with gravel and isolated boulders. This soil is of glacial origin, and is hard and fairly homogenous. This layer is up to 35m thick between the hills, as shown in Figure 4.2. The tunnels intersect this layer between Basel tunnel meter 850 and 1300. The till was observed to be dry during the geological investigation and the tunnel excavation. Within the till there are water bearing lenses of silty sand and gravel, but the groundwater is perched on top of the till.

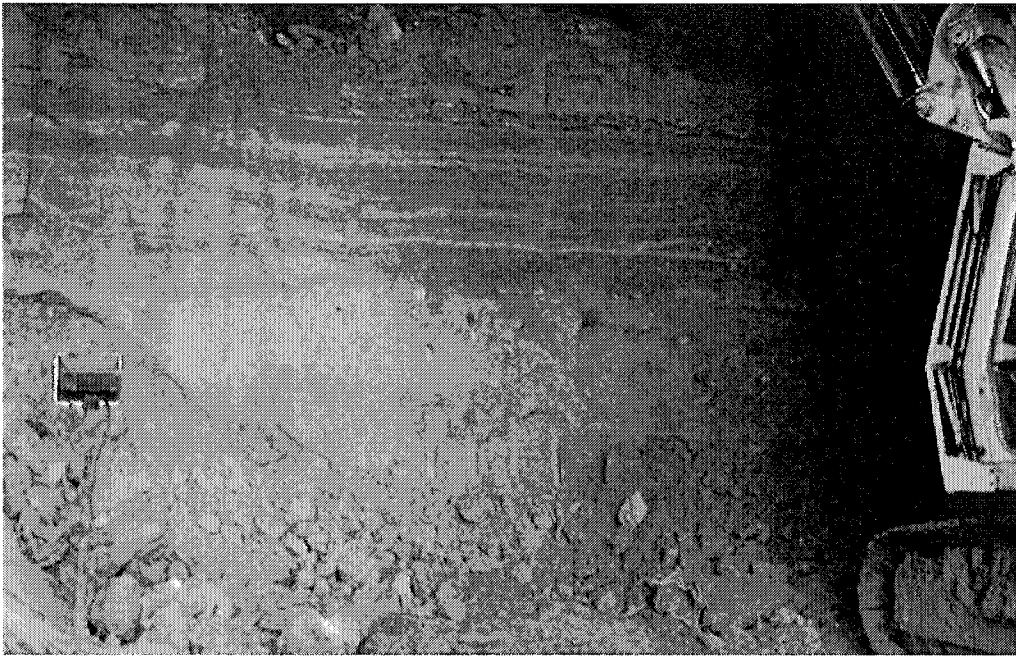


**Figure 4.4 - Excavation of the tunnel face showing the till**

The elastic modulus of the moraine ranges from 60 to 80 MPa. In the region near the stream, values of 80 MPa are typically reported. The calculation of the liner loads used the density as  $22 \text{ kN/m}^3$  and the friction angle  $32^\circ$ , with no cohesion. The typical strength of the till was assumed to be an effective cohesion of between 5 and 20 kPa, and a friction angle between  $30^\circ$  and  $33^\circ$ <sup>5</sup>. The layers of water bearing sands and silts in the moraine are cohesionless. The till was assumed to be at  $8.3^\circ\text{C}$ , the average annual temperature of Zurich<sup>6</sup>.

<sup>5</sup>personal communication with the Aeschertunnel project geologist, May 2003

<sup>6</sup><http://www.worldclimate.com/cgi-bin/data.pl?ref=N47E008+1102+06660W>, accessed Dec 3, 2003

The grain size distribution of the glacial till encountered in the excavation of the southern portal of the Eggraintunnel is presented in Figure 4.5. This tunnel is a part of the same project as the Aeschertunnel and is approximately 2km north of the Aeschertunnel. Due to the proximity of this tunnel the soil may be assumed to be similar.

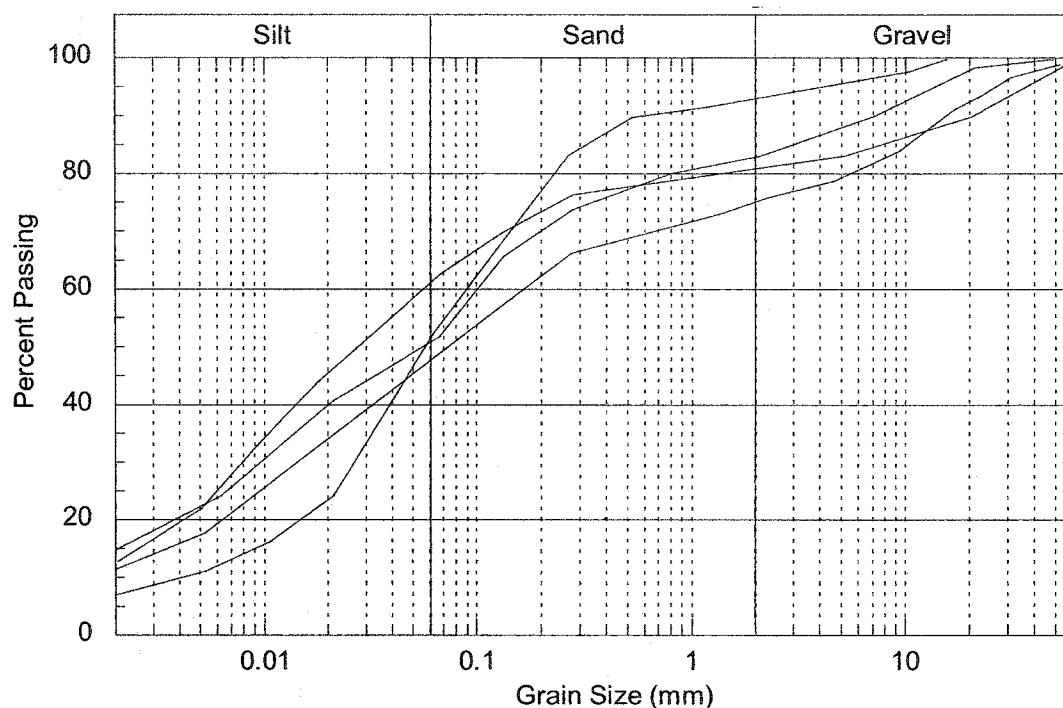


**Figure 4.5 - Grain size distribution from the Eggraintunnel (Kleboth 2000)**

Additional testing at the southern portal off the Eggraintunnel provided similar material properties to those reported in the Aeschertunnel. Fries (2000) reported an elastic modulus of 80 MPa, density of 23 kN/m<sup>3</sup> and a friction angle 35°, with no cohesion. Guntlin (2000) reported density of 22 kN/m<sup>3</sup> and a friction angle 32°, with no cohesion.

#### **4.1.3 Surficial layer**

From Basel tunnel meter 970 to 1250 the moraine is overlain by fine silty sand. This layer ranges from 0 m to approximately 10 m thick. Ground water is present in this layer, perched on top of the till. The density is 19 kN/m<sup>3</sup> and the friction angle 30°, with no cohesion<sup>7</sup>. This layer isn't present to the east of the stream.

<sup>7</sup>personal communication with the Aeschertunnel project geologist, May 2003

## 4.2 Instrumentation

Measuring of settlements commenced during the blade shield tunneling operation when it was suspected that the soil was losing strength in response to tunneling (Figure 4.7). Settlements were also measured in the region of the Aescherbach to assess the impact of these deformations on a roadway, a sewer line under the shoulder of the roadway, a concrete stream diversion channel, and nearby houses (Figure 4.8). Settlement points were arranged in a linear manner along the edge of the Aescherstrasse (road), along the edge of the concrete stream diversion channel, and a limited access road to the west of the channel. Settlement points were also located in a grid formation between the Aescherbach and the local access road and as the tunnels approach the Aescherstrasse from the east. In addition an inclinometer was installed on the slope between the local road and the Aescherbach.

Convergence points were installed at the tunnel crown and to the left and right of the tunnel crown during the placement of the shotcrete. The exact location of the left and right convergence markers was not recorded, but they are approximately below jet-grout columns 9 and 31 (Figure 4.6). Convergence measurements were taken after the installation of the shotcrete liner.

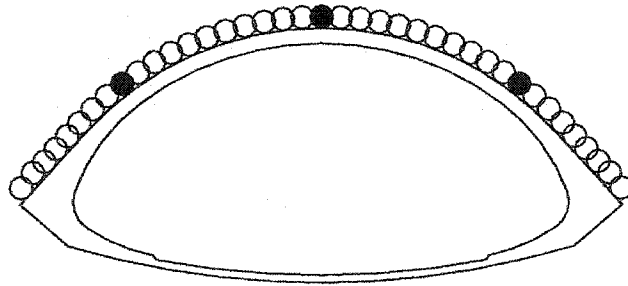


**Figure 4.6 - Location of convergence points**

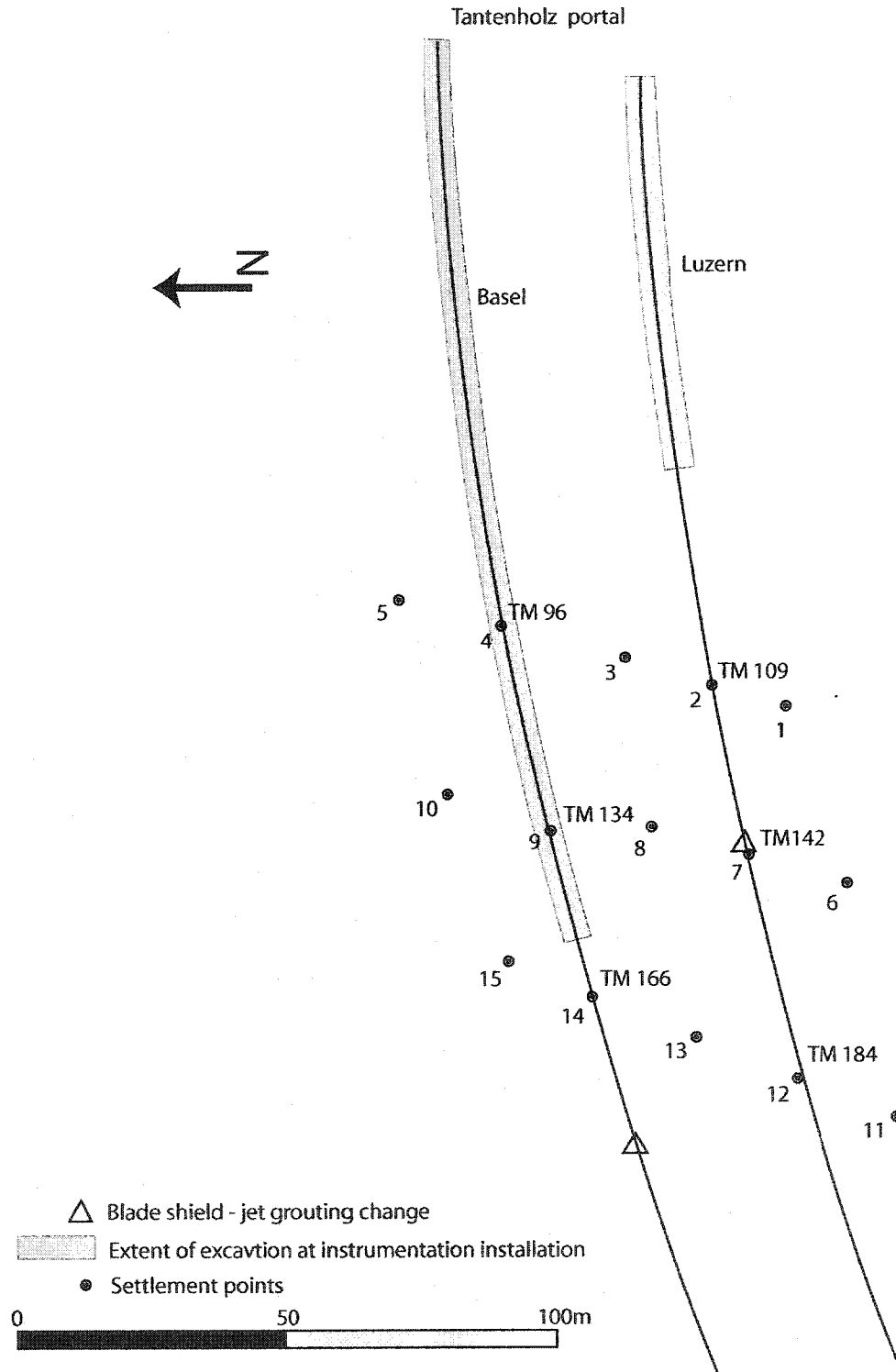


**Figure 4.7 - Plan view of the settlement points in the vicinity of the Tantenholz portal**



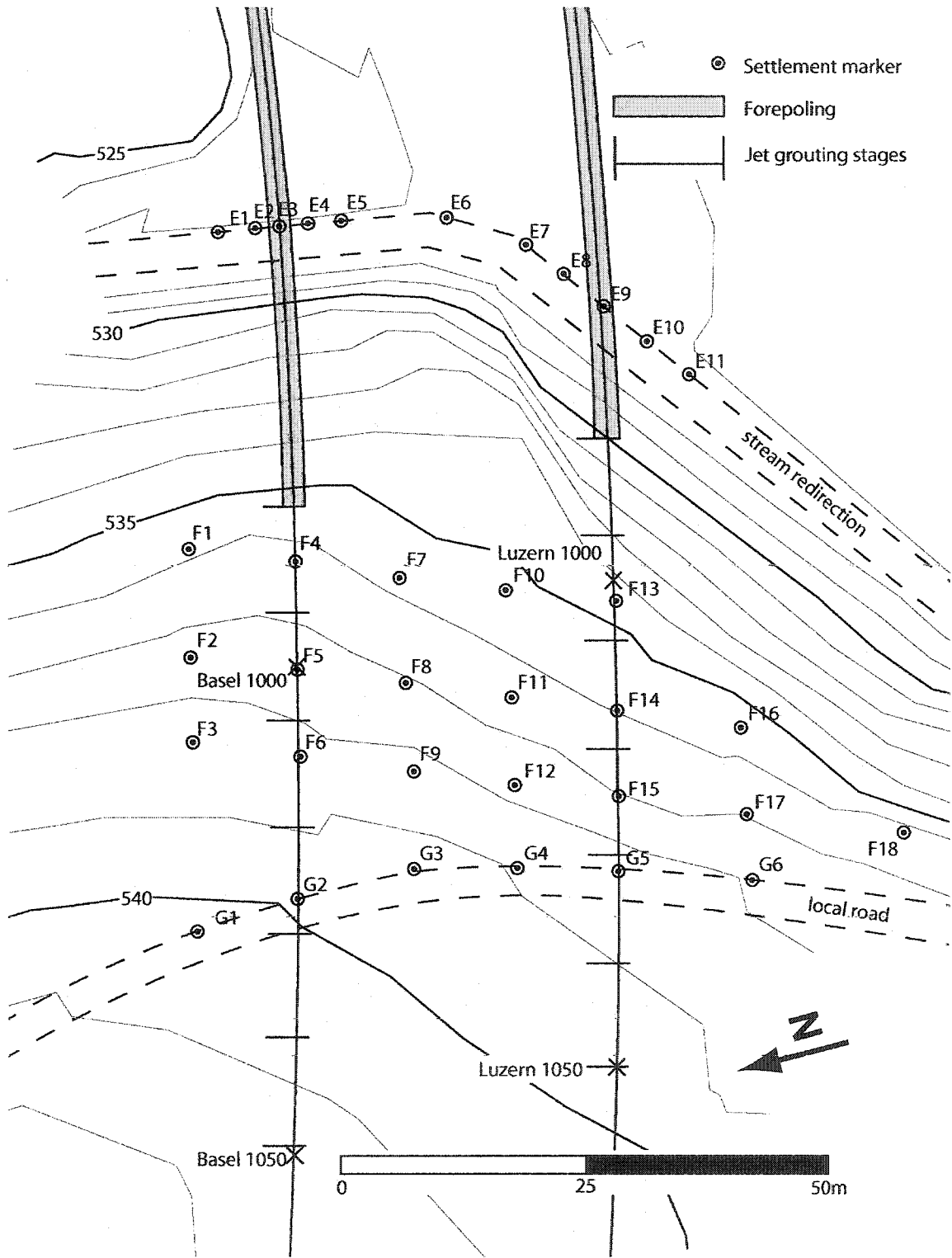


**Figure 4.8 - Plan view of the settlement points in the vicinity of Aescherbach**

### **3.3 Construction Methods**

#### **4.3.1 Rock**

The sections of the tunnels that pass through the bedrock were excavated by drill and blast. The rock was supported with pattern rockbolting and shotcrete.

#### **4.3.2 Fill area**

The tunnels' cross sections intersect the original ground profile in the Aescherbach valley, from Basel tunnel meter 923 to 953 and Luzern tunnel meter 933 to 963. This profile includes the original location of the stream. This necessitated redirecting the stream from its natural route with a concrete channel that passes over the tunnel excavation. The valley was filled to provide a new foundation for the stream and preserve the soil strength. The fill is made from concrete with very low cement to aggregate ratios and gravel aggregate.

Due to concerns that the ground may heave during jet-grouting, causing damage to the new stream channel, in the stages passing through the original ground profile in the fill and the following 2 stages, the preliminary tunnel support was provided with steel forepoles. The forepoling was installed in 13m lengths with 2m of overlap between stages. Each stage of forepoling was comprised of 46 steel poles, each 150mm in diameter. They are arranged symmetrically in an arc from  $-46^{\circ}$  to  $+46^{\circ}$  from the tunnel crown at 0.35m centers.

#### **4.3.3 Glacial till**

The construction technique in the till used both a blade shield and the installation of a jet-grout vault for excavation support.

#### 4.3.3.1 Blade Shield

Construction of the portal and staging area at the southeast end of the tunnel commenced in early 1998. The portal consists of a tangent pile wall secured by soil anchors. The tunnel excavation started in late summer 1999 from the southeast portal. The heading excavation commenced using blade shield for excavation support.



**Figure 4.9 - Tantenholtz portal (Southeast) showing tangent pile wall**

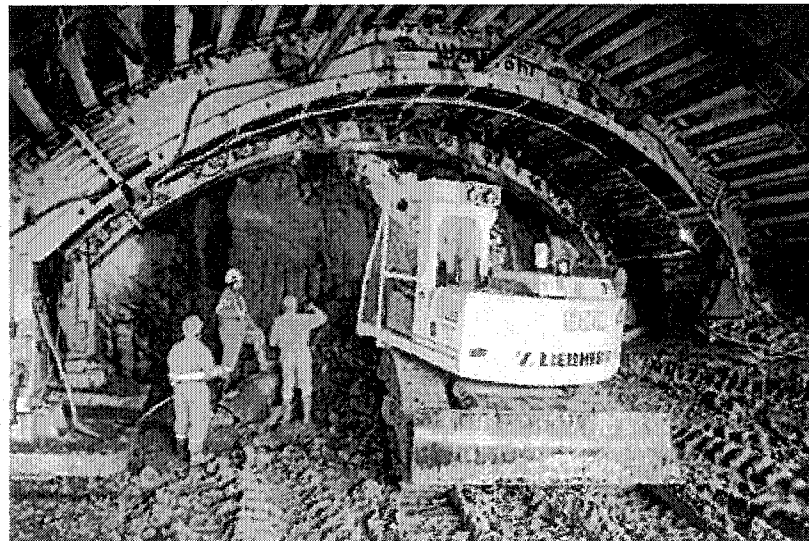


**Figure 4.10 - Blade shield use in heading excavation**

The concrete tunnel liner was cast immediately behind the shield. The bench was to be excavated as the excavation of the heading neared completion. Use of the blade shield was abandoned after the tunnel face became unstable and excessive surface settlements were recorded.

#### *4.3.3.2 Jet-Grout*

The blade shield construction technique was replaced with jet-grouting and Rodio (Italy) was employed as a specialist jet-grouting contractor. The jet-grouting method was to provide excavation support with an umbrella of sub-horizontal jet-grout columns to create a vault for the excavation of the heading. All future tunneling through the moraine, with the exception of the portion passing under the stream realignment, used this technique, resulting in the installation of approximately 90km of jet-grout columns.

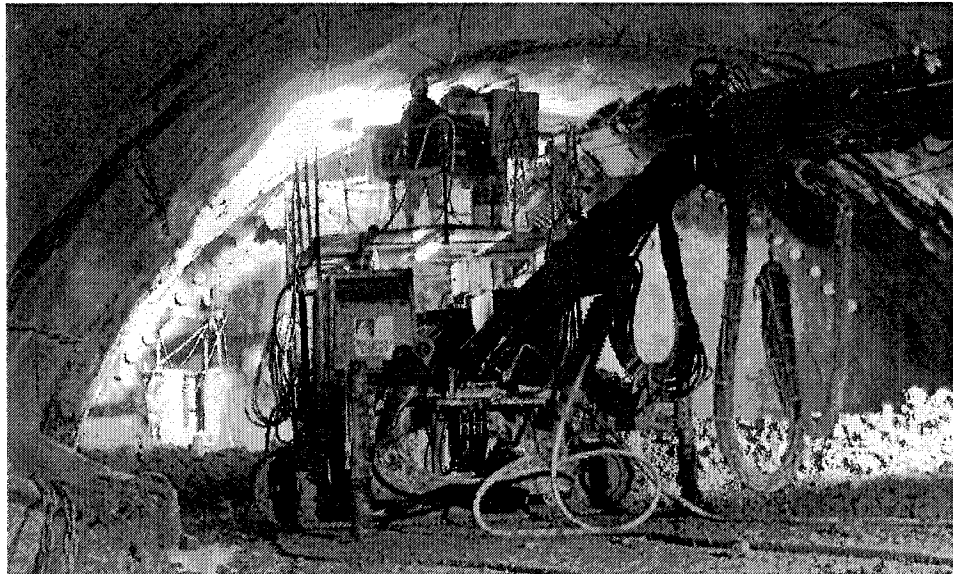


**Figure 4.11 - Jet-grouting installation in the tunnel heading**

The vault was formed with the installation of 35 to 39 jet-grout columns. The columns had a specified diameter of 600mm with a spacing of 450mm between the boreholes at the tunnel face to ensure overlapping columns. Each column was 13.0m long with 2.0m of overlap between stages, resulting in an 11m advance per stage. The columns were inclined  $11^\circ$  away from the tunnel axis to form a series of partially overlapping cone sections.

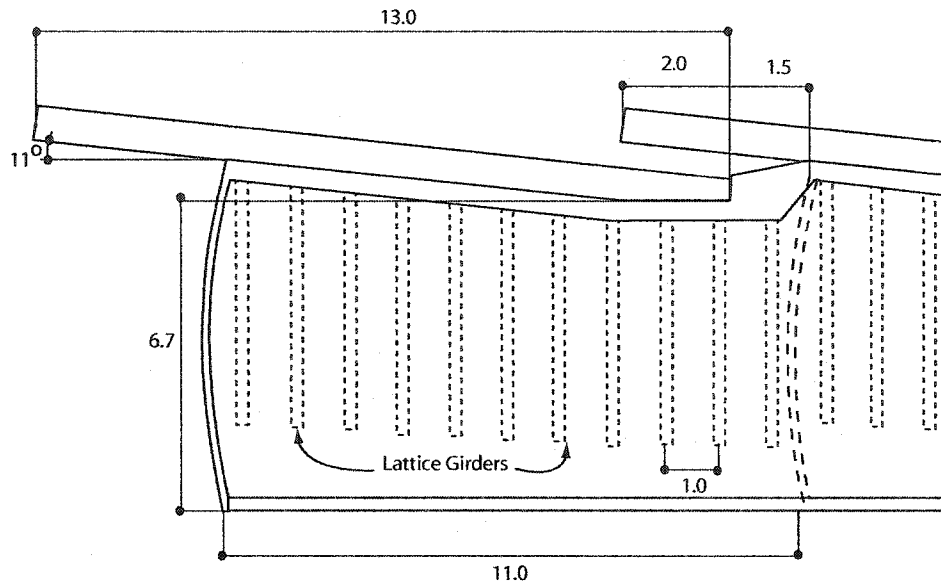


Figure 4.12 - Tunnel profile using jet-grout technique

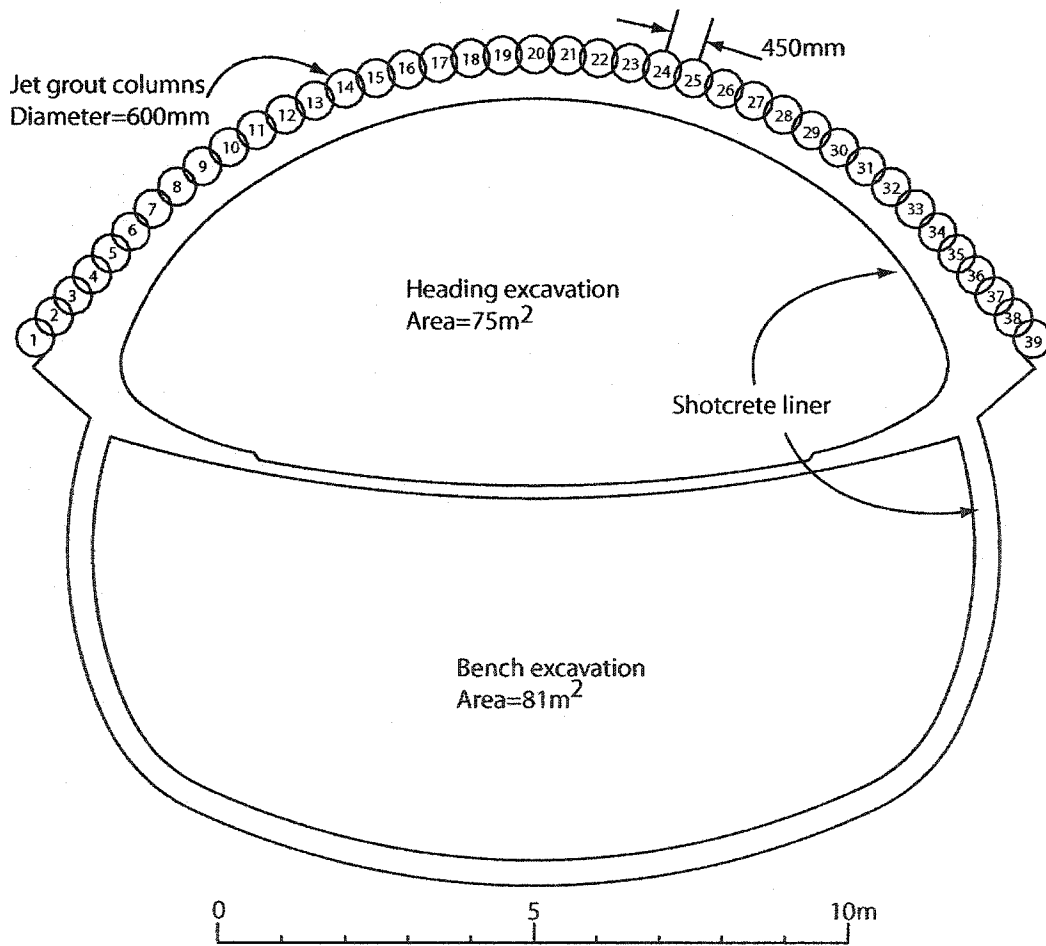


Figure 4.13 - Tunnel cross section using jet-grout technique.

Typically the crown was jet-grouted first, as this was speculated to produce the least amount of heave. The jet-grout installation was generally performed in a serial manner on the top set, i.e. columns 14 to 26, and then in a serial manner for 27 to 39 and then 1 to 13 (the sides). The average time to install a single jet-grout column took 39 minutes from the completion of the previous column for the stages passing through profiles 1 and 2. The sets of columns were generally installed within a 6-hour period, with the installation of all sets in 3 to 5 days. The remainder of the working shift would consist of removing the spoil from the tunnel. Each stage including excavation and installation of the preliminary liner stages typically took 8 days to finish.

The construction procedure for a stage is as follows;

1. Installation of the 35-39 jet-grout columns
2. Excavation of the tunnel face
3. Installing 2 layers of welded wire mesh and steel lattice girders and 400mm of shotcrete above the invert in 2m steps.
4. Closing the invert in 2 - 5.5m steps with welded wire mesh and 200mm of shotcrete.
5. Installation of 200mm of shotcrete on the tunnel face



**Figure 4.14 - Lattice girders prior to installation**

**Table 4.3 - Jet-grout sequencing and timing for Luzern profile 1**

Shift	Column numbers	Installation time (h)	Setting time (h)
1	27-14	6.9	19.3
2	1,3,5,7,9,11,13,39,37	4.9	12.8
3	38,36-29	5.8	64.9
4	2,4,6,8,10,12	3.2	

**Table 4.4 - Jet-grout sequencing and timing for Luzern profile 2**

Shift	Column numbers	Installation time (h)	Setting time (h)
1	16-23	6.2	66.0
2	7-14	6.2	18.3
3	31-24	5.3	11.8
4	39-32,1-6,15	11.2	

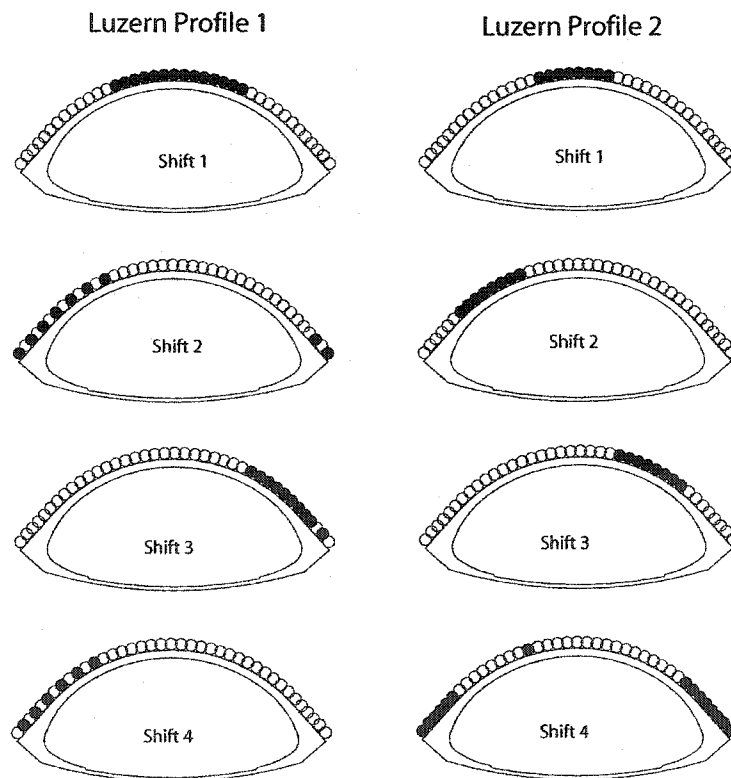


**Figure 4.15 - Jet-grout installation sequence for Luzern profiles 1 & 2**

**Table 4.5 - Jet-grout sequencing and timing for Basel profile 1**

Shift	Column numbers	Installation time	Setting time
1	28-23	3.9	39.1
2	10-19	8.5	20.8
3	8,9,20-22	2.9	69.3
4	39-29	6.2	17.8
5	1-7	4.2	

**Table 4.6 - Jet-grout sequencing and timing for Basel profile 2**

Shift	Column numbers	Installation time	Setting time
1	13-21,26-22	10.1	15.6
2	39-27	8.3	16.3
3	1-12	8.9	

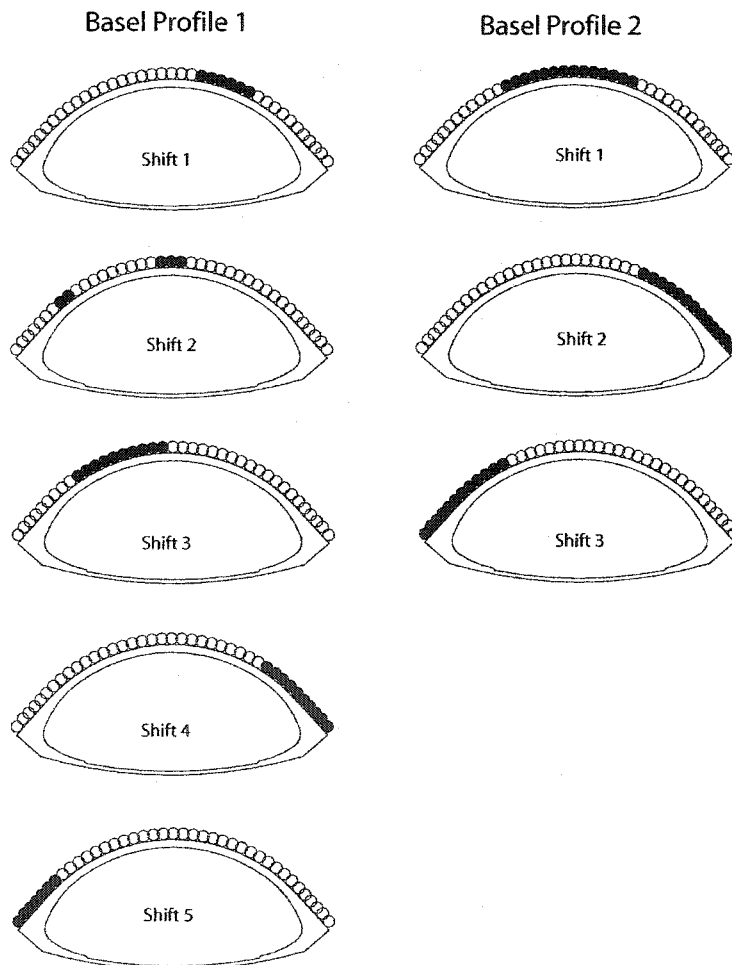


**Figure 4.16 - Jet-grout installation sequence for Basel profiles 1 & 2**



The time dependant development of strength of the shotcrete was determined by Electrowatt, the project managers (Figure 4.17). The 24 hour strength is approximately 20 MPa. The lattice girders composed of 2-20mm bars and 1-30mm bar. The welded wire mesh is 8mm diameter bars at 150mm spacing. The lattice girders and welded wire mesh are both constructed from steel with a yield strength of 550 MPa

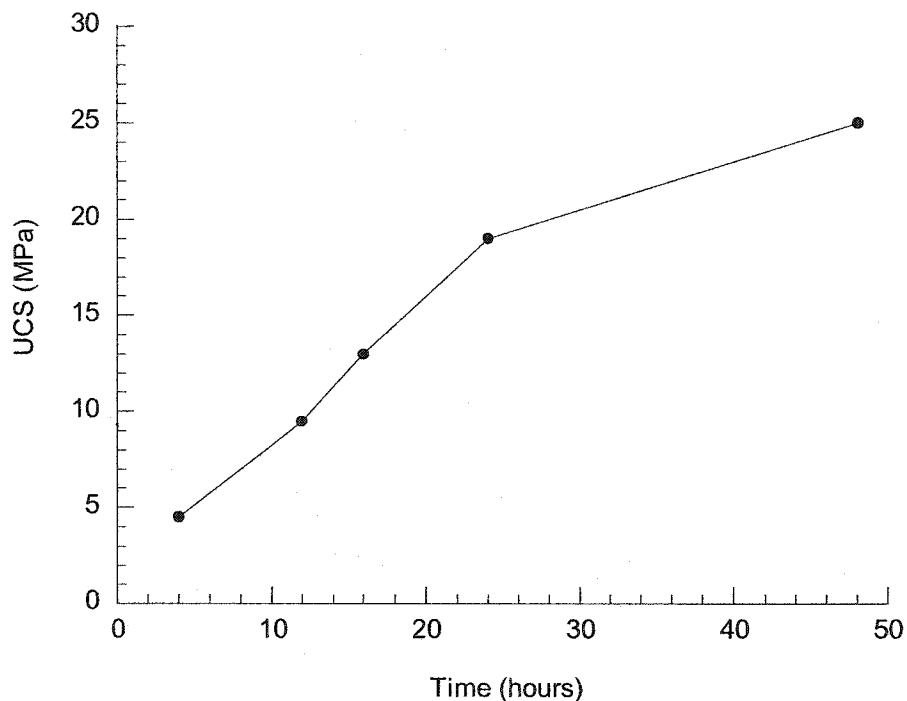


**Figure 4.17 - Development of shotcrete uniaxial compressive strength (UCS) with time**

The properties of the jet-grout used in the design of the Aeschertunnel had a Young's modulus of 2 GPa, cohesion of 300 kPa and a friction angle of 35°. Testing of 100mm diameter samples showed a density of 16 kN/m<sup>3</sup> and an unconfined compressive strength of 9.4 MPa at 28 days. The jetting parameters used during construction of the Aeschertunnel are shown in Table 4.7.

**Table 4.7 - Jet-grouting parameters during tunnel construction**

Parameter	Range
Grout pressure	40 MPa
Grout W:C	1:1
Drilling rod rotation rate	15 rpm
Withdrawal rate	0.5 m/min
Grout injection rate	12 m <sup>3</sup> /hour

## **4.4 Observations During Tunnel Construction**

### **4.4.1 Blade Shield Tunneling**

There were difficulties with using the blade shield. The axis of the blade shield was aligned angled above the axis of the tunnel in order to prevent the excavation from dropping below the desired position. This resulted in the formation of a larger gap at the tail of the shield, which in turn led to the greater soil displacements above the tunnel. These larger soil displacements are believed to have caused the ground to deform plastically and lose its original strength. When the ground softened, water was observed to be entering the tunnel. This was assumed to be due to the formation of fissures that extended to the perched water table in those deposits.

When the tunnel excavation was at Basel tunnel meter 153 and Luzern tunnel meter 71 on the 22<sup>nd</sup> of June 2000, instrumentation was installed to monitor the surface settlements due to concern that the till had lost a significant amount of its strength, possibly resulting higher liner loads. Excavation proceeded with the blade shield until Basel tunnel meter 205 and Luzern tunnel meter 142 on the 15<sup>th</sup> of August 2000. At this point the face in the Luzern axis collapsed and tunnel excavation was halted. The invert of the Luzern heading was closed with 300mm of concrete and steel girders were installed at 1m centers. Grout was injected behind the liners of both the Luzern and Basel axes in an attempt to restore the soil strength and limit further settlements.

Surface settlements were significantly reduced with the introduction of jet-grouting. Prior to the introduction of jet-grouting the centerline settlements approached 350mm at tunnel meter 74 (Figure 4.18). After the face collapse at Luzern tunnel meter 142 use of

the blade shield was replaced with jet-grouting, reducing the settlements to 80mm (Figure 4.19). Settlements were observed to be similar in the Basel axis, but the instrumentation was installed after the tunnel had passed or was very close to the settlement points.

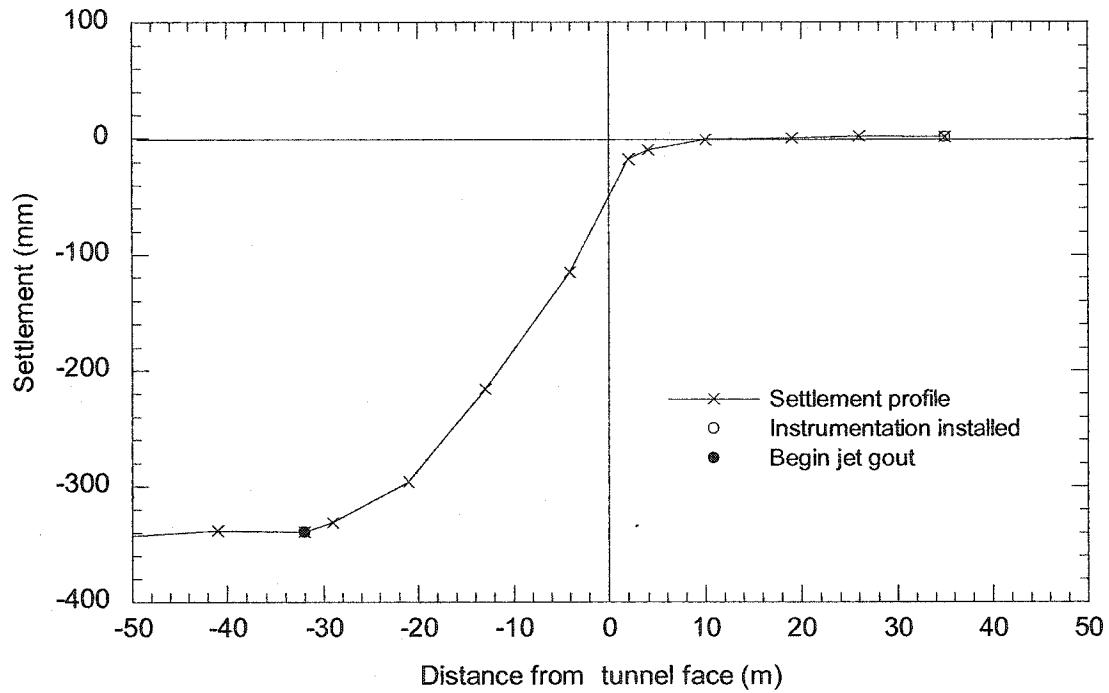


**Figure 4.18 - Settlement profile along the centerline using the blade shield at Luzern tunnel meter 74**

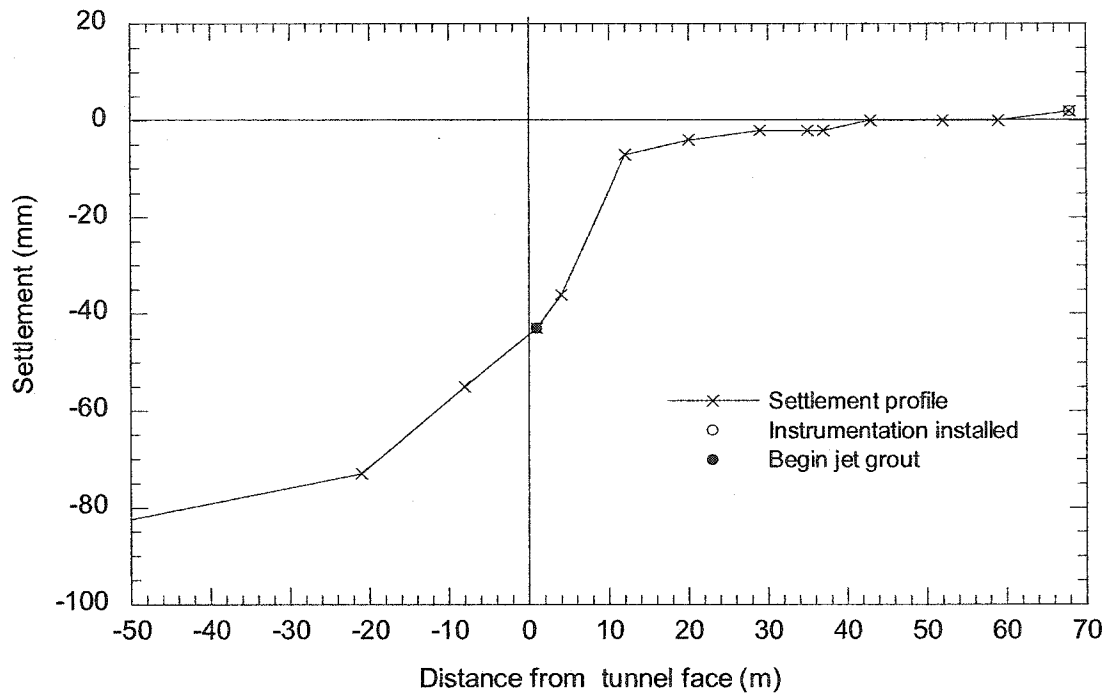


**Figure 4.19 - Settlement profile along the centerline using blade shield & jet-grout at Luzern tunnel meter 142**

**4.4.2 Jet-Grout Over-pressurization**

There were many observations that suggest that the jet-grout procedure induced pressures that exceeded the overburden pressures during the installation of the jet-grout columns. During the installation of the jet-grout columns heave was noticed where the Basel axis passed under the road. Grout was observed along the edge of the road and on the slope leading down to the valley from the road. When the jet-grouting recommenced, after the forepoling section to the west of the valley, grout was observed at the surface in many locations, up to 10's of meters horizontally from the tunnel axis. Grout was observed to spray from the top of the inclinometer casing when the installation of the jet-grout for the Luzern axis was performed to the west of the valley passing through the inclinometer casing.

Within the tunnel there was also evidence that the jet-grout procedure caused over-pressurization. The temporary shotcrete lining on the tunnel face collapsed during jet-grout installation, likely due to grout pressures building up at the tunnel face. The wooden borehole plugs intended for the retention of the grout were sometimes expelled and projected when adjacent jet-grout columns were being installed. On one occasion the grout pressures were sufficient to cause some steel lattice girders in the previous stage to buckle.

#### **4.4.3 Observed settlements when using the jet-grout technique**

The settlements observed during the jet-grout process were best recorded in the region of the Aescherbach, at Basel and Luzerne profiles 1 and 2, where approximately 30% of the settlement occurred ahead of the tunnel face (Figure 4.20). Nearly all of the settlement was developed 30m (3 tunnel diameters) behind the tunnel face and 30m ahead of the tunnel face the settlement was insignificant. The final settlements in profile 1 of both the Basel and Luzerne axes were smaller than profile 2. A normal cumulative distribution (CDF) was used to approximate the settlement profiles 1 and 2 using a least squares fit. The mean for the CDF in both cases was greater than zero, indicating that less than 50% of the settlement occurred ahead of the tunnel face.

**Table 4.8 - Normal distribution fit parameters for the centerline settlement measured at Profiles 1 and 2**

	F5, F14	F6, F15
$\sigma^2$	9.2 m <sup>2</sup>	9.6 m <sup>2</sup>
mean	2.3 m	3.3 m
$s_{max}$	25.2 mm	22.7 mm

At the locations 12m north and 12m south of the Basel axis the development of the settlement profile was more irregular than those measured at the centerline (Figures 4.21 & 4.22). Greater settlements were observed north of the Basel axis (towards the Luzern axis) and heaving of 2mm was observed in Basel profile 1 when the tunnel face was near the profile. This heaving may have been due to the installation of the jet-grout columns.

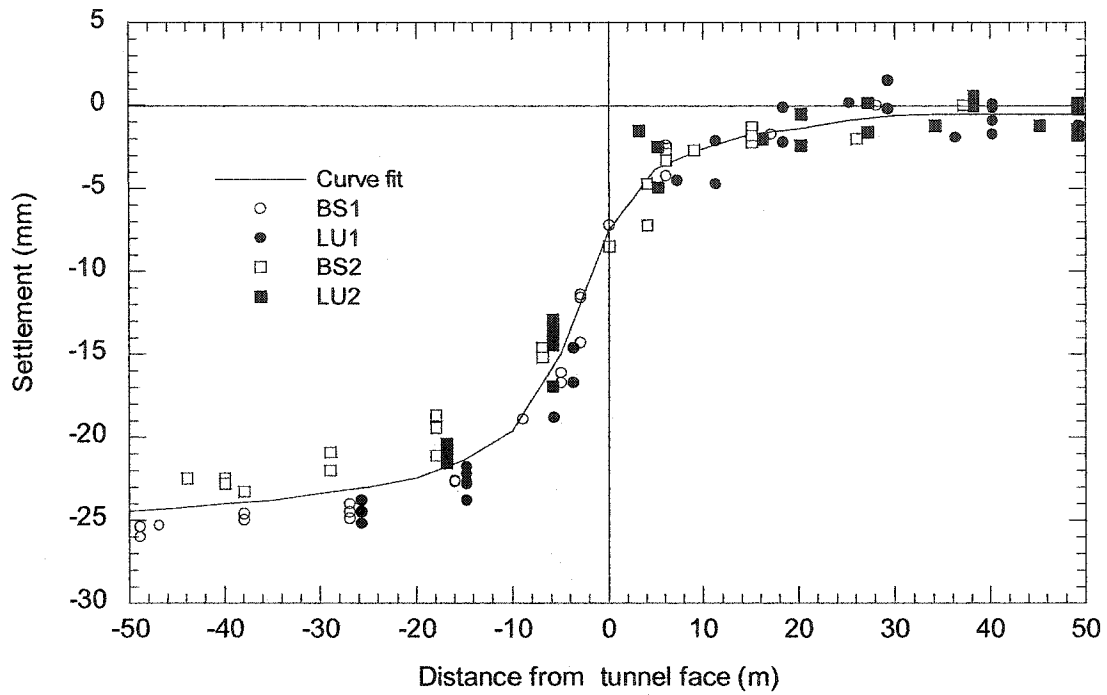


Figure 4.20. - Centerline settlement development – Profiles 1 and 2

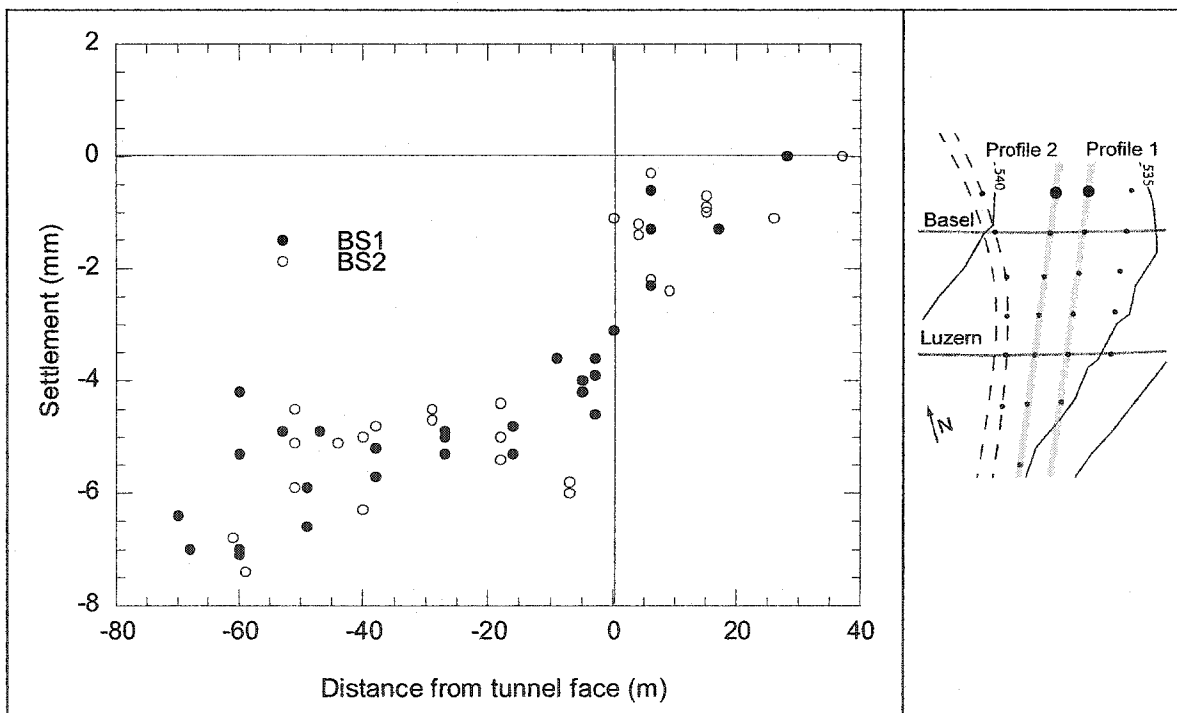
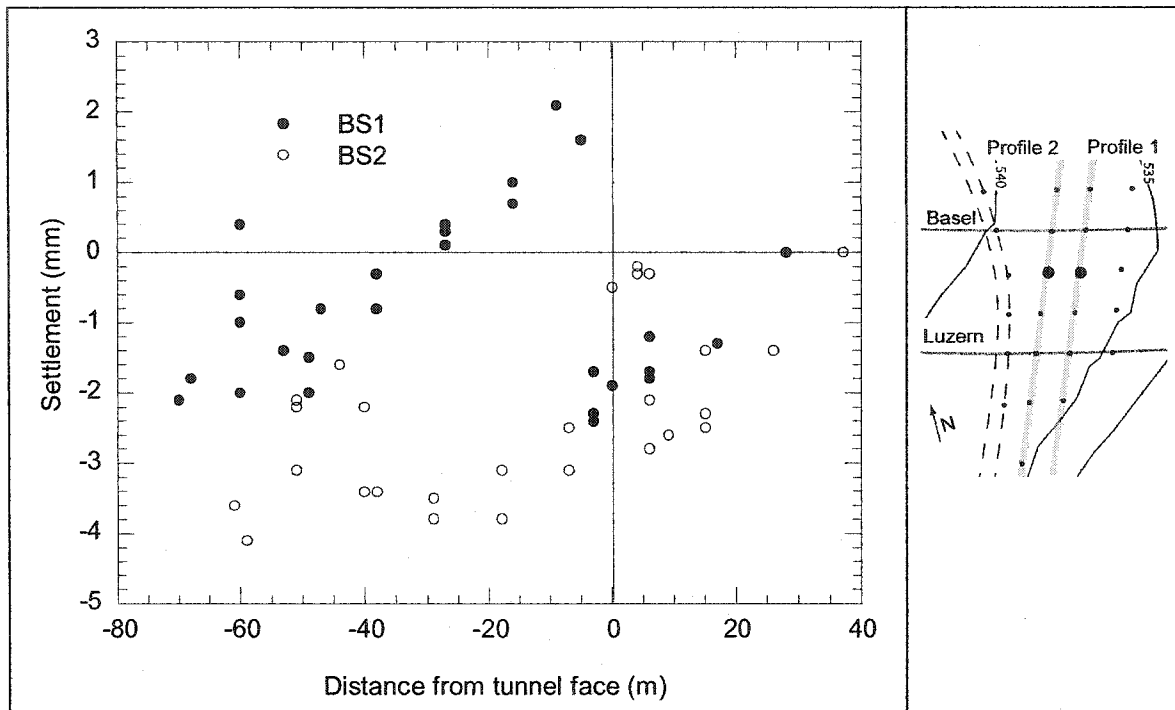


Figure 4.21 - Settlement Development 12m North of Basel axis



**Figure 4.22 - Settlement and heave measured at the profile 12m South of Basel axis. The heave was coincident with the installation of jet-grout.**

At the settlement point 20m south of the Basel axis, heaving of the ground was observed in both Basel profiles 1 and 2 when the excavation was within 10 m of the profiles (Figure 4.23). Basel profile 1 heaved 2mm and Basel profile 2 heaved 4mm. A drop of about 3mm was observed in both profiles about 40 m behind the tunnel face as the excavation of the Luzern axis passed through the profiles.

The Basel settlement profiles 32 m south of the Basel axis showed nearly no effect from the construction of the Basel axis (Figure 4.24). Because this settlement point is directly above the Luzern axis, settlements that of 25mm were observed after the excavation of the Luzern axis followed 40 m behind the Basel axis. At 12m south of the Luzern axis heaving was observed in both profiles 1 and 2 as the face of the Basel axis passed 40 to 50 m ahead of the excavation of the Luzern tunnel face, as seen in Figure 4.25,. Luzern profile 1 showed heaving of 20mm as the Luzern tunnel face passed through the profile whereas Luzern profile 2 showed no additional heaving (Figure 4.25).

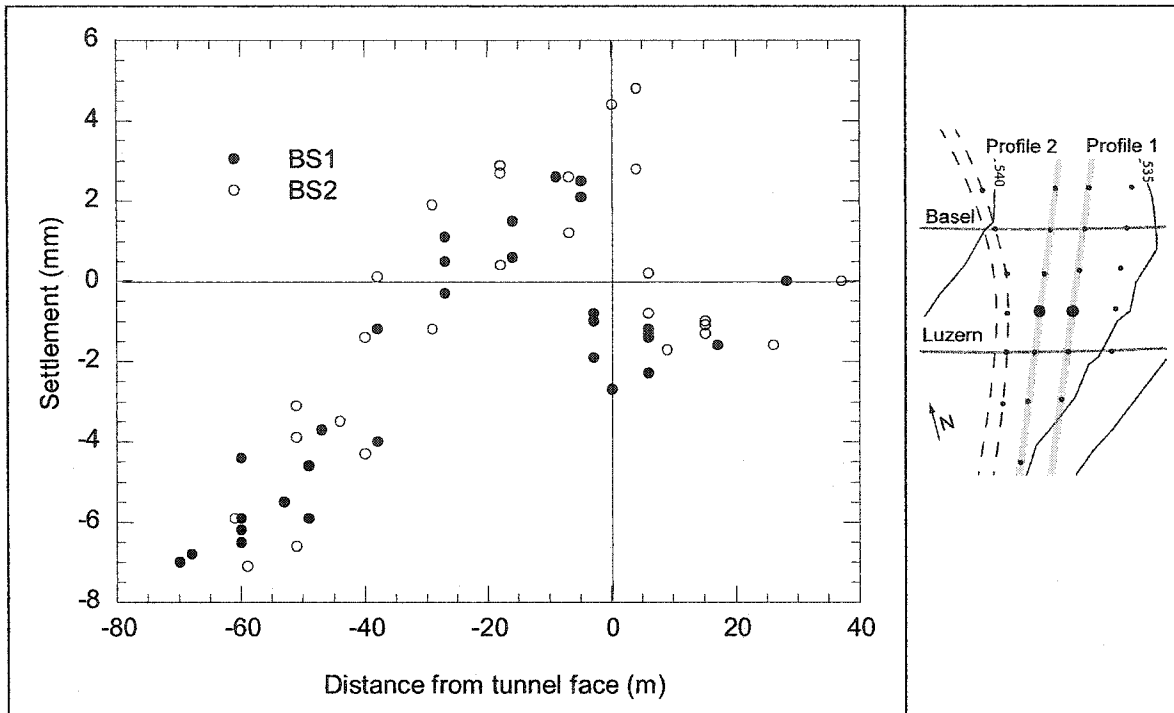


Figure 4.23 - Settlement development 20m South of Basel axis.

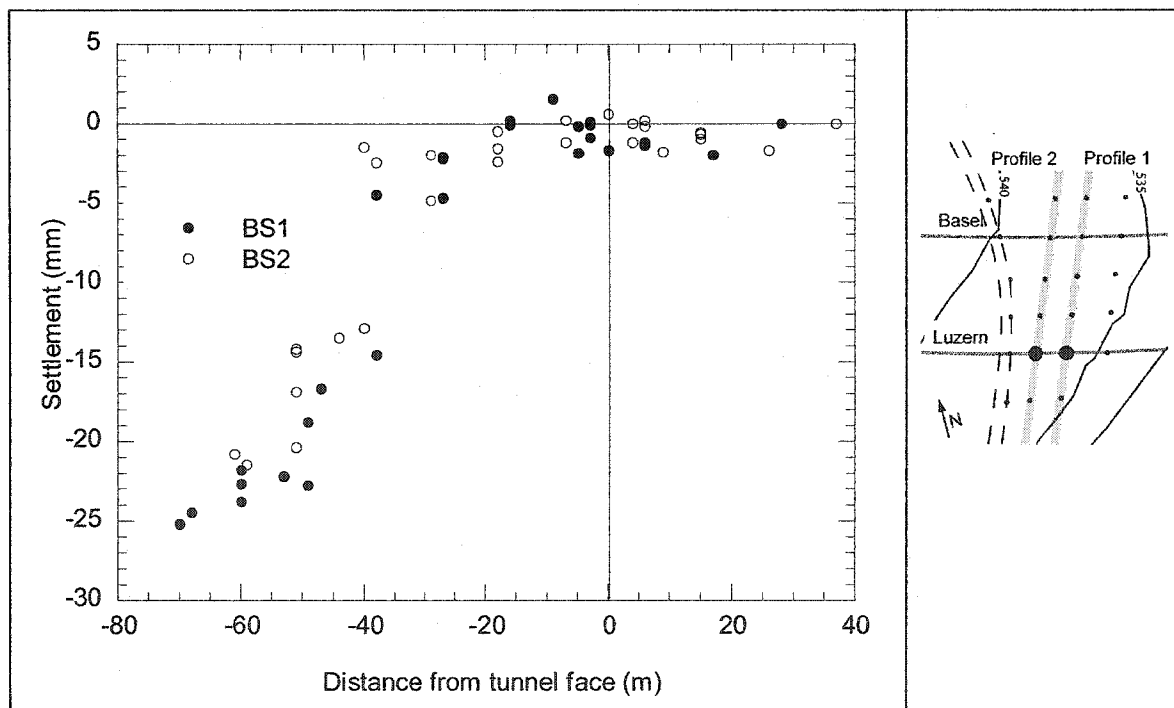
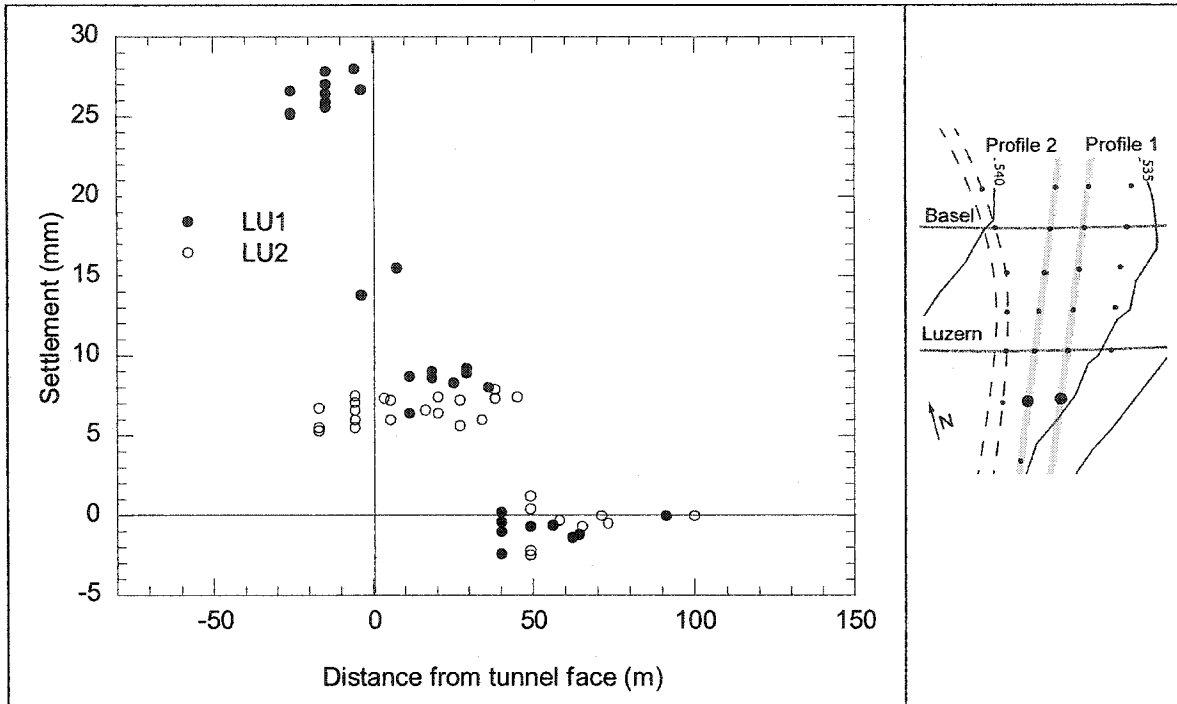


Figure 4.24 - Settlement development 32m South of Basel axis (Centerline Luzern axis)





**Figure 4.25 - Settlement development 12m South of Luzern axis**

Convergence measurements were taken at Basel tunnel meter 998 and Luzern tunnel meter 1022, corresponding nearly to Basel profile 1 and Luzern profile 2 respectively (Figures 4.26 & 4.27). The vertical displacements of the left and right measurement points are approximately 60% of the crown displacements for both the Luzern and Basel axes.

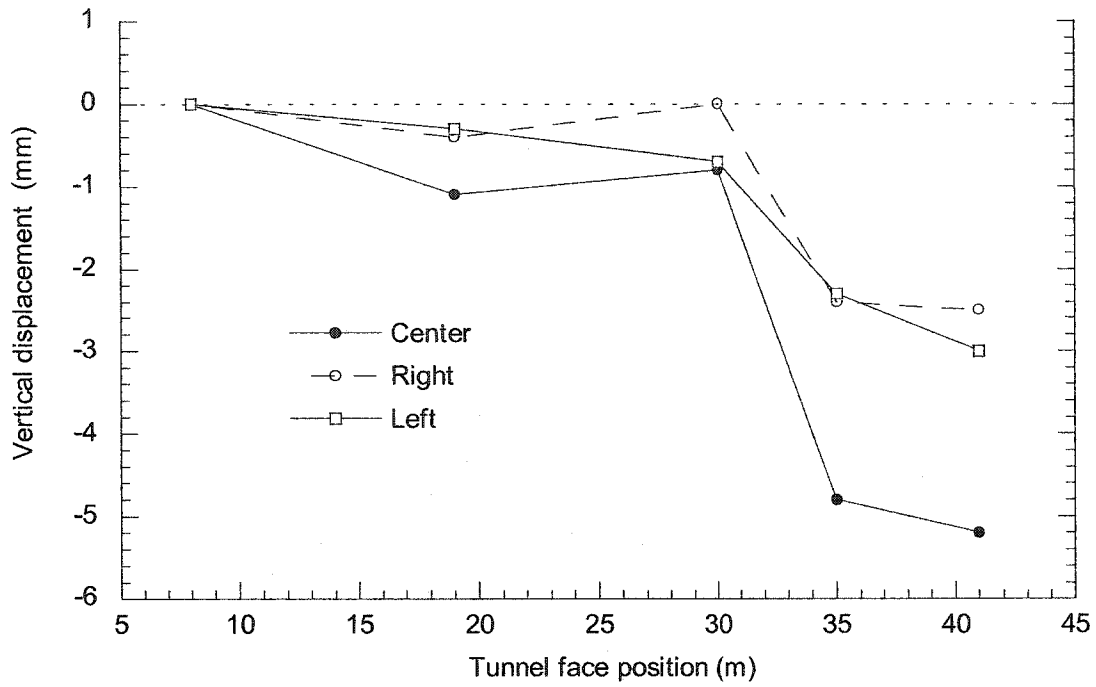


Figure 4.26 - Convergence – Luzern tunnel meter 1020

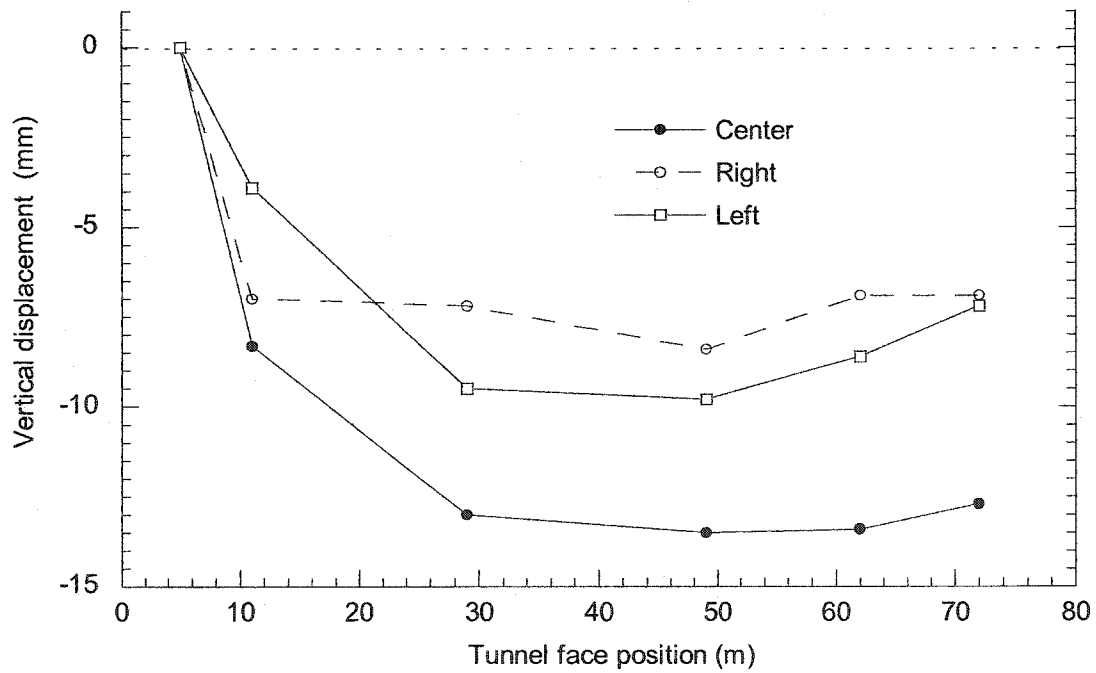


Figure 4.27 - Convergence – Basel tunnel meter 998

#### **4.5 Summary**

The field investigation covers the geology encountered during the construction of the Aeschertunnel, the construction procedures and observations. In particular it focuses on the jet-grouting construction procedures and surface settlements observed in Basel tunnel profiles 1 and 2. The following conclusions arise:

- 1) The use of a blade shield during excavation of the heading at the start of the tunnel construction led to excessive settlements and the collapse of the tunnel face.
- 2) During the installation of jet-grout, there was significant generation of pressures. These were large enough to cause hydrofracture and heaving of the ground, and localized yielding of the shotcrete liner and temporary shotcreting on the tunnel face.
- 3) The use of jet-grouting for preliminary excavation support resulted in a stable excavation face during excavation of the heading. Settlements were limited to approximately 25mm with 15m of overburden. The settlement ahead of the tunnel face was limited to 30% of the final settlements.

## 5 Analysis of Surface Settlements over the Aeschertunnel

There are three general methods for predicting the ground deformations associated with soft ground tunneling: (1) analytical methods, (2) empirical methods, and (3) numerical methods such as the finite element or finite difference techniques (Loganathan 1998).

Development of analytical techniques to determine the ground deformations is limited due to the difficulty of creating a general solution that satisfies the wide range of material properties, tunnel design and construction techniques. Sagesta (1987) presented an approximate analytical method for strain profiles due to near surface ground loss in a homogeneous, isotropic, incompressible ( $\nu=0.5$ ) soil in elastic half-space, and Verruijt (1996) expanded on the Sagesta's solution to include soils of any Poisson's ratio. This method still suffers from the downfall of most 2-D analyses as it over predicts the width of the settlement trough and the magnitude of the horizontal displacements. Because of the limitations of the analytical methods only the empirical and numerical methods were used for the analysis of the Aeschertunnel deformation described in this section.

The typical deformation patterns observed in Basel and Luzern profiles 1 and 2 had approximately 25 mm of settlement over the centerline of the tunnel. Approximately 17% of the maximum settlement occurred 12m horizontally from the tunnel axis in Basel profiles 1 and 2. The Luzern profiles both exhibited heave on the south side of the axis, (Figure 4.25, Table 5.1).

**Table 5.1 - Observed settlements, centerline and 12m north (12) and south (-12) of Basel & Luzern profiles 1 & 2**

		Basel 1	Basel 2	Luzern 1	Luzern 2
$S_{max}$	(mm)	-24.9	-23.8	-25.2	-20.8
$S_{12}$	(mm)	-5.3	-5.9	-7	-5.9
$S_{-12}$	(mm)	-2.1	-3.1	25.2	5.3

In this thesis a back analysis of the surface settlements over the Aeschertunnel was carried out using both an empirical method and a numerical method. This back analysis involved a simple curve fit for Peck's method and the systematic variation of the material parameters and construction techniques for the finite element analysis.

### 5.1 Back Analysis Techniques

The procedures that are used in the finite element back analysis of geotechnical problems can be divided into two categories: (1) the inverse, and (2) the direct approach (Swoboda 1999). With the inverse approach, the system of equations that govern the stress strain behavior of the model are written with the displacements as the knowns and the material properties as the unknowns. The advantages of the inverse method are that it exhibits stable behavior and converges to a solution quickly. The disadvantage with this method is the difficulty it has dealing with measurement errors and heterogeneity, in which case it may not converge to a solution.

#### *Direct Back Analysis Methods*

The direct approach uses trial values in a stress analysis algorithm. The advantages of the direct method are the simpler formulation of stress strain algorithms, and the much greater availability of commercially available FEM programs. The trial values are varied until the difference between the field observations and the numerical results converge to a minimum. This difference is often expressed as the sum of squared error.

$$SSE = \sum [u_i - u_i^*]^2 \quad (5.1)$$

Where  $u_i$  are the values of the field observations and  $u_i^*$  are the numerical results. Numerical search algorithms are often employed to search for this minimum. These algorithms can be separated into two categories: (1) direct search methods and (2) gradient search methods (Cooper 1970). Gradient methods require the evaluation of the directional derivative of the error function and shouldn't be used where the derivative of the error function cannot be evaluated (Box 1969; Beveridge 1970).

### *Direct Search Methods*

Direct search methods for finding the minimum value of an error function of multiple variables can be divided into two general categories: (1) simultaneous methods and (2) sequential methods (Beveridge 1970). With the simultaneous methods the error function is evaluated for the variables of interest over a sufficiently exhaustive range, whereas sequential methods use previous results to determine the starting values for the variables for the next iteration. The simultaneous search methods can be inefficient, requiring large amounts of computing time.

The univariate search, multivariate grid search and the direct search algorithms such as Powell's method are examples of sequential direct search methods (Beveridge 1970). The most common sequential direct search method, the univariate search, is performed by changing one variable at a time, finding the minimum of the error function successively for each variable. Once all of the variables have been searched sequentially the entire process of alternating the variables should be repeated. This search technique is very slow and can lead to false minima where there is a significant interaction between the variables. The multivariate grid search is a factorial design. With this method, the variables are assigned 2 values each, and the evaluation for the error is performed for all combinations of these variables. The evaluation with the least error becomes the starting point for the next iteration, with new values chosen for the variables. This method accounts for the possible interaction between variables.

The numerical search for the lowest value for the error function is continued iteratively until the solution converges or when the error function approaches sufficiently close to zero. Ensuring convergence is for a numerical solution isn't possible, so several criteria for stopping the search have been proposed (Beveridge 1970) i.e.; the search may be stopped when the difference in the value of the error function in successive iterations drops below a specified tolerance.

This thesis used a direct back analysis with direct search techniques (Powell's method and multivariate grid search) to find the best match between observed and modeled settlements.

## 5.2 Empirical Analysis

(Peck 1969) proposed an empirical method for assessing the shape of the settlement trough perpendicular to the tunnel axis. This approach fits a Gaussian (normal) probability density function to observed settlements, which is given by,

$$s(x) = s_{\max} \cdot e^{\left(\frac{-x^2}{2i^2}\right)} \quad (5.2)$$

where  $s$  is the settlement,  $s_{\max}$  is the maximum settlement, over the centerline,  $x$  is the horizontal distance to the centerline, and  $i$  is the horizontal distance from the centerline to the point of inflection of the settlement trough (Figure 5.1), and the area under the Gaussian curve is described as ground loss and is usually reported as a percentage of the cross sectional area of the tunnel.

$$V_l = \frac{\sqrt{2\pi} \cdot i \cdot s_{\max}}{A_t} * 100 \quad (5.3)$$

where  $V_l$  is the percent volume loss and  $A_t$  is the cross sectional area of the tunnel. When tunneling through clays the  $V_l$  is equal to the total ground loss due to the undrained (incompressible) conditions, whereas in a dilatant material such as dense sand the calculated  $V_l$  is less than the total ground loss (Mair 1997).

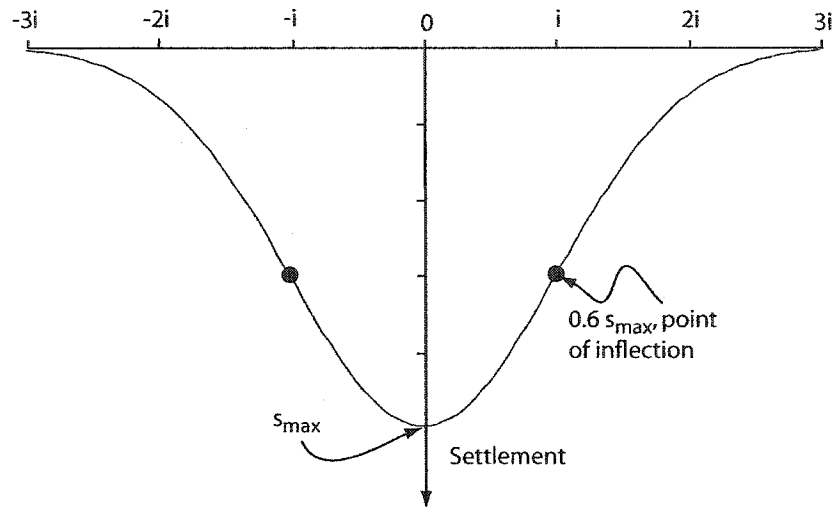


**Figure 5.1 - Gaussian curve used to describe the settlement trough**

When using this method to predict the surface settlements due to tunneling, the values of the trough width parameter and the volume loss must be selected. In a survey of English tunneling data (New 1982) showed that the relationship between the trough width parameter ( $i$ ) and the depth to the tunnel axis is approximately linear and generally independent of the construction method and tunnel diameter. They proposed the following relationship;

$$i = Kz_o \quad (5.4)$$

where  $z_o$  is the depth to the tunnel axis and  $K$  is another trough width parameter. New (1982) suggests that  $K$  is dependant upon the soil type, and a value of 0.5 can be used for clays and 0.25 for sands. Tunnels in soft clays can have considerable, and very rapid, consolidation settlements that are difficult to distinguish from immediate settlements and result in a wider settlement trough. The difference in the width of the settlement trough with soil type may also be partially due to the difference in the geometry of the failure mechanism in tunnels constructed in sand or clay, as shown in Figure 5.2.



In centrifuge tests in sand the failure tended to be in the form of a “chimney”; the failure propagated from the tunnel almost vertically to the surface. Centrifuge tests in clay showed the failure extending both upwards and outwards from the tunnel to the surface, resulting in a wider settlement trough (Mair 1997).

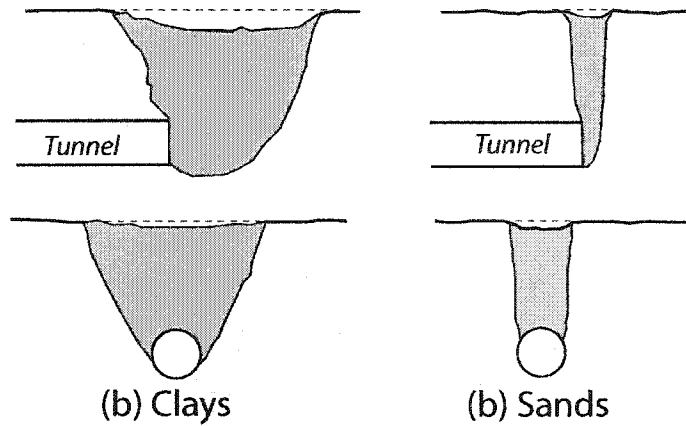


**Figure 5.2 - Failure mechanisms observed in centrifuge model tests of a tunnel in clay and sand (Mair 1997)**

However, the effect of a pre-vault in sands has been shown in theoretical analysis by (Leca 2000), and in centrifuge tests by (Skiker 1994) to limit the propagation of the failure to the surface if the pre-vault is sufficiently large, stopping the formation of a chimney (Figure 5.3). If this method is used, the settlement trough may be wider due to the limitation of plastic settlements.

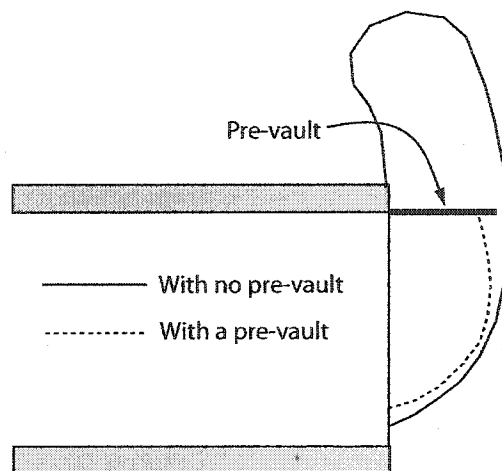


**Figure 5.3 - The effect of a pre-vault observed in centrifuge tests of a tunnel in sand**

The magnitude of the volume loss depends mainly on the type of ground and the construction method (Table 5.2). Volume losses can be higher when using earth pressure balance (EPB) or slurry shields in mixed face conditions, notably when sand or gravel overlies stiff clay.

**Table 5.2 - Range of volume loss ( $V_l$ ) for different construction techniques and soil conditions (Mair 1997).**

Construction Method	Soil	$V_l$ (%)	
		Low	High
EPB/slurry TBM	Dense fine sand	0.2	1.3
	Soft clay	1	2
	Hard sandy clay	0.03	1
	Dense sands	0.2	1
Open Face TBM	Stiff clay	1	2
NATM	London Clay	0.5	1.5

The problem with this empirical method is that the ground loss will vary with different construction techniques, tunnel design and soil properties (Ottaviani 1983). This approach provides its best results for normally consolidated clays but will tend to underestimate the magnitude of settlements in non-cohesive soils below groundwater level and overestimate settlements for non-cohesive soils above the groundwater table (New 1982). This method has limitations when applied to stratified soils and there is no prediction of the horizontal movements and the subsurface deformations (Loganathan 1998).

The inflection point (i) was determined by minimizing squared errors between the empirical fit and the observed settlements 12m north and 12m south of the centerline. The empirical analysis shows a very steep settlement trough (Figure 5.4). Using Peck's empirical fit of a Gaussian curve to the settlement profile, the trough width to the point of inflection (i) was between 4 and 7m from the tunnel axis. The  $V_l$  ranged from 0.25 to 0.46%. The volume losses observed are very low, suggesting the jet-grout technique is comparable to tunneling with EPB TBM, and better than the  $V_l$  for New Austrian Tunneling Method (NATM)(Table 5.2). The trough width parameter (K) ranges between 0.25 and 0.35. This suggests that the shape of the settlement trough is similar to that found when tunneling in sand ( $0.25 < K < 0.45$ , Mair & Taylor, 1997).

The empirical parameters for profile 1 on the Luzern axis cannot be determined because of the large heaves observed 12m south of the centerline. The empirical parameters for a Gaussian fit of the observed settlements for all 4 cross section are summarized in Table 5.3.

**Table 5.3 - Empirical parameters for a Gaussian fit to the measured settlements**

		Basel 1	Basel 2	Luzern 1	Luzern 2
i	(m)	6.1	6.5		4.1
$v_i$	(%)	0.41	0.46		0.25
overburden	(m)	14.7	15.5	11.8	13
K		0.32	0.35		0.25

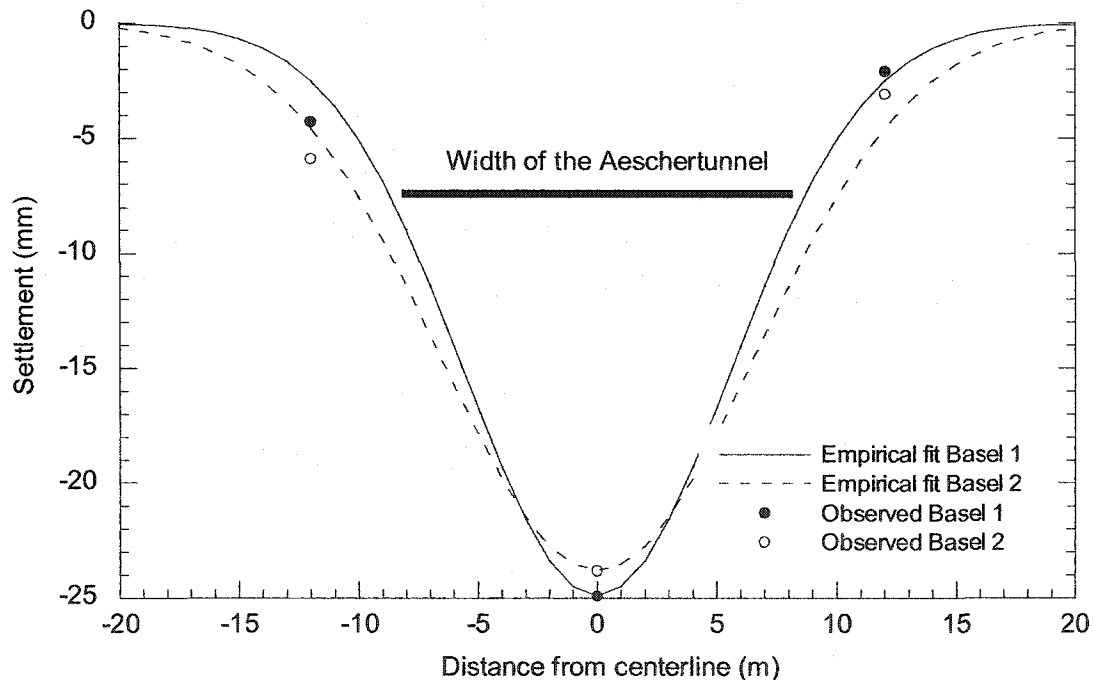


**Figure 5.4 - Observed vs. empirical fit settlements for Basel profiles 1 and 2**

The trough width inflection doesn't include any influence of the diameter of the tunnel, so it is worth noting that the trough width inflection is less than the width of the tunnel (Figure 5.4). In the next section a numerical analysis is carried out to investigate the ground deformation pattern measured at the Aeschertunnel.

### 5.3 Numerical Analysis

As shown in Figure 2.2 the displacement field due to tunneling is a 3-dimensional problem, i.e. the displacements are a function of face advance. While it is recognized that a 3-dimensional analysis may be required to examine the complete stress-strain response, several researchers have shown that 2-dimensional analysis can be used successfully to back-analyze the tunnel induced settlement trough (Rowe 1983; Gioda 1999). Although a 2-dimensional analysis is inherently inferior to modeling ground response to tunneling, the importance of workmanship and construction timing and procedure is uncertain in both 2 and 3-dimensional analysis, requiring the modeler to use some judgment in either case (Rowe 1983). The 2-dimensional analysis must employ techniques that approximate the 3-dimensional face effects. Two techniques are commonly used; (1) the stress reduction method, and (2) the stiffness reduction method.

The stress reduction method is performed by applying support pressures on the tunnel opening that are less than the original ground stresses and allowing the tunnel to converge upon these pressures before the liner is installed. When the liner is installed the remaining support pressures are removed and the liner becomes stressed. This technique is commonly used to simulate the face pressure created by an EPB or slurry shield.

In the application of the stiffness reduction method, the soil within the excavation zone is assigned a lower modulus of elasticity and the ground is allowed to deform to a new equilibrium. When the liner is installed, the final excavation is performed and the liner becomes fully stressed. When the stiffness reduction method is applied to clays it also requires lowering the Poisson's ratio, due to their incompressible nature in undrained modeling (Leca 2000).

Two dimensional methods have been used to determine the effect of construction procedures such as the time dependent hardening of shotcrete, the use of compressed air, slurry pressures and earth pressure balance TBM's, the use of grouting to improve the soil properties, and the effect of liner installation sequence on the liner loads (Swoboda 1979). Numerical models can also account for the construction phases and loading conditions associated with them. Discontinuities, soil-structure interfaces, non-homogeneous and anisotropic ground conditions can be readily modeled, limited only by the computational effort (Gioda 1999).

The numerical back analysis used a finite element program, Phase2 version 5.04, from Rocscience. Phase2 is a general 2-dimensional finite element package for the assessment of stresses and deformations, and contains special features to facilitate the modeling of tunnel excavations. The program is Windows based, and has the capability of having multiple stages; material properties and the stress states can be defined for any particular stage. This allows for the simulation of construction procedures such as staged excavation and support installation. The material models may be linear elastic, linear elastic-plastic and the failure criteria may be Mohr-Coulomb, Druker-Prager or Hoek-Brown. Additionally pore water pressures and tractions may be included

The back analysis procedure using Phase2 was to vary the model parameters starting from a set of base parameters as to get the best agreement between the observed surface settlements and the modeled settlements. The back analysis focused on the settlements from two cross sections, profile 1 and 2 of the Basel axis. The settlements from the Luzern axis were not included in the analysis in part due to the large heaving observed in Luzern profile 1, and due to the influence of the of the Basel axis being excavated first.

The Phase2 models used the heading of the tunnel cross section as shown in Figure 4.12. The base material parameters were selected from the reported values in Chapter 4, and assumed values for the surficial deposit of sand (Table 5.4). The time dependent grout material parameters were determined from the laboratory testing as described in Chapter 3. The installation timing of the grout columns was selected from the contractor's records of the grout installation times as shown in Chapter 4 (in detail in Appendix C). The grout installation included a grout support pressure (P), expressed as a percentage of overburden pressure. This pressure is assumed to include volume loss due to bleeding, shrinkage and the hydration process. The bedrock was assumed to be a rigid boundary as its Young's modulus was approximately 30 times that of the till. The ratio of horizontal to vertical stresses ( $K_0$ ) was assumed to have a base value of 0.5. While this may appear low for till, the profiles were on the outside curve of the hill and the slope wasn't horizontal in the direction of the tunnels, leading to the potential of stress release for a lower horizontal stress ratio. A typical Phase2 model is shown in Figure 5.5.

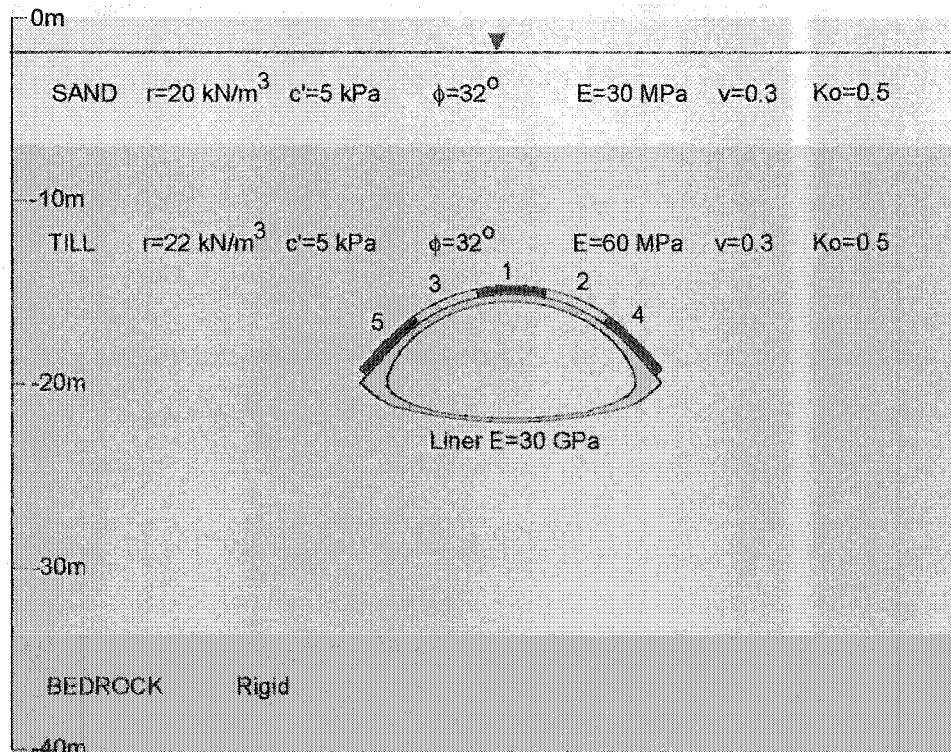


**Figure 5.5 - Typical Phase2 model showing material properties and jet-grout installation sequence**

**Table 5.4 - Base soil properties used in finite element model**

	c (kPa)	$\phi$ (degrees)	E (MPa)	v	$\rho$ (kN/m <sup>3</sup> )
Till	5	32	60	0.3	22
Sand	5	32	30	0.3	20

The liner properties were evaluated by treating the steel and the shotcrete as a homogenous isotropic composite material (Table 5.5, Appendix C). The shotcrete was assumed to fail when the mean stress was less than zero, and the steel would then take up the stress. In compression, the shotcrete has the limiting strain. Once the concrete fails it was assumed that the steel would be unable to reach its yield strain due to buckling.

**Table 5.5 - Liner properties used in finite element model**

	E (GPa)	$c_{tens}$ (MPa)	$c_{comp}$ (MPa)	$\phi_{comp}$ (deg)
Crown	29	13.5	10.2	35
Invert	26	9.2	8.6	35

The 3-dimensional nature of the tunnel displacements was accounted for by using the material softening approach. The excavation area had the stress state reinitialized to zero and its elastic modulus reduced to allow for convergence prior to the installation of the jet-grout (S1) and the liner (S2). The initial softening was applied to match the settlement profile prior to the installation of the jet-grout. These settlements were induced by the approaching tunnel

The Phase2 back analysis was performed with 4 different approaches. The first approach used an elastic model, the second approach used an elastic-plastic model, the third approach explored the effect of a reduced softening area. The fourth and the successful approach combined initial grout pressures in excess of overburden and a strain softening soil model. Before discussing the results from these models, the factors affecting the width of the settlement trough generated by the finite element method are reviewed.

### 5.3.1 Factors affecting the width of the settlement trough in a FEM

#### *General over-prediction of trough width with FEM*

A 2-dimensional analysis cannot simulate the 3-dimensional stress path the soil ahead of the advance of the tunnel experiences (Ottaviani 1983). This is important if the extrusion ahead of the tunnel becomes plastic. Even in plane strain conditions trough width may be overestimated. Stallebras (1996) performed centrifuge and finite element models of a tunnel in plane strain conditions showed that the FE model exhibited larger horizontal displacements.

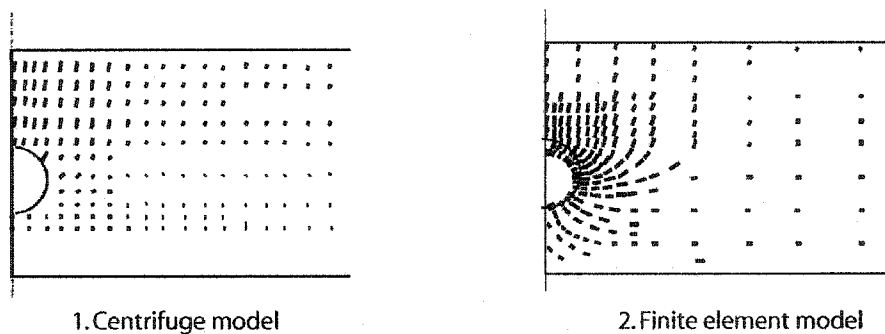


**Figure 5.6. - Trough width overestimation with FEM in sand overlying clay  
Modified from Stallebras (1996)**

The effect of the distance from the invert to a rigid underlying stratum affects the magnitude of the predicted settlement, but Rowe (1983) showed that the shape of the settlement trough in the parametric study wasn't affected significantly.

#### *Effect of soil parameters on trough width*

The material properties can also change the shape of the settlement trough. Many soils behave anisotropically (Ladd 1977). Rowe (1983) performed a parametric study and showed that for tunneling in soft clays, the settlement trough tended to narrow as the ratio of the horizontal modulus to the vertical modulus decreased. Decreasing the Poisson's ratio also decreased the width of the settlement trough. Rowe (1983) however, noted that there is a strong interdependency of the Poisson's ratio, friction angle, initial horizontal stress state, and elastic modulus. Standing (1996) reduced  $K_0$  in the vicinity of the tunnel



to account for the 3-D displacements around the tunnel face in a finite element model. This resulted in a narrower settlement trough that closely matched observed settlements.

*Strain weakening and strain localization*

Overconsolidated soils display strain localization when sheared beyond their peak strength. The limitation of FEM in predicting the trough width may be due to the soil models in the FEM being unable to effectively represent this localization of plastic strains (Sterpi 1999).

The formation of shear bands is very dependent upon the discretization of the finite element mesh (Larsson 1991). Finer meshes produce realizations of narrower shear bands (Pastor 1991; Zienkiewicz 1995), and the shear bands will tend to form in a direction parallel to the sides of the elements. The use of regular triangular elements versus quadrilateral elements can provide more directions for the bands to form and reduces some of the issues associated with strain localization and mesh dependency (Sterpi 1999).

**5.3.2 Elastic Analysis**

Preliminary modeling was carried out using an elastic model of Basel profile 2. The Young’s modulus of the till and sand ( $E_{till}$  and  $E_{sand}$ ), Poisson’s ratio of the till ( $\nu$ ), the softening parameters (S1 and S2), grout pressure (P) and the stress ratio ( $K_o$ ) were systematically changed using Powell’s method.

**Table 5.6 - Elastic model - Initial and best fit (final) model parameters**

	Initial	Final
S1	0.5	0.525
P (%)	80	70
$K_o$	0.5	0.78
$E_{sand}$ (MPa)	30	60
S2	0.5	0.6
$E_{till}$ (MPa)	60	80
$\nu_{till}$	0.3	0.39

This model used a fine mesh for the jet-grout columns. The grout pressure was applied by applying staged tractions to the boundaries of the jet-grout column. The tractions were applied upon the installation of the columns and removed when the grout had hardened upon the installation of the next set of jet-grout columns. The mesh was set as a graded type. The models had approximately 4800 elements and 2400 nodes. The elements were 3 noded triangles for all materials. The computation time was approximately 150 seconds. A total of 12 iterations were carried out, with 20 to 25 model runs per iteration.

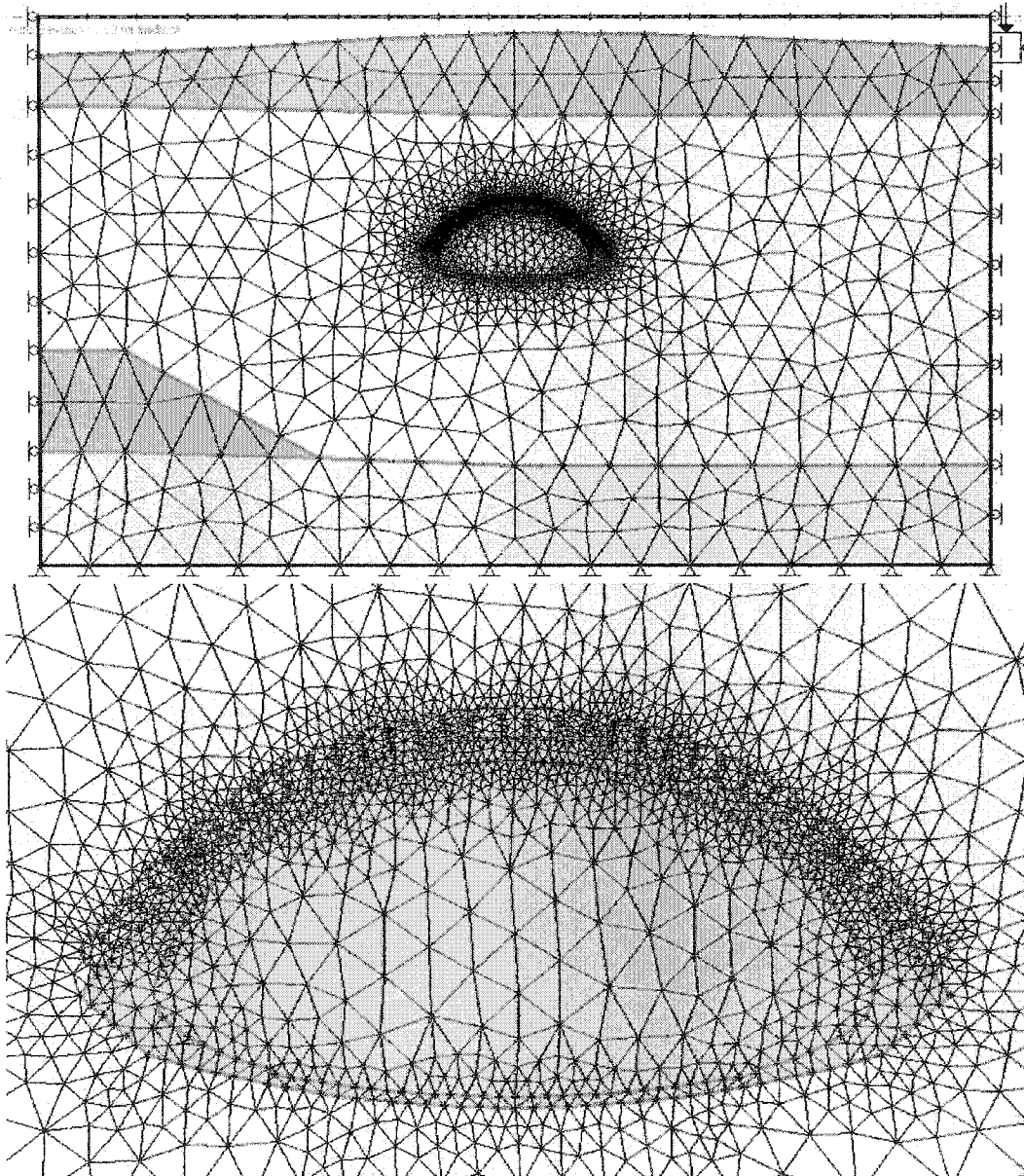


**Figure 5.7 – The finite element grade triangular mesh used in the elastic analysis**

This approach was abandoned as the results converged to settlements significantly different from the observations (Figures 5.8 & 5.9). This indicated that the mode of settlement in the model was different from the mode of settlement in the field. After the sixth iteration the reduction in error became small for successive iterations, and by the twelfth iteration the error between the modeled and observed settlements was still significant (Figure 5.9). This approach could not attain the narrow settlement trough while predicting the maximum settlement. The maximum modeled settlement was 16.9 mm above the centerline.

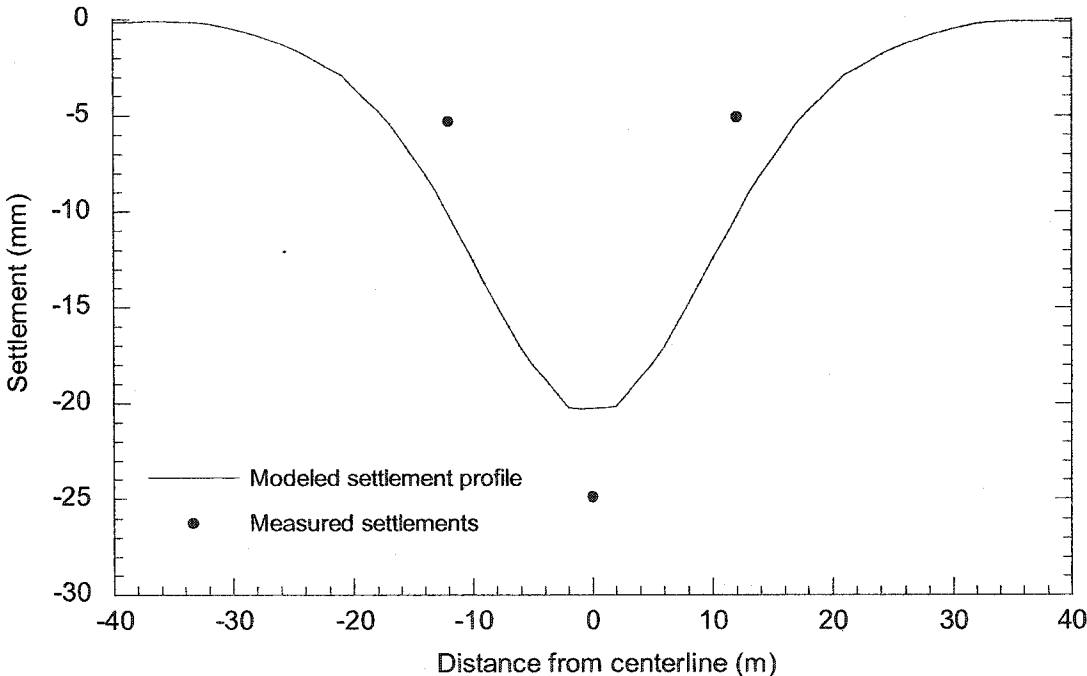
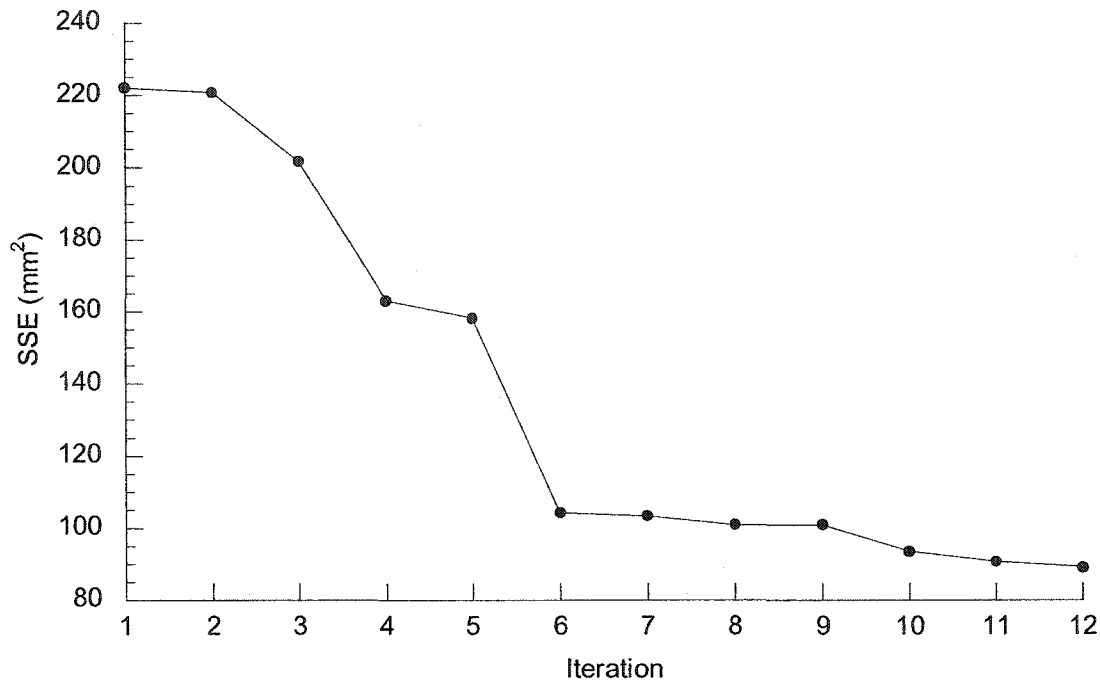


Figure 5.8 - Modeled vs. measured settlements for Basel profile 2, elastic model



**Figure 5.9 - Elastic model convergence**

### **5.3.3 Elastic Plastic Analysis**

The time involved in running a Phase2 analysis is related to the number of elements in the model. To reduce the computation time the number of elements was reduced by representing the jet-grout columns having a square cross section. Each grout column was modeled using two triangular elements. The cross sectional area of a 600mm diameter jet-grout column was used to determine the dimensions of the trapezoidal equivalent having the same centers as the round jet-grout columns. The elastic plastic model was modeled after Basel profile 2.

The elastic-plastic model used an elastic-perfectly plastic soil model with the cohesion set to zero. Elastic plastic modeling was carried out by varying the Young's modulus of the till and sand ( $E_{till}$  and  $E_{sand}$ ), Poisson's ratio of the till ( $\nu$ ), the softening parameters ( $S1$  and  $S2$ ), grout pressure ( $P$ ) the stress ratio ( $K_0$ ) and the friction angle of the till ( $\phi_{till}$ ). The parameters were systematically changed using Powell's method.

**Table 5.7 - Elastic-plastic model - Initial and final (best fit) model parameters**

	Initial	Final
$E_{\text{till}}$ (MPa)	80	100
$\nu_{\text{till}}$	0.3	0.4
$E_{\text{sand}}$ (MPa)	60	80
$K_o$	0.5	0.6
S1	0.5	0.5
S2	0.5	0.5
P (%)	80	80
$\phi_{\text{till}}$ (deg)	32	32

The mesh was set in Phase2 as a graded type. The grout pressures were modeled in the same manner as the elastic modeling. The models had approximately 1870 elements and 970 nodes. The elements were 3 noded triangles for all materials. In order to further reduce the computation time the numerical convergence was set to 0.01. The computation time was approximately 10 minutes. A total of 5 iterations were carried out, with approximately 25 to 30 model runs per iteration.

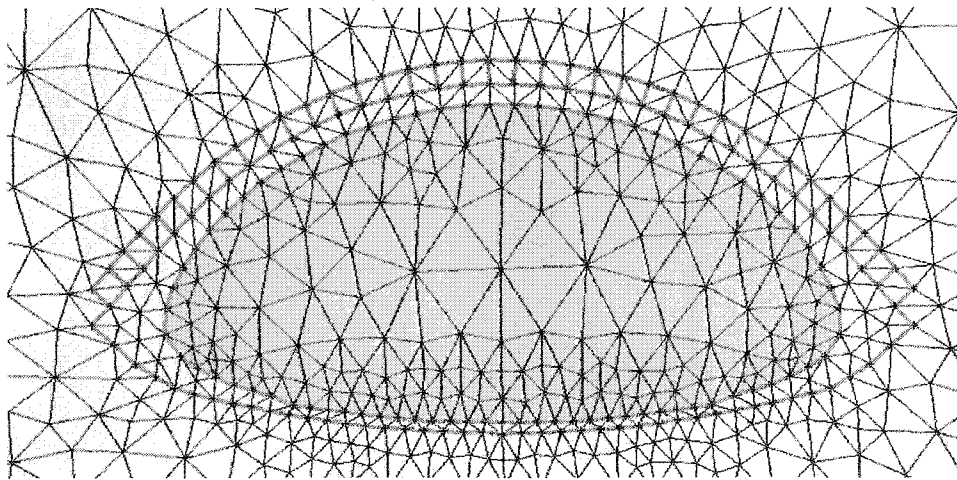


**Figure 5.10 - Mesh used in the elastic-plastic analysis**

The maximum settlement was 17.0mm above the centerline and a trough inflection point of 9.5m. This indicated that the model was still unable to capture the shape of the settlement trough. Figure 5.11 illustrates the yielded zone in percent yielded elements. There is some limited yielding at the base of the jet-grout arch and at the 4 locations where 5 sets of jet-grouting meet. The yielded zone below the invert is larger, but did not contribute significantly to a narrower settlement trough (Figure 5.12).

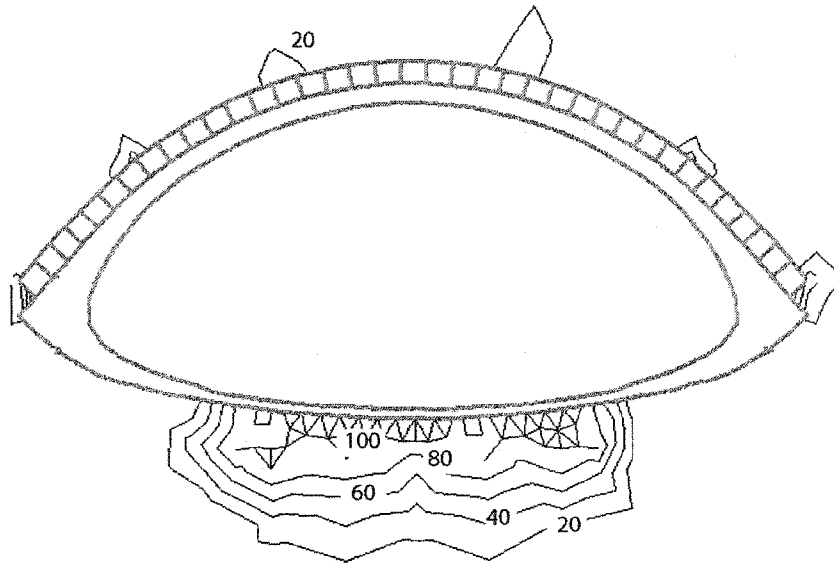


**Figure 5.11 - Trial 2 - Yielded elements in elastic-plastic model**

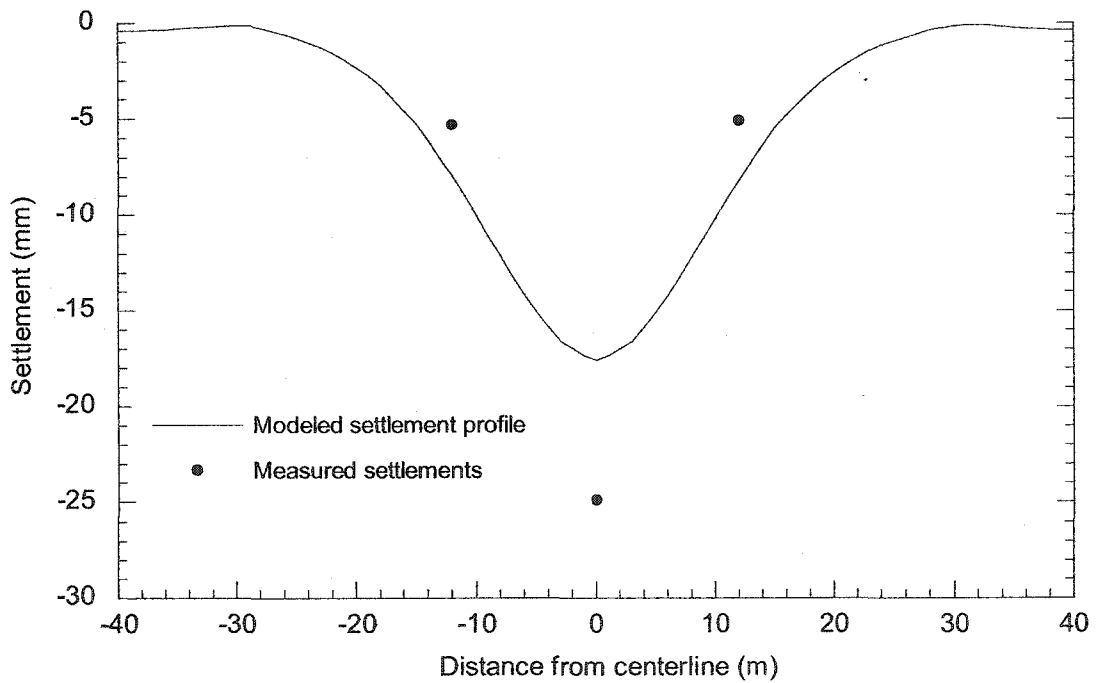


**Figure 5.12 - Modeled vs. measured settlements for Basel profile 2, elastic-plastic model**

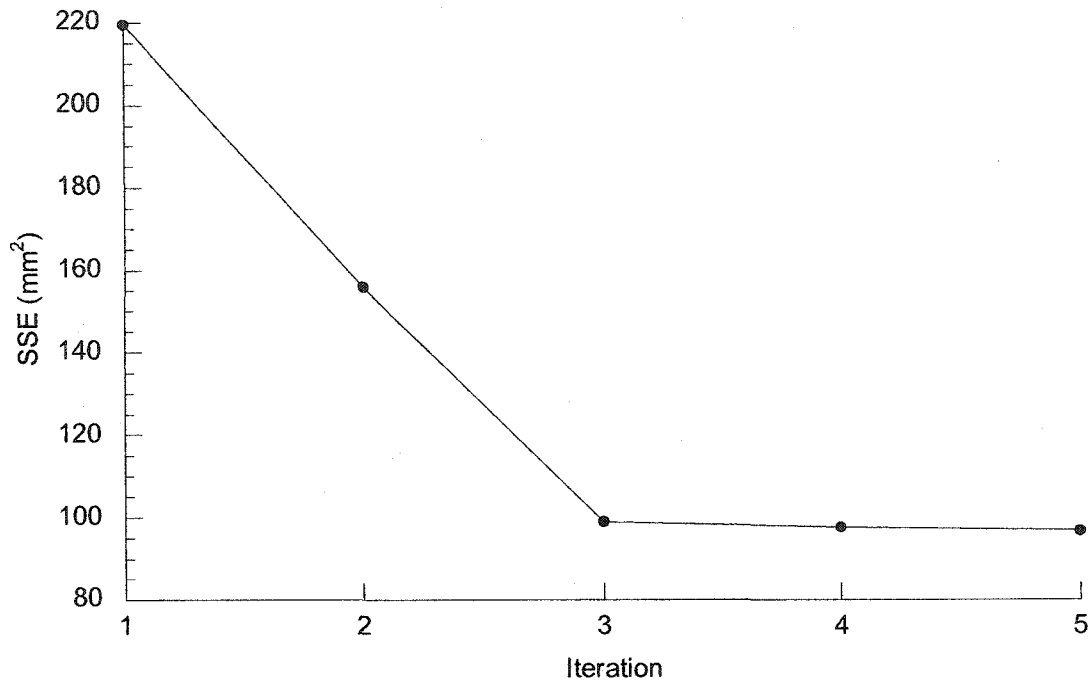


**Figure 5.13 - Elastic plastic model convergence**

#### **5.3.4 Effect of reduction in softening area on trough width**

The modeling approach changed from trying to match the observed settlements to trying to capture a settlement mode that would give a much narrower settlement trough. In an attempt to attain a narrower settlement profile in Phase2 the softening area was reduced. As stated previously the softening of the excavation area is commonly used in 2-dimensional modeling to simulate the tunnel face advance and timing of the installation of the support, however there are no guidelines as to the amount of softening or the area of the tunnel face that should be softened, particularly for large span tunnels. The rationalization for the use of a reduced softening area to achieve a narrower settlement trough is that the jet-grout vault would reduce horizontal displacements beyond the jet-grout vault, resulting in most of the 3-dimensional displacements occurring in the center of the excavation.

The use of a softening area less than the total area of the face was investigated using the initial material and model parameters as reported in Table 5.7. Four models with softening areas of 100%, 82%, 55% and 33% of the excavation area were run. The finite element models for this series of analysis were otherwise the same as the elastic plastic model. There was no further calibration of the parameters in these models as this was solely an investigation into the effect of the reduction in the softening area on the trough width.

**Table 5.8 - Effect of reduced softening area on the trough width parameter (i)**

Softening Area (% of excavation)	Trough width (i) (m)
100	10.2
82	10.1
55	9.8
33	9.6

Reduced softening areas resulted in a slightly narrower settlement profile (Figure 5.14), and correspondingly the settlement trough didn't have significant reduction of the inflection point (Table 5.8). Because this was an investigation in the effect of the softening area on the trough width and not the magnitude of the settlements, Figure 5.14 illustrates the settlements normalized to the maximum settlement



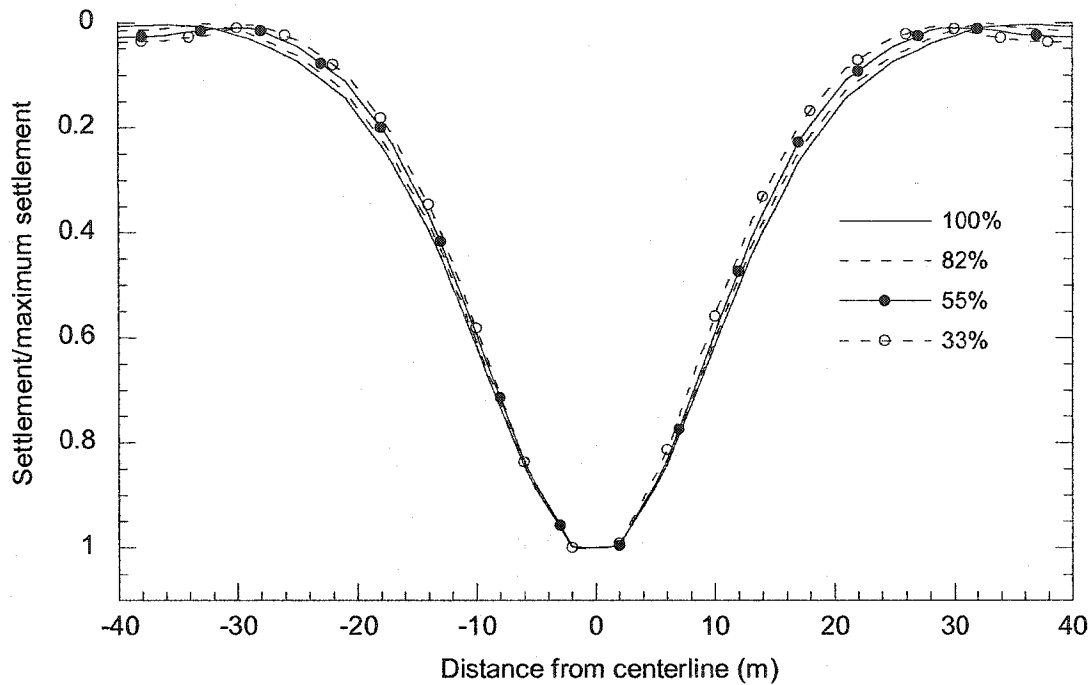


**Figure 5.14 - Effect of a reduced softening area, expressed as a percentage of the tunnel cross sectional area, on the trough width**

### **5.3.5 Elevated grout pressures in excess of overburden**

As shown in Figures 4.21 to 4.24 the jet-grouting process resulted in considerable heave, indicating that the grout pressures were in excess of overburden. These grout pressures are due to a portion of the injection pressures of 40 MPa acting on the soil over the extent of the jet-grout column. The observation of grout coming to the surface through the inclinometer casing (Figure 5.15) is a further indication that the grout pressures were in excess of overburden, additionally the grout pressures were sufficient to blow out wooden plugs in adjacent jet-grout columns. This modeling approach used grout pressures that varied from 200% of overburden (approximately 0.7 MPa) upon installation of the jet-grout, to 90% of overburden (approximately 0.3 MPa), when the grout had set.

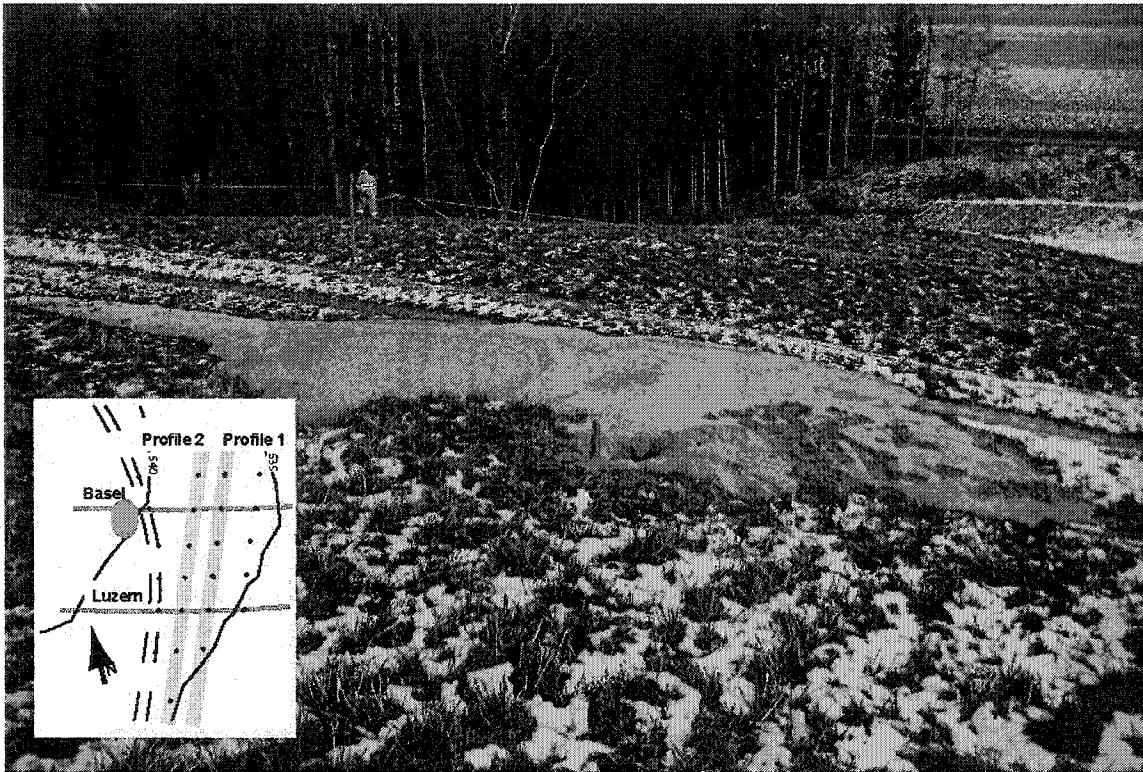


**Figure 5.15 - Evidence of grout over pressurization near profiles 1 and 2**

This model used an elastic-plastic soil model for the till, with the same finite element mesh as used in the elastic-plastic analysis (Section 5.3.3). To reduce time in setting up the models for the initial iterations, the grout pressures were modeled by altering the grout material properties. The installation of the grout was modeled by changing the material within the grouted zone to grout from till. The grout pressures were modeled with a high initial value, to represent the high pressures observed during the jet-grouting process. The residual pressures were applied when the grout had hardened, and the material properties were changed to the hardened values. The procedure is summarized below.

### *Step 1 - Unhardened jet-grout installation*

Replace the till in the model with unhardened jet-grout. This results in the initialization of the stress state of the grout. The jet-grout has the initial element loading state set to hydrostatic ( $K_0=1$ ). In order to simulate pressures in excess of overburden, in the field stress properties menu, the unit weight of the overburden of the unhardened jet-grout is assigned a value greater than the unit weight of the overlying till. For example if the till has a unit weight of  $21\text{kN/m}^3$ , assigning the unit weight of the overburden for the unhardened jet-grout to  $42\text{kN/m}^3$  results in grout pressures equal to 200% of overburden.

The material properties of the unhardened jet-grout are assigned so that its Poisson's ratio and Young's modulus are reduced to 1/1000 of the hardened values. This makes the grout act like a pressurized fluid upon the installation; it allows the jet-grouted area to change in volume and still maintain hydrostatic pressures in the fluid state.

### *Step 2 - Hardened jet-grout installation*

In the next stage the hardened jet-grout is installed. The pressures are reduced to simulate the effect of the loss of volume due to loss of bleed water, drying shrinkage and hydration. To simulate reduced pressures this material has the unit weight of overburden adjusted as described earlier. The installation of the hardened material results in the initialization of the stress state of the grout. The material properties are changed to the hardened properties, with staged material properties to simulate the hardening of the jet-grout.

The model used 14 stages to simulate the effects of construction procedure and timing (Table 5.9). The installation of the jet-grout columns occurred over the period of 5 shifts, grouting the crown of the tunnel first and then alternating from side to side. An installation time of 5 hours per set, and a setting time of 19 hours were used in the modeling to determine the grout material parameters.

**Table 5.9 - Model staging with high grout pressures**

Stage	Jet-grout Installation	Grout Pressure	Excavation Area
1			
2			Soften (S1)
3	Set 1, Columns 16-22	High	
4		Low	
5	Set 2, Columns 23-29	High	
6		Low	
7	Set 3, Columns 9-15	High	
8		Low	
9	Set 4, Columns 30-37	High	
10		Low	
11	Set 5, Columns 1-8	High	
12		Low	
13			Soften (S2)
14			Excavate, install liner

The model was run with the model parameters given in Table 5.10. The agreement between the measured and modeled settlements is an improvement over the previous models, but the model was still unable to capture the narrow settlement trough (Figure 5.16).

**Table 5.10 - Parameters for elastic plastic model with elevated grout pressures**

Parameter	Value
$E_{\text{till}}$ (MPa)	70
$\phi_{\text{till}}$ (deg)	40
$\nu_{\text{till}}$	0.2
$E_{\text{sand}}$ (MPa)	35
$\phi_{\text{sand}}$ (deg)	33
$P_{\text{peak}}$ (%)	200
$P_{\text{residual}}$ (%)	100
$K_o$	0.5
S1	0.525
S2	0.95

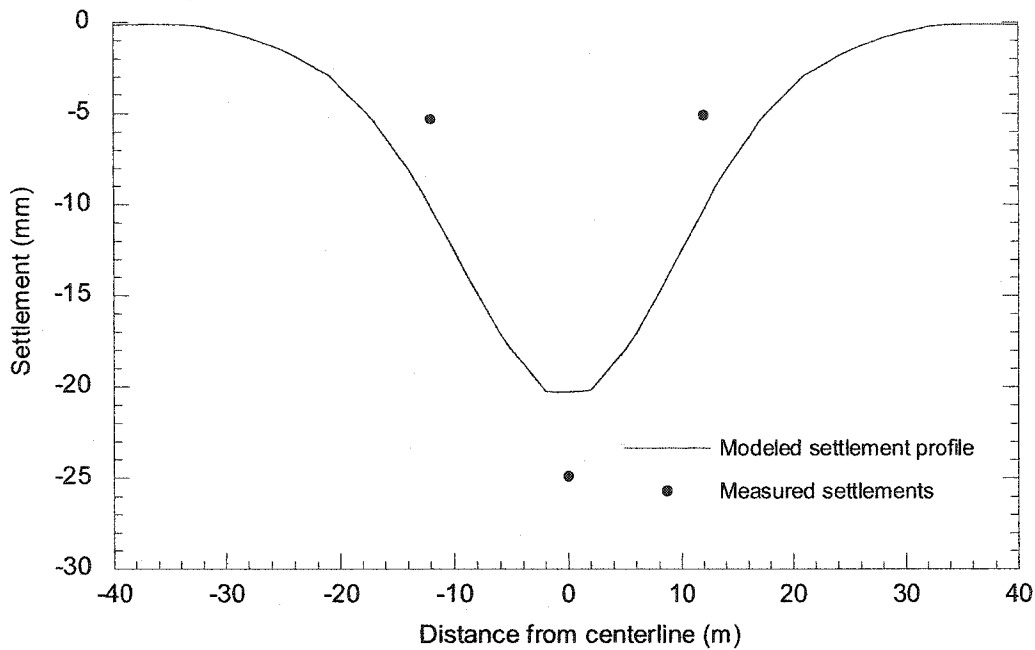


**Figure 5.16 - Model results using grout pressures in excess of overburden**

### ***5.3.6 Elevated grout pressures & strain softening soil model***

The Aeschertunnel was constructed in a glacial till. Glacial till is an overconsolidated soil and usually displays a strain weakening behavior. For example (Bishop 1965) showed using undisturbed samples of London Clay that the peak frictional resistance of  $30^\circ$  decreased to a residual frictional resistance of  $16^\circ$  at approximately 4% axial strain in triaxial testing, while the peak strength was recorded at about 2% strain. The vertical settlement of the tunnel roof after the jet-grouting and the installation of the shotcrete liner was approximately 15mm. If the convergence after the installation of the liner represents 15 to 30% of the total convergence, this suggests a strain tangential to the excavation boundary of 50/5000 (1%) to 100/5000 (2%). This is assuming the same amount of convergence toward the tunnel axis from all directions and a tunnel radius defined by;

$$r = \sqrt{\frac{A_t}{2\pi}} \quad (5.5)$$

where  $A_t$  is the excavation area and  $r$  is the tunnel radius.

As explained in Section 5.3.1, modeling localization of plastic strains requires a fine uniform mesh to reduce mesh dependency. To achieve the formation of yield bands, a fine mapped rectangular mesh made up of 3 noded triangular elements was introduced above the tunnel crown (Figure 5.17). This region contained 4800 elements for the initial iterations and was refined further for the final iteration with 17750 elements.

The back-analysis procedure applied to the strain weakening approach no longer used Powell's method due the time involved by the user in a sequential search. The search method changed to a multivariate grid search. This allowed multiple models to be run overnight. The multivariate grid search tested 3 to 5 variables at two points per variable, resulting in 8 to 32 model runs per iteration. The best result of each iteration was evaluated by the errors between the observations and the model and the trough width. No formal weighting was applied to the trough width parameter and the settlement error in the selection of the best model. The values of the variables used in the iterations were based upon experience gained in the previous iterations.

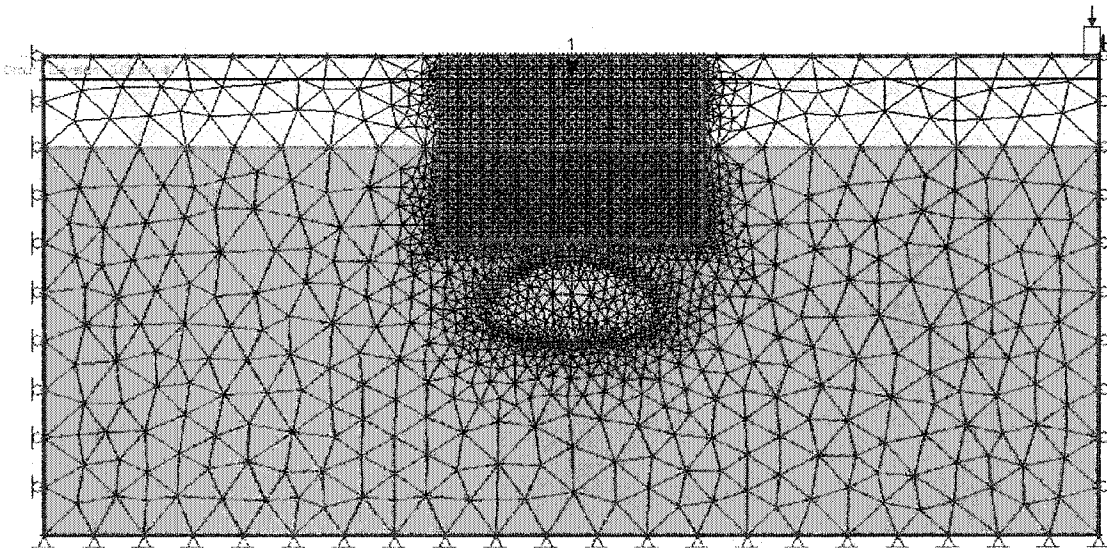


**Figure 5.17 - Finite element mesh for strain softening model with high grout pressures**

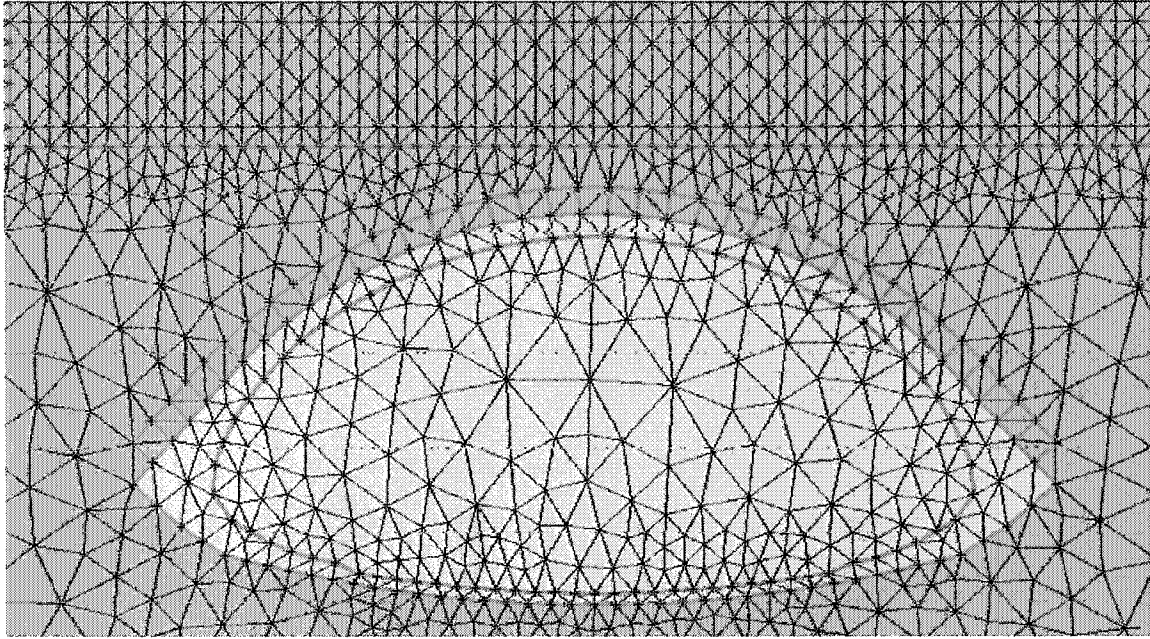


**Figure 5.18 - Finite element mesh for strain softening model with high grout pressures – Detail of excavation area**

The previous trials determined that the softening parameter S1 should reduce the Young's modulus in the excavation area to 52.5% of initial when a modulus of 60 MPa was used for the till. The first iteration varied 5 parameters, peak pressure ( $P_p$ ), residual pressure ( $P_r$ ), Poisson's ratio, till friction angle and the second softening (S2), at two points per parameter for 32 model runs per iteration.

**Table 5.11 - Strain softening model parameters - iteration 1**

	$P_r$ (%)	$P_p$ (%)	$\phi$ (degree)	$\nu$	S2 (%)
High	100	175	40/30	0.3	75
Low	90	150	36/27	0.2	60
Best	90	175	36/27	0.2	60

The first iteration gave a best fit with a sum of squared error of  $26.5\text{mm}^2$  between the modeled settlements and the measured settlements at Basel profile 2. The maximum settlement was 19.4mm above the tunnel axis with a trough width of 8.61m. This indicated that the modeled settlements 12m from the centerline were too large. In order to reduce the settlement in the model 12m from the tunnel axis, the softening parameter S2 was given a lower bound of 60% so that the search would investigate models with

limited settlement off the centerline. The pressures were also searched in higher values, as these were critical causing the formation of shear bands above the tunnel crown resulting in a narrower settlement trough. The Poisson's ratio and the friction angle of the till were also further investigated.

**Table 5.12 - Strain softening model parameters - iteration 2**

	Pr (%)	Pp (%)	$\phi$ (degree)	$\nu$	S2 (%)
High	100	200	40/30	0.25	75
Low	90	175	36/27	0.2	60
Best	100	200	36/27	0.2	75

The second iteration resulted in a best fit with error of  $10.2\text{mm}^2$  when compared with Basel profile 2. The maximum settlement was 21mm and the trough width parameter 7.82m. The best fit for the second model resulted from higher grout pressures and a higher value of S2. The Poisson's ratio and friction angle remained at their lower values. Because of the dependence of the extent of the propagation of the shear band upon the friction angle and the element size, the friction angle was investigated for the third iteration with the finer mesh.

**Table 5.13 - Strain softening model parameters - iteration 3**

	$\phi$ (degree)	E (MPa)	S2 (%)
High	40/30	70	95
Low	36/27	60	75
Best	40/30	70	95

The final iteration yielded errors of  $15.4\text{mm}^2$  for Basel profile 1 and  $3.2\text{mm}^2$  for Basel profile 2. The maximum settlement was 24.2mm with a trough width parameter of 6.75m. The best fit had the reduced degree of softening and the higher friction angle. The effect of the smaller element size in the third iteration resulted in the shear band being able to propagate towards the surface even with the higher peak and residual friction angles.



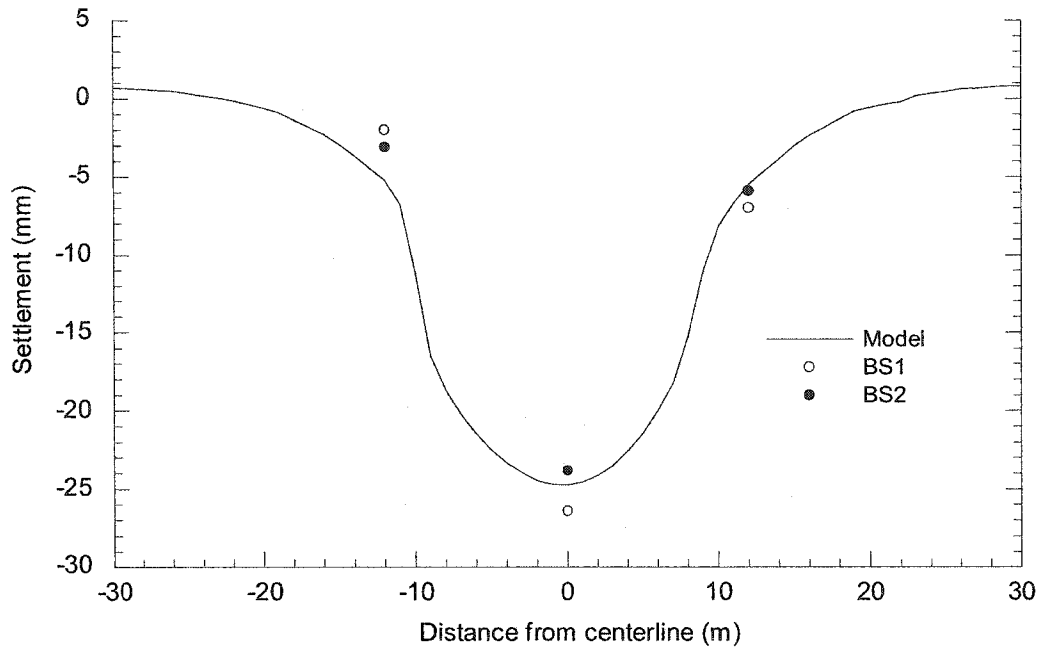


**Figure 5.19 - Strain softening modeled settlement profile using the best fit parameters**

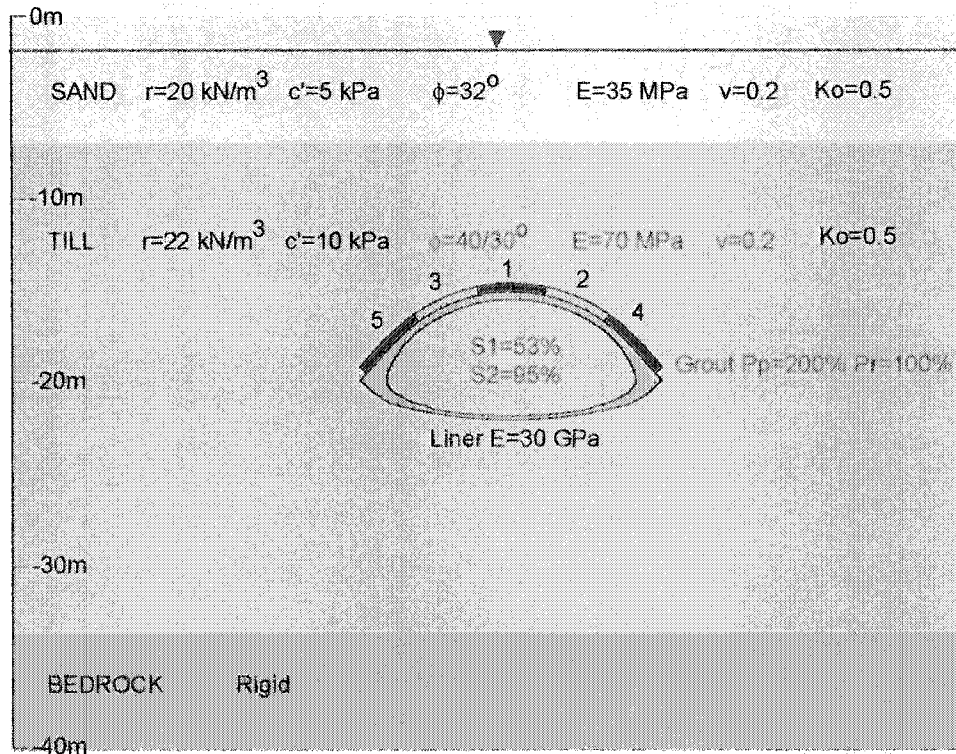


**Figure 5.20 - Strain softening model profile showing modeling parameters and jet-grout installation sequence for the best fit (iteration 3). The varied parameters are shown in red type.**

### Settlement Development

The jet-grouting process yielded centerline settlements of 5mm and heaving of 5mm. Heaving during each jet-grout stages ranged from 1.5 to 3.5mm of maintained heave (Figures 5.22-5.25). During the installation of the first set of columns at the crown (columns 16 to 22) the heave is approximately symmetric, with a maximum of 2mm. The installation of the second and third sets of columns (23 to 29, 9 to 15)) resulted in maintained heaving of approximately 3.5mm, located above the installation of the jet-grout 12m from the centerline. The installation of the fourth and fifth sets (30 to 37, 1 to 8) resulted in additional heaved of approximately 1.5mm, again this heave was above the set being installed 12m from the centerline. The use of a lower residual jet-grout pressure caused the maintained heaving to be less than the peak observed during the jet-grout column installation.

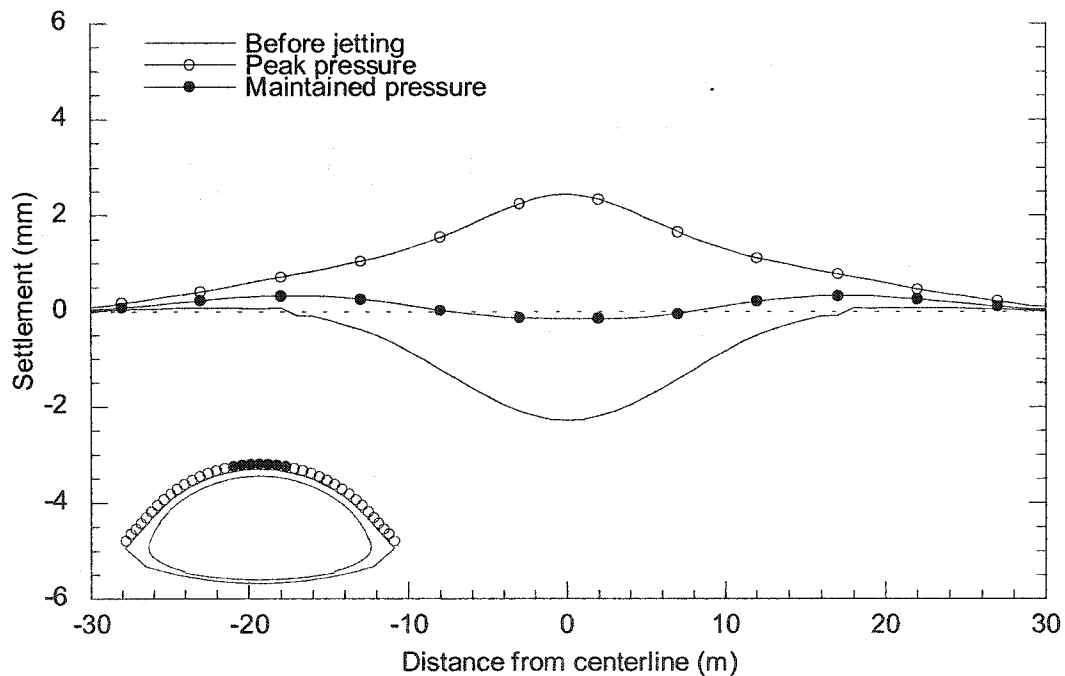


Figure 5.21 - Modeled deformation during installation of jet-grout columns 16 – 22

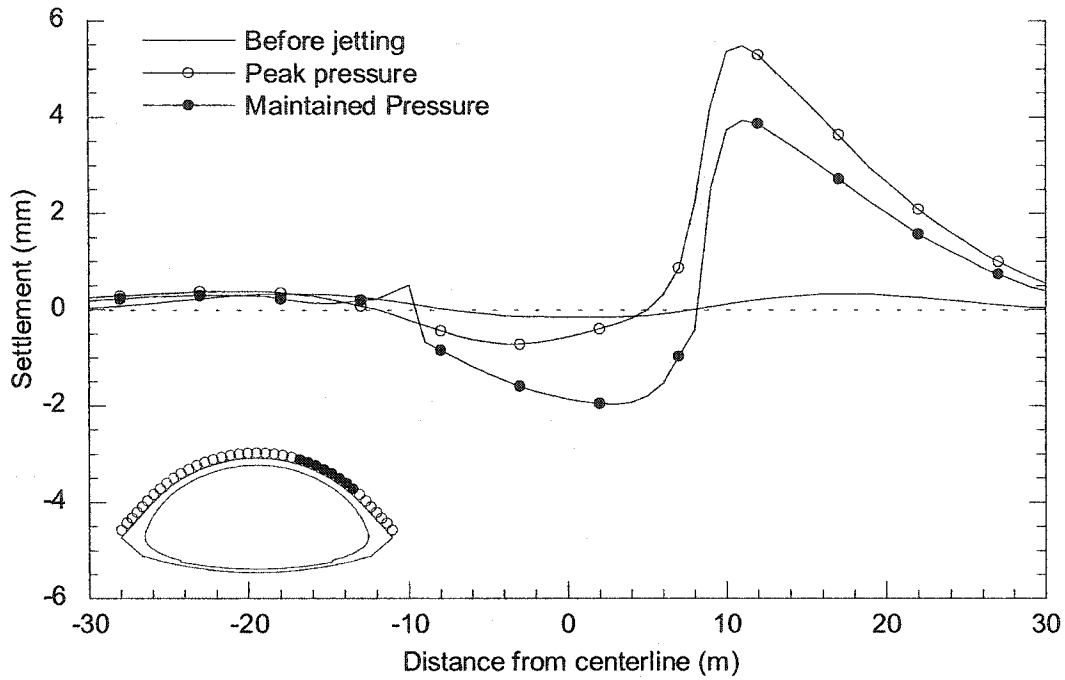


Figure 5.22 - Modeled deformation during installation of jet-grout columns 23 – 29

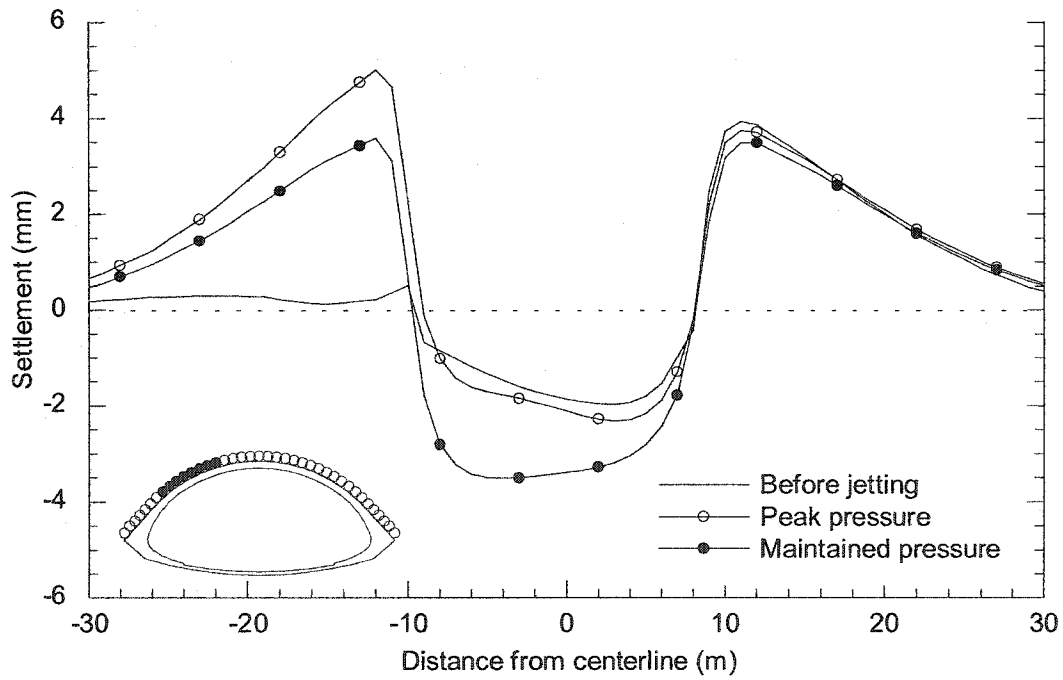


Figure 5.23 - Modeled deformation during installation of jet-grout columns 9-15

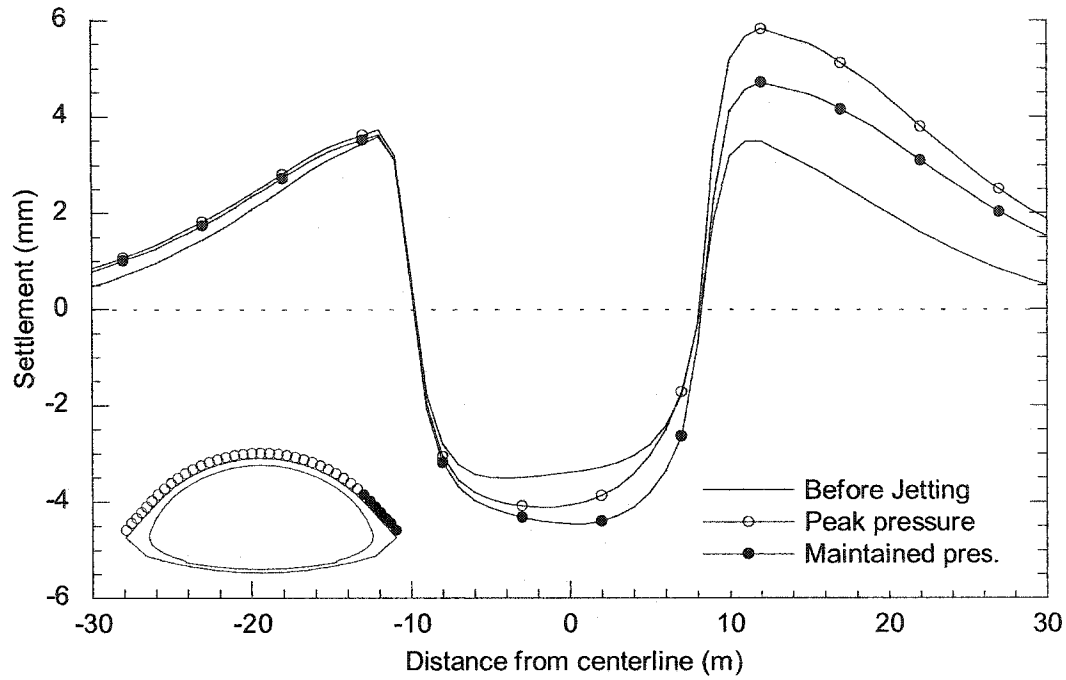


Figure 5.24 - Modeled deformation during installation of jet-grout columns 30 - 37

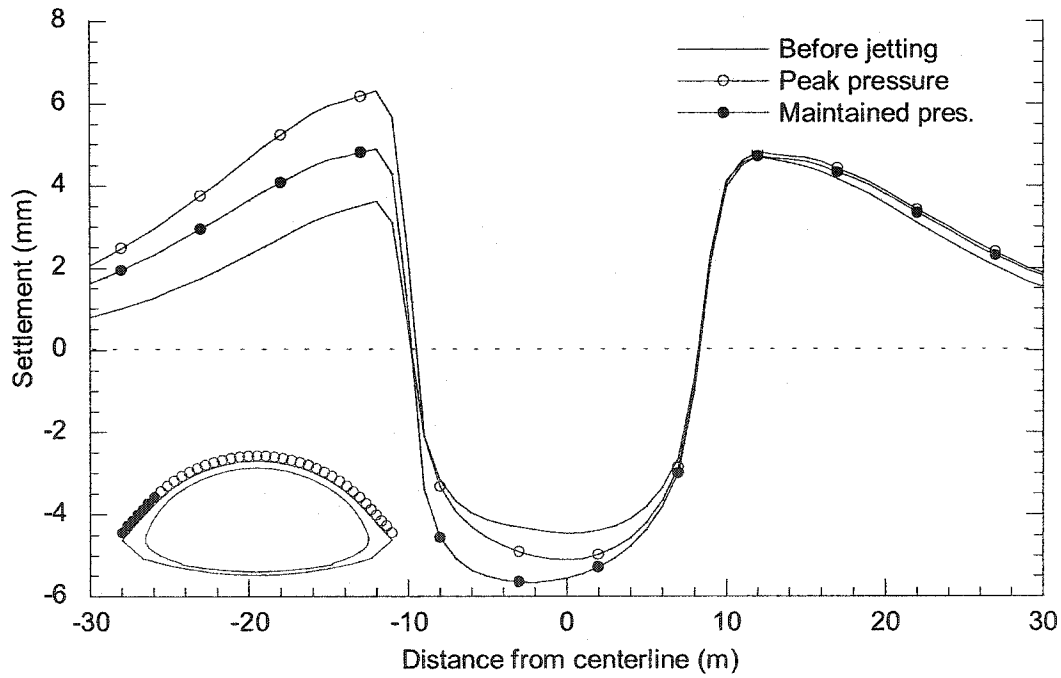
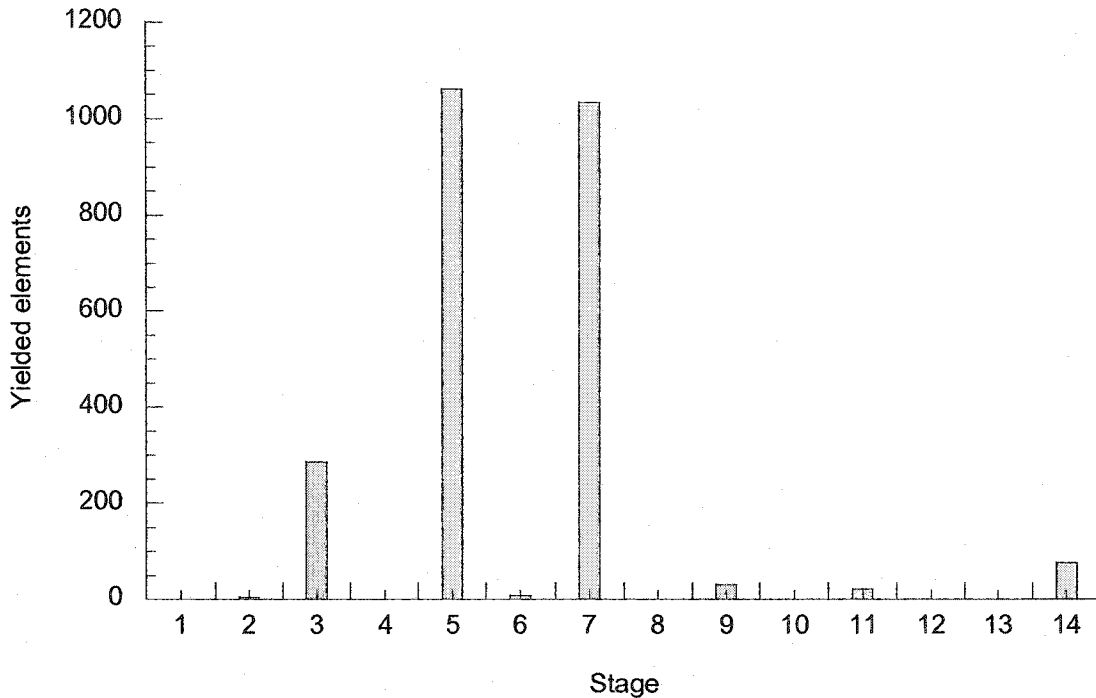


Figure 5.25 - Modeled deformation during installation of jet-grout columns 1 - 8

### *Yield development*

The majority of element yielding occurs during the installation of the jet-grout in stages 3, 5, and 7; during the application of the high grout pressure as shown in Figure 5.26. The excavation and installation of the liner only resulted in limited yielding of the till below the invert. There was no yielding of the jet-grout columns or the liner.



**Figure 5.26 - Yield development by stage (additional elements)**

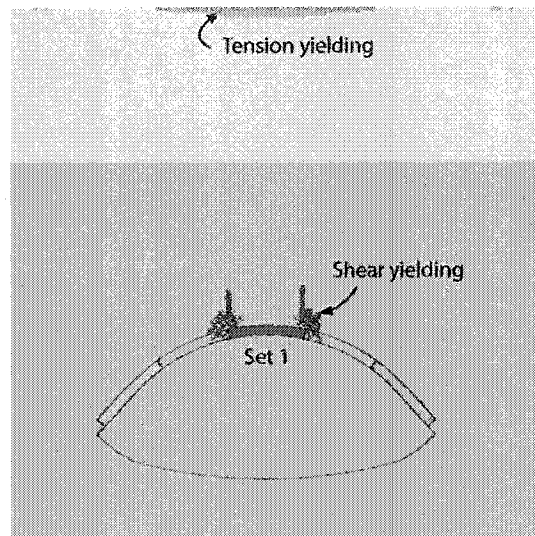
During the application of high grout pressures during the installation of the first set of jet-grout columns in stage 3, plastic straining developed at the shoulders of the jet-grout columns 16-22, adjacent where columns 15 and 23 were be installed. The reduction of the grout pressures didn't contribute to further yielding in stage 4. The installation of the second set of columns in stage 5 resulted in extensive element yielding. This zone formed in a linear manner extending from the interface of the first set and second sets of jet-grout, extending upwards at an angle of  $28^\circ$  from vertical to within 2.3m below the surface. This shear band was 1 to 2 elements thick. The installation of the third set in stage 7 resulted in extensive yielding similar to the yielding in stage 5. The shear band

developed at an angle  $33^\circ$  from vertical, again passing into the surficial layer to 1.8m below the surface. The installation of the fourth and fifth sets of jet-grout in stages 9 and 11 resulted in yielding at the bases of the jet-grout arch and the interfaces of adjacent sets of jet-grout columns.

**Table 5.14 - Stages used in the Phase2 strain weakening model and the associated yielding due to the jet-grout process.**

**Stage 3**

- Installation of the first set of grout columns 16-22 (set 1).
- heaving results in tension failure of soil at the surface.
- Shear bands begin to form above the jet-grouted zone, some tensile failure is observed in the immediate vicinity of columns 16 & 22.



**Stage 5**

- Installation of jet-grout columns 23-29 (set 2).
- The shear band propagates upwards from the interface of grout set 1 and grout set 2.
- The soil to the right of the shear band moves upwards, in the direction of the shear band.
- The soil to the left of the shear band moves down, resulting in further tensile failure near the surface.

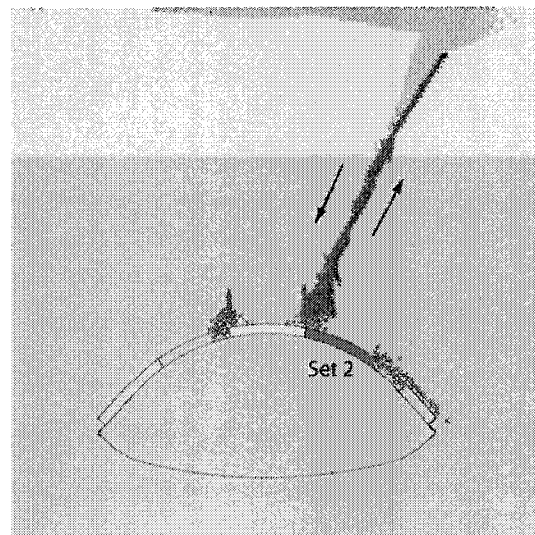
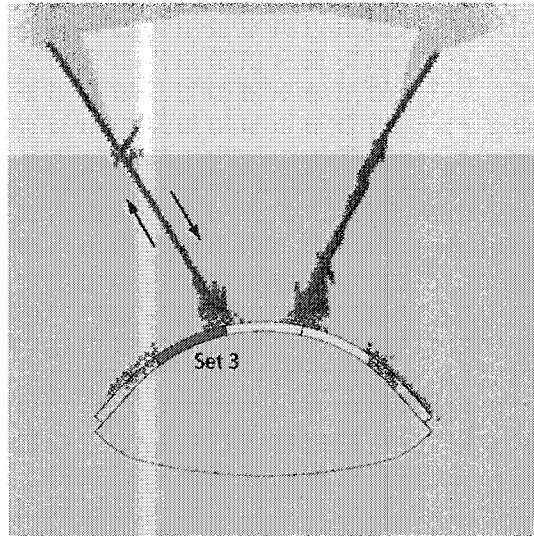


**Table 5.14 continued**

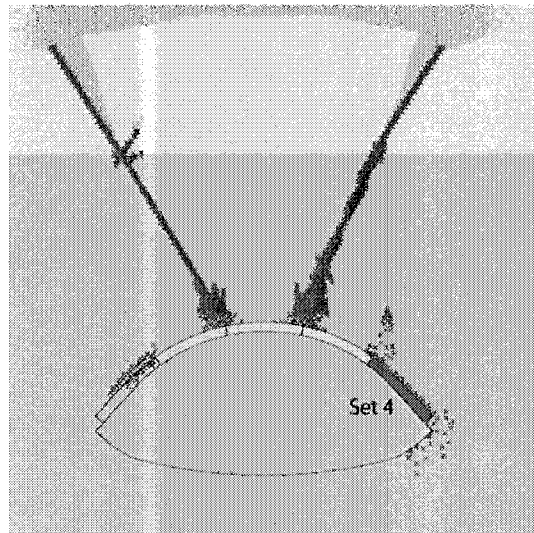
**Stage 7**

- Installation of jet-grout columns 9-15 (set 3).
- The second shear band propagates upwards from the interface of grout set 1 and grout set 3.
- The soil to the left of the second shear band moves upwards, in the direction of the shear band.
- The soil to the right of the shear band moves down, resulting in further tensile failure near the surface.



**Stage 9**

- Installation of jet-grout columns 30-37 (set 4).
- There is no further propagation of the two shear bands, and no further tensile failure at the surface.
- The soil on both sides of grout set 4 shows some localized yielding.



**Stage 11**

- Installation of jet-grout columns 1-8 (set 5).
- There is no further propagation of the two shear bands, and no further tensile failure at the surface.
- The soil on both sides of grout set 5 shows some localized yielding.

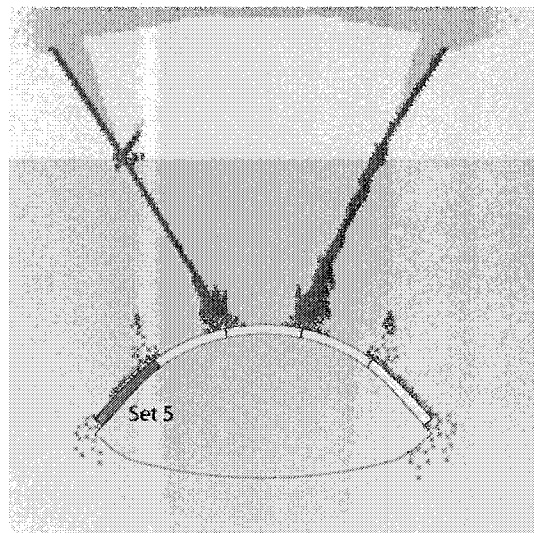


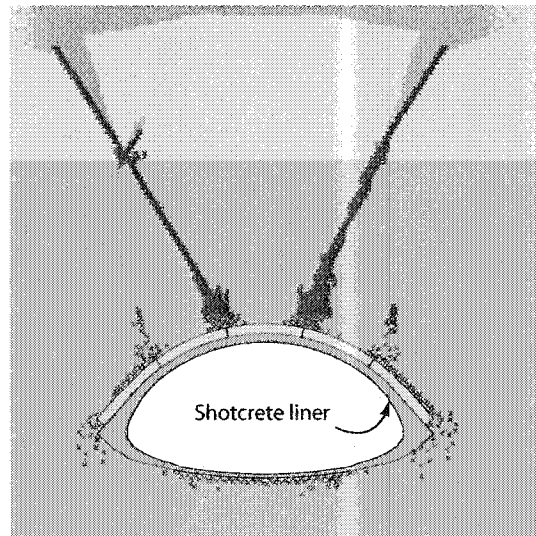
## Table 5.14 continued

### Stage 14

-Second softening of the excavation area, followed by simultaneous excavation and installation of the shotcrete liner.

-There is no further propagation of the two shear bands, and no further tensile failure at the surface.

-The soil below the invert has limited yielding, both in shear and in tension.



### 5.4 Evaluation of the liner loads

Once the jet-grout columns are installed and hardened they provide a stiff umbrella for excavating the tunnel. Often the design of the primary shotcrete liner ignores the loads that may be carried by the jet-grout columns. To estimate the load carried by the jet-grout columns, two Phase2 analyses were carried out. In the first analysis the material within the jet-grouted zone was changed to till in the stage prior to the second softening of the excavation area, and the other left the jet-grout in place. The rationale for changing the jet-grout area to till is that the model will still have the same stress and deformation history as before, so the portion of the excavation load taken by the jet-grout vault and the change in the settlement can be quantified. The jet-grout in the second model was installed in the same manner as before.

In order to describe the liner loads in terms of bending moments and normal forces the shotcrete liner was replaced with Timoshenko beam elements. The shotcrete liner, as shown in earlier models, was removed and replaced with till. The Timoshenko beam elements were placed on the inside edge of where the shotcrete liner previously was, and had a thickness of 400mm and a Young's modulus of 30 GPa.



The removal of the jet-grout vault resulted in a very small increase in the settlement. The maximum settlement increased by 0.4mm from 30.0mm to 30.4. The settlements are not the same as in Section 5.3.6 because the liner isn't the same thickness at the springline as in the strain weakening model with grout pressures greater than overburden.

There is an increase in the axial force in the liner in the portion of the liner above the springline when the jet grout arch is removed as shown in Figure 5.27. The normal force is a minimum in the invert, 15m from the tunnel crown. The two spikes that appear in Figures 5.27 to 5.29 are at the springline where the actual liner is the thickest. This is the area of the jet grout arch. The bending moments and the shear forces in the liner are not significantly affected by the presence of the jet-grout arch (Figures 5.28 and 5.29).

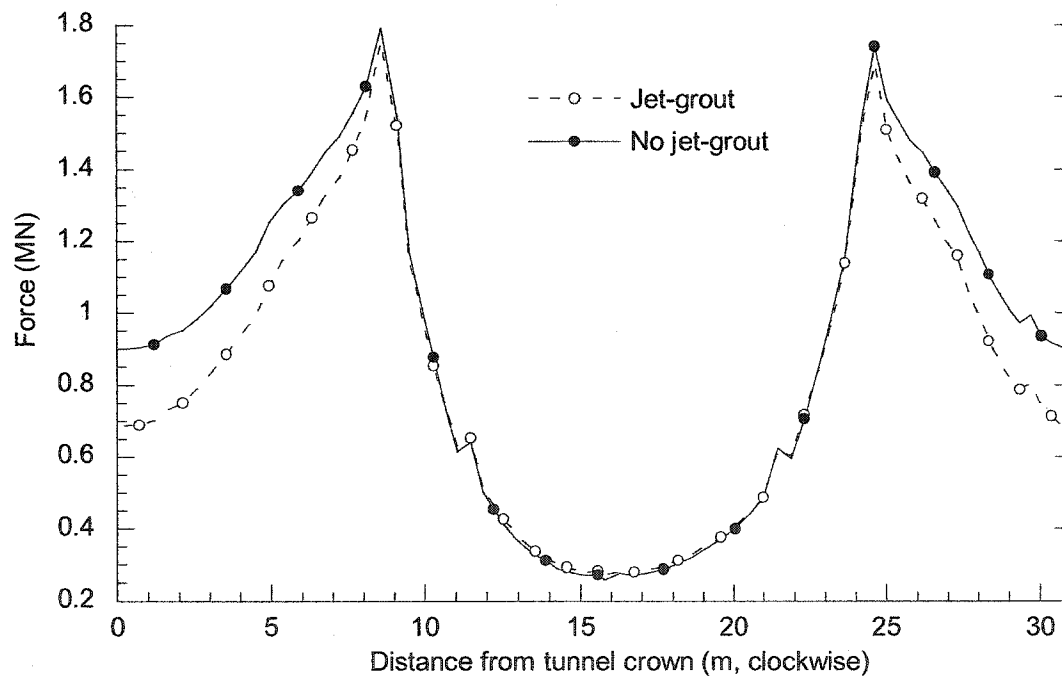


**Figure 5.27 - Modeled axial force in the shotcrete liner with and without the presence of the jet-grout arch**

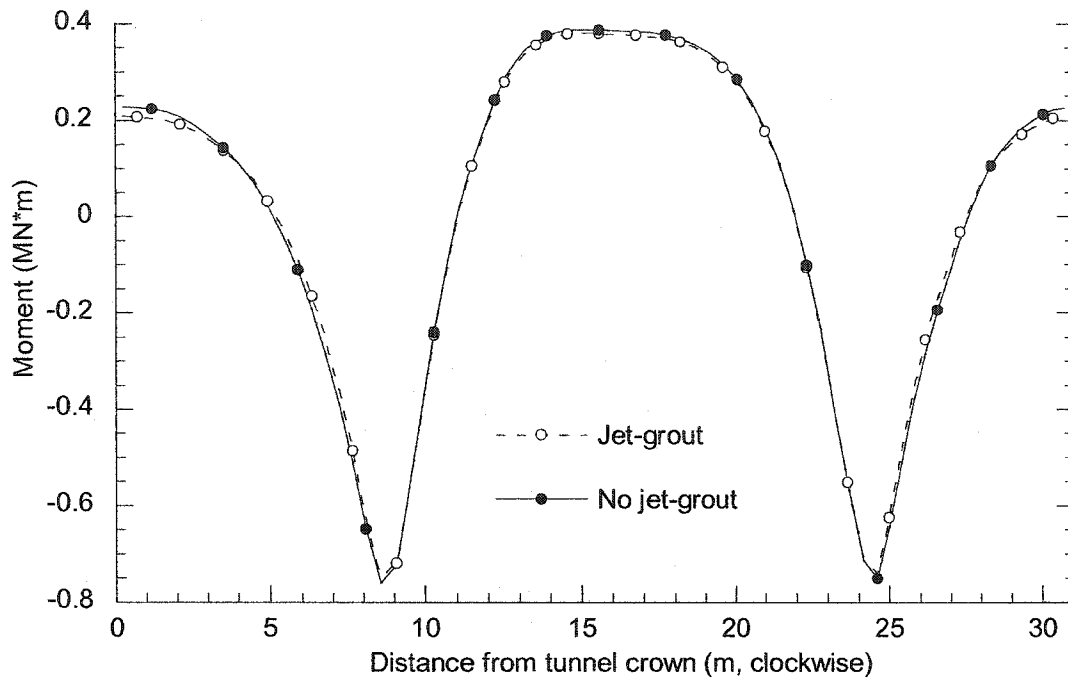


**Figure 5.28 - Modeled bending moment in the shotcrete liner with and without the presence of the jet-grout arch**

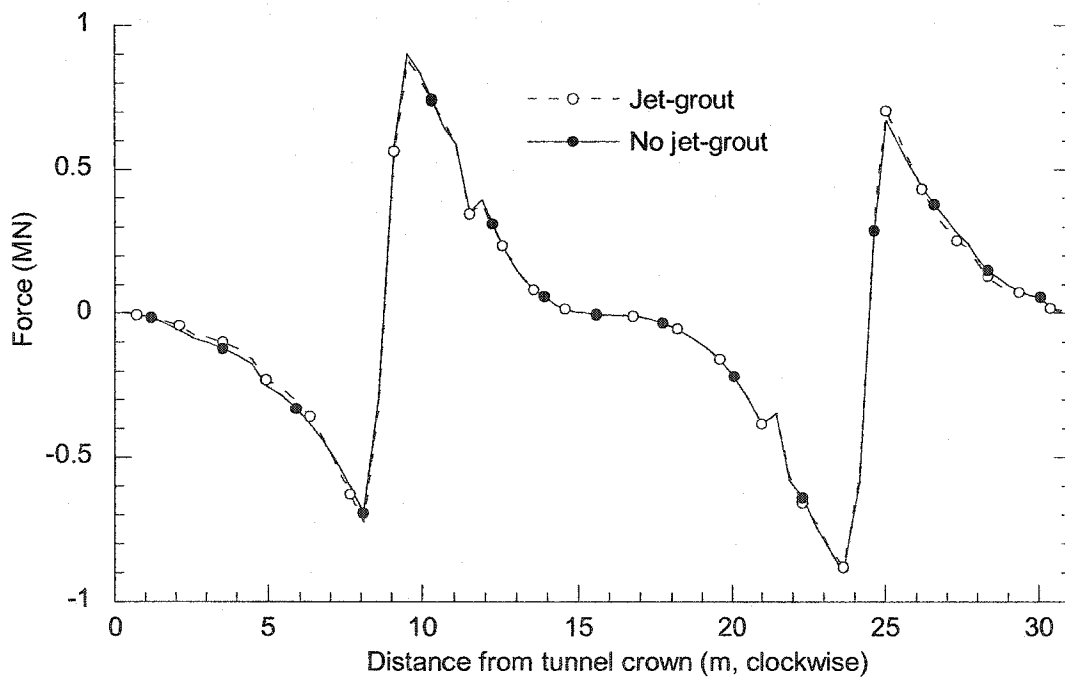


**Figure 5.29 - Modeled shear force in the shotcrete liner with and without the presence of the jet-grout arch**

## 5.6 Summary

The deformation assessment characterized the settlement with an empirical method and finite element modeling. The conclusions that arise from these analyses are:

- 1) The empirical analysis shows that the volume loss using the jet-grout to form a vault is low, comparable to EPB tunneling and very controlled NATM tunneling. The assessment of the trough width shows a narrow settlement trough, with the trough width parameter less than the width of the excavation.
- 2) The elastic settlements in the FEM result in a trough width wider than observed, leading to the hypothesis that there is plastic straining of the soil. Due to the narrow settlement trough, these plastic settlements likely form as shear bands that form near the tunnel crown and extend steeply to the surface.
- 3) The finite element analysis shows the necessity of using a refined mesh to simulate the formation of shear bands.
- 4) The plastic straining observed in the final trial form adjacent to the installation of previous sets of jet-grout. This is due to the higher jet-grout pressures heaving the soil. The soil above the previous set of jet-grout is held in place due to the stiffness of the jet-grout. The plastic strains occur where there is this contrast in stiffness.
- 5) The best match between the observed and modeled settlements occurred when the grout was given a peak pressure greater than overburden, reducing to a lesser maintained pressure. This method produced shear bands resulting in a narrow settlement trough.
- 6) The jet-grout vault appeared to be effective in limiting deformations ahead of the face; this is likely due to the reduction of 3 dimensional deformations. The small increase in settlements and the nominal increase in shotcrete liner loads when the

jet-grout vault was removed prior to the installation of the liner and the high value of the second softened Young's modulus suggest that the jet-grout vault has a limited role in taking the final excavation loads.

- 7) The back analyzed values are most likely not unique. There may exist a set of solutions that result in the formation of shear bands that will provide a narrow settlement trough.

## 6 Conclusions and Recommendations

### 6.1 Conclusions

This thesis investigated the use of sub-horizontal jet grout columns for preliminary excavation support. This was done with a laboratory testing program to define the time dependant mechanical properties of grout using a high early strength cement, with a mix design and environmental conditions similar to field conditions. The effect of the role of the jet grouting in the surface deformations during construction of the heading of the Aeschertunnel was evaluated using the finite element method.

The conclusions that arise are:

The laboratory testing shows that the development of strength and stiffness in jet grout is dependent on the time-temperature history of the grout. The insulation properties in the lab were selected so that the time temperature path in the lab would follow the time temperature path in the field. The development of the stiffness follows the same trend as the development of the strength. The laboratory testing showed that the 6 hour strength 15 kPa increasing to 3 MPa at 24 hours. The stiffness increased from 7.5 MPa at 6 hours to 675 MPa at 24 hours. In this period between 6 and 24 hours the grout reaches approximately two-thirds of its 3-day strength and stiffness. Measurements of the heat produced in the hydration showed that the strength and stiffness development follow the total heat production. This may be of use in construction to determine when the jet grout has sufficiently set so that it won't be damaged by further construction activities.

The use of jet grout columns to form a vault ahead of the excavation face prevented collapse of the tunnel, providing a safe working environment. The settlement profile had a narrow trough width and little volume loss. The construction technique also limited the settlements ahead of the tunnel face to 30% of the final settlements. There were observations of grout pressurization, as seen in the failure of the shotcrete liner and heaving of the surface.

The finite element analysis showed that the settlements observed are influenced by the jet grouting process. The build up of pressures during grouting can result in heaving of the ground and the formation of shear bands. When the peak grout pressure was sufficiently high, shear bands formed in the till. The use of a lower residual pressure keeps the overall heave in the model in the range of values observed during construction of the Aeschertunnel. The volume loss due to shrinkage and loss of bleed water during hydration justify the existence of a lower residual pressure.

The formation of shear bands in the finite element method is aided by using very refined meshes and strain softening soil behavior.

The relatively high value (95%) of the softened Young's modulus prior to the final excavation suggests that the jet grout vault limits the deformations in direction of the tunnel axis. This is also supported by the limited settlements ahead of the tunnel face.

The jet grout vault has a limited role in supporting the final excavation. The small increase in settlements with the removal of the vault prior to final excavation and the high value of the second softening support this. The use of a high value in the second softening results in smaller deformations in this stage, thus limits the loads on the jet grout.

The nature of the construction timing used resulted in little dependence of the settlements on the time dependent grout properties. The grout was installed in sets during which period there would be little increase in strength or stiffness. The setting time between the installation of set of jet grout columns was long enough to ensure that the grout had passed well beyond its peak in hydration. This provides grout that has developed most of its strength and stiffness.

## 6.2 Recommendations

When installing jet grout columns in a sequential manner, the delayed hardening results in the installation of subsequent jet-grout columns affecting earlier installations. When jet-grout columns are installed in a serial manner one next to another the existence of pressures on the soil from the installation of a jet grout column cause the adjacent unhardened columns to also exert pressure on the soil. This causes the grout of columns to act as a pressurized panel that result in pressures that cause the soil to heave and shear. To mitigate this problem the sequence of column installation may be altered so that unhardened jet grout columns are sufficiently spaced from each other to prevent the group from creating forces large enough to heave the soil above the tunnel.

Measuring the temperature of jet grout columns may provide an valuable, non destructive method in evaluating when they have hardened. This may be done with the insertion of a thermistor into the jet grout column after installation.

Care must be taken during the process to ensure that the soil is well mixed and grout pressures within the column are kept to a minimum to prevent heaving of the ground. Current jet grouting methods provide very good control over the jet grouting parameters. These parameters are controlled by the jet grouting rig operator based upon their observations, most importantly of spoil return from the borehole. The inclusion of measurements of the pressure within the jet grout during installation, or quantifying the spoil return may improve the control of heaving.

### **6.2.1 Future research**

In monitoring the ground deformation patterns in the construction of future tunnels using the jet-grout technique with similar jet-grout column installation sequencing, it would be of interest to install instrumentation that would measure the sub-surface deformations. These measurements could then confirm the presence of the shear bands that caused the narrow settlement trough.

The process of jet grouting, particularly the build up of pressures within the grouted zone, is dominant over the ground conditions. This is perhaps the most significant aspect to consider when using jet grout. If greater control is available over the pressures within the grouted zone, or understanding about the development of these pressures is increased, the jet grouting technique may find wider applications.



## 7 Bibliography

- Attwell, P. B., Hurrell, M. R. 1985. Settlement development caused by tunnelling in soil. *Ground Engineering* **18**(8): pp. 17-20.
- Beveridge, G. S. C., Schechter, R.S. 1970. **Optimization: Theory and Practice**. New York, McGraw-Hill, p. 773.
- Bishop, A. W., Webb, D.L., Lewis, P.I. 1965. Undisturbed samples of London Clay from the Ashford Common shaft: Strength-effective stress relationships. *Geotechnique* **15**(1): pp. 1-31.
- Box, M. J., Davies, D., Swann, W.H. 1969. **Non-linear optimization techniques**. Edinburg, Oliver & Boyd, p. 60.
- Brill, G. T., Burke, G. K., Ringen, A. R. 2003. A ten year perspective of jet grouting: Advancements in applications and technology. Proceedings of the 3rd international conference - Grouting and Ground Treatment, New Orleans, ASCE, pp. 218-235.
- Bruce, D. A., Boley, D. L., Gallavresi, F. 1987. New developments in ground reinforcement and treatment for tunnelling. Proceedings - 1987 Rapid Excavation and Tunnelling Conference, New Orleans, LA, USA, Society of Mining Engineers, Inc., pp. 811-835.
- Bye, G. C. 1983. **Portland Cement: composition Production and Properties**. New York, Pergamon Press, p. 149.
- Chambon, P., Corte, J-F. 1994. Shallow tunnels in cohesionless soil; Stability of the tunnel face. *Journal of Geotechnical Engineering* **120**(7): pp. 1149-1165.

- Cooper, L., Stienberg, D. 1970. **Introduction to Methods of optimization**. Toronto, W.B. Saunders Company, p. 381.
- Croce, P., Flora, A. 2000. Analysis of single fluid jet grouting. *Geotechnique* **50**(6): pp. 739-750.
- Di Cervia, A. R. 2000. New techniques in difficult ground tunnelling. *Transportation Research Record*(1740): pp. 175-181.
- Fang, Y.-S., Liao, J. J., Lin, T-K. 1994. Mechanical Properties of jet grouted soilcrete. *Quarterly journal of engineering geology* **27**(3): pp. 257-265.
- Fang, Y.-S., Liao, J. J., Sze, S-C. 1994. An empirical strength criterion for jet grouted soilcrete. *Engineering Geology* **37**(3): pp. 285-293.
- Fries, T. 2000. ausfahrtstunnel Ristet - erfahrungen aus dem Lockergestainsvortrieb. *Mettielungen der Schweizerischen gesellschaft fur Boden- und Felsmechanik, Zurich, Societe Suisse de Mechanique des Sols et des Roches*, pp. 33-38, in German.
- Gioda, G., Locatelli., L. 1999. Back analysis of the measurement performed during the excavation of a shallow tunnel in sand. *International Journal for Numerical and Analytical Methods in Geomechanics* **23**(13): pp. 1407-1425.
- Gioda, G., Swoboda, G. 1999. Developments and applications of the numerical analysis of tunnels in continuous media. *International Journal for Numerical and Analytical Methods in Geomechanics* **23**(13): pp. 1393-1405.
- Goodman, R. E. 1989. **Introduction to Rock Mechanics**. New York, John Wiley & Sons, p. 562.

- Guntlin, M. 2000. Stutzwand Tantenholz, ein permanent verankertes bauwerk der neuen Generation. Metteilungen der Schweizerischen gesellschaft fur Boden- und Felsmechanik, Zurich, Societe Suisse de Mechanique des Sols et des Roches, pp. 39-49, in German.
- Heuer, R. E., Virgens, D.L. 1987. Anticipated behavior of silty sands in tunnelling. Proceedings - 1987 Rapid Excavation and Tunnelling Conference, New Orleans, LA, USA, Society of Mining Engineers, Inc., pp. 221-237.
- Kauschinger, L. J., Hankour, R., Perry, E.B. 1992. Jet Grouting: State-of-the-practice. ASME Special Publication No. 30, New Orleans, LA, USA, ASME, pp. 169-181.
- Kauschinger, L. J., Hankour, R., Perry, E.B. 1992. Methods to estimate the composition of jet grouted bodies. ASME Special Publication No. 30, New Orleans, LA, USA, ASME, pp. 194-205.
- Kleboth, P. 2000. Die eologie im Bereich der Umfahrung Birmensdorf. Metteilungen der Schweizerischen gesellschaft fur Boden- und Felsmechanik, Zurich, Societe Suisse de Mechanique des Sols et des Roches, pp. 3-9, in German.
- Kosmatka, S. H., Panarese, W. C., Gissing, K. D, Macleod, N. F. 1995. **Design and Control of Concrete Mixtures 6th ed.** Ottawa, Canadian Portland Cement Association, p. 221.
- Ladd, C. C., Foott, R., Ishihara, K., Schlosser, f., Poulos, H.G. 1977. Stress deformation and strength characteristics. Proceedings, 9th International Conference on Soil Mechanics and Foundation Engineering, Tokyo, Foundation Publications Limited,, pp. 421-494.

- Larsson, R., Runesson, K., Sture, S. 1991. Finite element simulation of localized plastic deformation. *Archive of applied mechanics* 61(5): pp. 305-317.
- Leca, E., Leblais, Y., Kuhnhen, K. 2000. Underground works in soils and soft rock tunnelling. *GeoEng2000, An International Conference on Geotechnical & Geological Engineering*, Melbourne, Technomic Publishing, pp. 220-268.
- Loganthan, N., Poulos, H. G. 1998. Analytical prediction for tunneling induced ground movements in clays. *Journal of Geotechnical and Geoenvironmental Engineering* 124(9): pp. 846-856.
- Lunardi, P. Accessed 2002. The design and construction of tunnels using the approach based on the analysis of controlled deformation of rocks and soils.  
[www.rocksoil.com/publicazioni\\_ing.html](http://www.rocksoil.com/publicazioni_ing.html).
- Lunardini, V. J. 1981. **Heat transfer in cold climates**. New York, Litton Educational Publishing Inc., p. 751.
- Mair, R. J. 1996. Settlement effects of bored tunnels. *International Symposium on Geotechnical Aspects of Underground Construction in Soft Ground*, London, A.A.Balkema, pp. 43-53.
- Mair, R. J., Taylor, R.N. 1997. Bored tunneling in an urban environment. 14th *International Conference on Soil Mechanics and Foundation Engineering*, Hamburg, A.A. Balkema, pp. 2353-2385.
- Mair, R. J., Taylor, R.N. 1997. Theme lecture: Bored tunneling in the urban environment. 14 *International Conference on Soil Mechanics and Foundation Engineering*, Hamburg, A.A. Balkema, pp. 2353-2385.

- Mussger, K., Koinig, J., Reischl, S. 1987. Jet grouting in combination with NATM. Proceedings - 1987 Rapid Excavation and Tunnelling Conference, New Orleans, LA, USA, Society of Mining Engineers, Inc., pp. 292-308.
- New, B. M., O'Reilly, M.P. 1982. Tunneling induced ground movements, predicting their magnitude and effects. Proceedings, Tunneling '82, London, Institution of Mining and Metallurgy, pp. 173-182.
- Ottaviani, M., Pelli, F. 1983. Influence of depth and distance between the axis on surface displacement due to the excavation of twin shallow tunnels. Proceedings - International Symposium on Engineering Geology and Underground Construction, Lisbon, Portugal, Laboratório Nacional de Engenharia Civil, pp. 247-256.
- Otto, B., and Thut, A. 1991. Assessment of the deformation behavior of the jet grouted arch support of Monteolimpino Railway Tunnel using in-situ measurements and back analysis. Proceedings of the 3rd International Symposium on Field Measurements in Geomechanics, Oslo, A.A. Balkema, pp. 883-844.
- Pastor, M., Peraire, J., Zienkiewicz, O.C. 1991. Adaptive remeshing for shear band localization problems. Archive of applied mechanics **61**(1): pp. 30-39.
- Peck, R. B. 1969. Deep excavations and tunnelling in soft ground. 7th International Conference on Soil Mechanics and Foundation Engineering, Mexico City, pp. 225-290.
- Pellegrino, G. Accessed 2002. Soil improvement technologies for tunnelling: Selected case histories. [www.nicholson-rodio.com/papers/soil\\_improvement.htm](http://www.nicholson-rodio.com/papers/soil_improvement.htm).
- Poulikakos, D. 1994. **Conduction Heat Transfer**. New Jersey, Prentice-Hall, p. 353.

- Powderham, A. J., Hitchcock, A., Taylor, S., Rice, P. M. 2002. Ground movement control for tunnel jacking under roadway.
- Robinson, R. A., Kukcer, M. S., Parker, H. W. 1991. Ground behavior in glacial soils for the Seattle transit tunnels. Proceedings of the 10th Rapid Excavation and Tunnelling Conference, Seattle, WA, USA, Society of Mining Engineers, Inc., pp. 93-117.
- Rowe, R. K., Lo, K. Y., Kack, G. J. 1983. Method of estimating surface settlement above tunnels constructed in soft ground. *Canadian Geotechnical Journal* **20**(1): pp. 11-22.
- Sagesta, C. 1987. Analysis of undrained soil deformation due to ground loss. *Geotechnique* **37**(4): pp. 301-320.
- Shibazaki, M. 2003. State of practice of jet grouting. Proceedings of the 3rd international conference - Grouting and Ground Treatment, New Orleans, ASCE, pp. 199-217.
- Skiker, A., Chambon, P., Leca, E., Garnier, J. 1994. Face stability of tunnels using the mechanical precutting method. *Centrifuge '94*, Singapore, A.A. Balkema, pp. 713-718.
- Stallebras, G., R.J., Taylor, R.N. 1996. A finite element study of ground movements measured in centrifuge model tests of tunnels. Proceedings - International Symposium on Geotechnical Aspects of Underground Construction in soft soils, London, A.A. Balkema, pp. 595-600.
- Sterpi, D. 1999. An analysis of geotechnical problems involving strain softening effects. *International Journal for Numerical and Analytical Methods in Geomechanics* **23**(13): pp. 1427-1454.

- Swoboda, G. 1979. Finite element analysis of the New Austrian Tunneling Method (NATM). Proceedings of the 3rd international conference on numerical methods in geomechanics, Aachen, Germany, A.A. Balkema, pp. 604-618.
- Swoboda, Q., Ichikawa, Y., Dong, Q., Zake, M. 1999. Back analysis of large geotechnical models. International Journal for Numerical and Analytical Methods in Geomechanics 23(13): pp. 1455-1472.
- Taylor, H. F. W. 1990. **The Chemistry of Cements**. New York, Academic Press Inc, p. 459.
- Terzaghi (1950). Geologic aspects of soft-ground tunneling. Applied Sedimentation. P. D. Trask. New York, Wiley: 193-209.
- Turner, W. C., Malloy, J. F. 1981. **Thermal Insulation Handbook**. New York, McGraw-Hill, p. 629.
- US Army Corps of Engineers. 1988. **TM 5-852-6, Arctic and Subarctic Construction - Calculation Methods for Determination of Depths of Freeze and Thaw in Soils**, Joint Departments of the Army and Air Force USA, p. 56.
- Verruijt, A., Booker, J.R. 1996. Surface settlements due to the deformation of a tunnel on an elastic half plane. Geotechnique 46(4): pp. 753-756.
- Wong, I. H., Poh, T. Y. 2000. Effects of jet grouting on adjacent ground and structures. Journal of Geotechnical and Geoenvironmental Engineering 126(3): pp. 247-256.
- Zielenkiewics, W., Kaminski, M. 2001. A conduction calorimeter for measuring the heat of cement hydration in the initial hydration period. Journal of Thermal Analysis and Conduction Calorimetry 65: pp. 335-340.

Zienkiewicz, O. C., Huang, M., Pastor, M. 1995. Localization problems in plasticity using finite element with adaptive remeshing. *International Journal for Numerical and Analytical Methods in Geomechanics* 19(3): pp. 127-148.



## **A. APPENDIX Aeschertunnel Field Investigation**

This appendix includes the grout installation sequence for Basel and Luzerne profiles 1 and 2, the observed settlements at Basel and Luzerne profiles 1 and 2 and the Tantenholtz portal. Also included are detailed drawing of the tunnel cross section.

**Table A.1 Grout installation sequence - Luzerne**

Profile 1, Luzern			Profile 2, Luzern		
Column Number	Date	Time of Completion	Column Number	Date	Time of Completion
27	2/5/2003	14:37	16	2/14/2003	15:18
26	2/5/2003	15:18	17	2/14/2003	16:08
25	2/5/2003	15:46	18	2/14/2003	16:45
24	2/5/2003	16:22	19	2/14/2003	17:35
23	2/5/2003	16:52	20	2/14/2003	18:07
22	2/5/2003	17:23	21	2/14/2003	18:48
21	2/5/2003	17:59	22	2/14/2003	20:33
20	2/5/2003	18:28	23	2/14/2003	21:27
19	2/5/2003	18:57	7	2/17/2003	15:28
18	2/5/2003	19:28	8	2/17/2003	16:05
17	2/5/2003	20:02	9	2/17/2003	16:35
16	2/5/2003	20:33	10	2/17/2003	17:05
15	2/5/2003	21:03	11	2/17/2003	17:55
14	2/5/2003	21:33	12	2/17/2003	18:26
1	2/6/2003	16:53	13	2/17/2003	19:07
3	2/6/2003	17:25	14	2/17/2003	21:41
5	2/6/2003	17:58	31	2/18/2003	15:57
7	2/6/2003	18:30	30	2/18/2003	16:27
9	2/6/2003	19:01	29	2/18/2003	18:34
11	2/6/2003	19:32	28	2/18/2003	19:06
13	2/6/2003	20:09	27	2/18/2003	19:44
39	2/6/2003	21:05	26	2/18/2003	20:13
37	2/6/2003	21:44	25	2/18/2003	20:45
38	2/7/2003	10:32	24	2/18/2003	21:17
36	2/7/2003	11:11	39	2/19/2003	9:07
35	2/7/2003	11:50	38	2/19/2003	9:35
34	2/7/2003	12:23	37	2/19/2003	10:07
33	2/7/2003	13:02	36	2/19/2003	10:37
32	2/7/2003	14:11	35	2/19/2003	11:09
31	2/7/2003	14:20	34	2/19/2003	11:38
30	2/7/2003	14:51	33	2/19/2003	12:09
29	2/7/2003	15:45	32	2/19/2003	12:39
28	2/7/2003	16:17	1	2/19/2003	16:34
2	2/10/2003	9:08	2	2/19/2003	17:14
4	2/10/2003	9:45	3	2/19/2003	17:52
6	2/10/2003	10:22	4	2/19/2003	18:21
8	2/10/2003	11:17	5	2/19/2003	18:51
10	2/10/2003	11:27	6	2/19/2003	19:25
12	2/10/2003	12:22	15	2/19/2003	20:21

**Table A.2 Grout installation sequence - Basel**

Profile 1, Basel			Profile 2, Basel		
Column Number	Date	Time of Completion	Column Number	Date	Time of Completion
13	1/14/2003	14:12	28	12/3/2003	18:14
14	1/14/2003	14:47	27	12/3/2003	18:44
15	1/14/2003	16:44	26	12/3/2003	19:15
16	1/14/2003	17:14	25	12/3/2003	19:43
17	1/14/2003	17:47	24	12/3/2003	21:34
18	1/14/2003	18:21	23	12/3/2003	22:05
19	1/14/2003	18:52	10	12/5/2003	13:13
20	1/14/2003	19:24	11	12/5/2003	13:42
21	1/14/2003	20:08	12	12/5/2003	14:20
26	1/14/2003	22:11	13	12/5/2003	17:32
25	1/14/2003	22:43	14	12/5/2003	18:02
24	1/14/2003	23:13	15	12/5/2003	18:35
23	1/14/2003	23:49	16	12/5/2003	19:08
22	1/15/2003	0:18	17	12/5/2003	20:10
39	1/15/2003	15:55	18	12/5/2003	20:42
38	1/15/2003	16:25	19	12/5/2003	21:41
37	1/15/2003	16:57	8	12/6/2003	18:30
36	1/15/2003	17:34	9	12/6/2003	19:02
35	1/15/2003	18:12	20	12/6/2003	20:16
34	1/15/2003	19:13	21	12/6/2003	20:45
33	1/15/2003	19:42	22	12/6/2003	21:23
32	1/15/2003	20:13	39	12/9/2003	18:43
31	1/15/2003	20:46	38	12/9/2003	19:14
30	1/15/2003	21:19	37	12/9/2003	19:45
28	1/15/2003	23:39	36	12/9/2003	20:19
29	1/15/2003	23:45	35	12/9/2003	20:48
27	1/16/2003	0:12	34	12/9/2003	21:16
1	1/16/2003	16:32	33	12/9/2003	22:50
2	1/16/2003	17:07	32	12/9/2003	23:17
3	1/16/2003	17:39	31	12/9/2003	23:50
4	1/16/2003	18:09	30	12/10/2003	0:23
5	1/16/2003	19:04	29	12/10/2003	0:52
6	1/16/2003	19:33	1	12/10/2003	18:41
7	1/16/2003	20:05	2	12/10/2003	19:11
8	1/16/2003	20:38	3	12/10/2003	19:45
9	1/16/2003	21:08	4	12/10/2003	20:15
10	1/16/2003	22:51	5	12/10/2003	20:44
11	1/16/2003	23:22	6	12/10/2003	21:19
12	1/17/2003	1:23	7	12/10/2003	22:53

**Table A.3 Observed settlement – Profile 1**

Date	Face Position		Ground Condition	Settlement Point					
	Luzerne	Basel		F2	F5	F8	F11	F14	F16
	922	972		0	0	0	0	0	0
11/28/02	949	983		-1.3	-1.7	-1.3	-1.6	-2	-1.2
12/02/02	951	994		-1.3	-2.4	-1.2	-1.2	-1.3	-1.4
12/05/02	957	994		-0.6	-3	-1.7	-1.4	-1.3	-0.6
12/09/02	964	994		-2.3	-4.2	-1.8	-2.3	-1.2	-0.7
01/13/03	977	1005	Frozen	-4	-16.1	1.6	2.5	-1.9	8
01/16/03	984	1005	Frozen	-4.2	-16.7	1.6	2.1	-0.2	8.9
01/23/03	988	1016	Wet	-5.3	-22.6	1	0.6	0.2	8.3
01/27/03	995	1016	Wet	-4.8	-22.7	0.7	1.5	-0.1	9
01/30/03	995	1027	Snow	-5	-24	0.4	1.1	-2.2	8.6
02/03/03	1002	1027	Snow	-4.9	-24.5	0.3	0.5	-2.1	8.7
02/06/03	1002	1027	Snow	-5.3	-24.9	0.1	-0.3	-4.7	6.4
02/10/03	1006	1038	Snow	-5.7	-24.6	-0.3	-1.2	-4.5	15.5
02/13/03	1017	1038	Snow	-5.2	-25	-0.8	-4	-14.6	13.8
02/17/03	1017	1047	Snow	-4.9	-25.3	-0.8	-3.7	-16.7	26.7
02/26/03	1028	1053	Snow	-4.9	-26	-1.4	-5.5	-22.2	25.9
02/27/03	1028	1060	Snow	-5.3	-25.1	-0.6	-5.9	-22.7	27
02/28/03	1028	1060	Wet	-4.2	-24.7	0.4	-4.4	-21.8	27.8
03/03/03	1028	1060	Wet	-7.1	-25.6	-1	-6.5	-23.8	26.4
03/06/03	1039	1060	Wet	-7	-26.4	-2	-6.2	-23.8	26.6
03/10/03	1039	1068	Wet	-7	-26.4	-1.8	-6.8	-24.5	25.1
03/11/03	1039	1070	Wet	-6.4	-26.5	-2.1	-7	-25.2	25.2

**Table A.4 Observed settlement – Profile 2**

Date	Face Position		Ground Cond.	Settlement Point						
	Luzerne	Basel		F3	F6	F9	F12	F15	F17	F18
	922	972		0	0	0	0	0	0	0
11/28/02	949	983		-1.1	-2	-1.4	-1.6	-1.7	-0.5	-1
12/02/02	951	994		-0.7	-2.2	-2.3	-1.3	-0.7	0	-0.4
12/05/02	957	994		-1	-1.3	-2.5	-1.1	-0.6	-0.7	-0.4
12/09/02	964	994		-0.9	-1.8	-1.4	-1	-1	-0.3	0.5
01/13/03	977	1005	Frozen	-1.4	-4.7	-0.3	4.8	-1.2	7.4	4.4
01/16/03	984	1005	Frozen	-1.2	-7.2	-0.2	2.8	0	7.3	2.6
01/23/03	988	1016	Wet	-6	-14.6	-2.5	2.6	-1.2	6	2.3
01/27/03	995	1016	Wet	-5.8	-15.2	-3.1	1.2	0.2	5.6	3.4
01/30/03	995	1027	Snow	-5.4	-18.7	-3.8	2.7	-1.6	7.2	3
02/03/03	1002	1027	Snow	-4.4	-19.4	-3.1	0.4	-0.5	6.4	4.5
02/06/03	1002	1027	Snow	-5	-21.1	-3.1	2.9	-2.4	7.4	3
02/10/03	1006	1038	Snow	-4.7	-20.9	-3.8	1.9	-2	6.6	3.2
02/13/03	1017	1038	Snow	-4.5	-22	-3.5	-1.2	-2.5	6	2.5
02/17/03	1017	1047	Snow	-4.8	-23.3	-3.4	0.1	-4.9	7.2	3.3
02/26/03	1028	1053	Snow	-5.1	-22.5	-1.6	-3.5	-13.5	7.1	4
02/27/03	1028	1060	Snow	-5.1	-22.5	-2.2	-3.9	-14.2	6.6	3.3
02/28/03	1028	1060	Wet	-4.5	-22.4	-2.1	-3.1	-14.4	7.5	4.8
03/03/03	1028	1060	Wet	-5.9	-23.4	-2.2	-3.9	-16.9	5.5	2.6
03/06/03	1039	1060	Wet	-5.9	-23.8	-3.1	-6.6	-20.4	6.7	4.2
03/10/03	1039	1068	Wet	-7.4	-24.1	-4.1	-7.1	-21.5	5.5	3.7
03/11/03	1039	1070	Wet	-6.8	-23.9	-3.6	-5.9	-20.8	5.3	3.4

**Table A.5 Observed settlements - Tantenholz**

Date	Face Position		Settlement Point							
	lu	bs	1	2	3	4	5	6	7	8
6/27/2000	74	160	0	1	1	-3	-1	3	2	0
7/6/2000	83	168	1	2	1	-5	1	2	0	-2
7/12/2000	90	178	1	0	-1	-10	-1	2	0	-4
7/20/2000	99	184	0	-1	-4	-14	-3	1	0	-5
7/27/2000	105	188	-2	-10	-9	-16	0	0	-2	-7
8/3/2000	107	192	-3	-18	-12	-18	-13	0	-2	-8
8/9/2000	113	193	-5	-115	-16	-19	-13	1	-2	-7
8/15/2000	122	197	-9	-216	-19	-22	-13	-1	-4	-10
8/22/2000	130	195	-14	-296	-21	-20	-14	-1	-7	-12
8/30/2000	138	195	-22	-331	-24	-27	-14	-5	-36	-22
9/21/2000	141(a)	195	-25	-339	-27	-27	-15	-5	-43	-24
10/4/2000	150	195	-23	-338	-23	-24	-10	-3	-55	-23
10/23/2000	163	195	-28	-345	-28	-29	-15	-10	-73	-30
12/7/2000	197	223	-28	-349	-29	-30	-10	-13	-84	-33
2/19/2001	227	260	-31	-356	-32	-39	-15	-16	-90	-35
5/9/2001	293	321	-34	-360	-34	-42	-13	-19	-96	-40
11/12/2001	520	490	-37	-370	-40	-58	-15	-21	-102	-65
9/23/2002	874	912	-40	-377	-45	-71	-11		-114	-89

Date	Face Position		Settlement Point							
	lu	bs	8	9	10	11	12	13	14	15
6/27/2000	74	160	0	-34	1	2	2	2	-5	-14
7/6/2000	83	168	-2	-55	0	1	1	-1	-85	-43
7/12/2000	90	178	-4	-64	-1	1	1	-4	-198	-53
7/20/2000	99	184	-5	-69	-1	0	0	-12	-299	-58
7/27/2000	105	188	-7	-74	-1	-1	-2	-18	-324	-61
8/3/2000	107	192	-8	-76	-2	-1	-2	-25	-342	-64
8/9/2000	113	193	-7	-76	0	-1	-1	-35	-356	-64
8/15/2000	122	197	-10	-81	-1	-1	-3	-59	-368	-67
8/22/2000	130	195	-12	-84	-2	0	-1	-61	-372	-67
8/30/2000	138	195	-22	-90	-3	-1	-4	-66	-379	-70
9/21/2000	141(a)	195	-24	-92	-3	-1	-4	-68	-384	-71
10/4/2000	150	195	-23	-91	3	3	1	-66	-383	-67
10/23/2000	163	195	-30	-99	-1	-1	-4	-73	-390	-72
12/7/2000	197	223	-33	-104	1	-4	-20	-85	-396	-72
2/19/2001	227	260	-35		-1	-16	-35	-93	-406	-74
5/9/2001	293	321	-40		0	-19	-41	-99		-76
11/12/2001	520	490	-65		1	-22	-56	-119		-81
9/23/2002	874	912	-89		4	-25	-62	-128		-82

(a) Luzerne face collapse

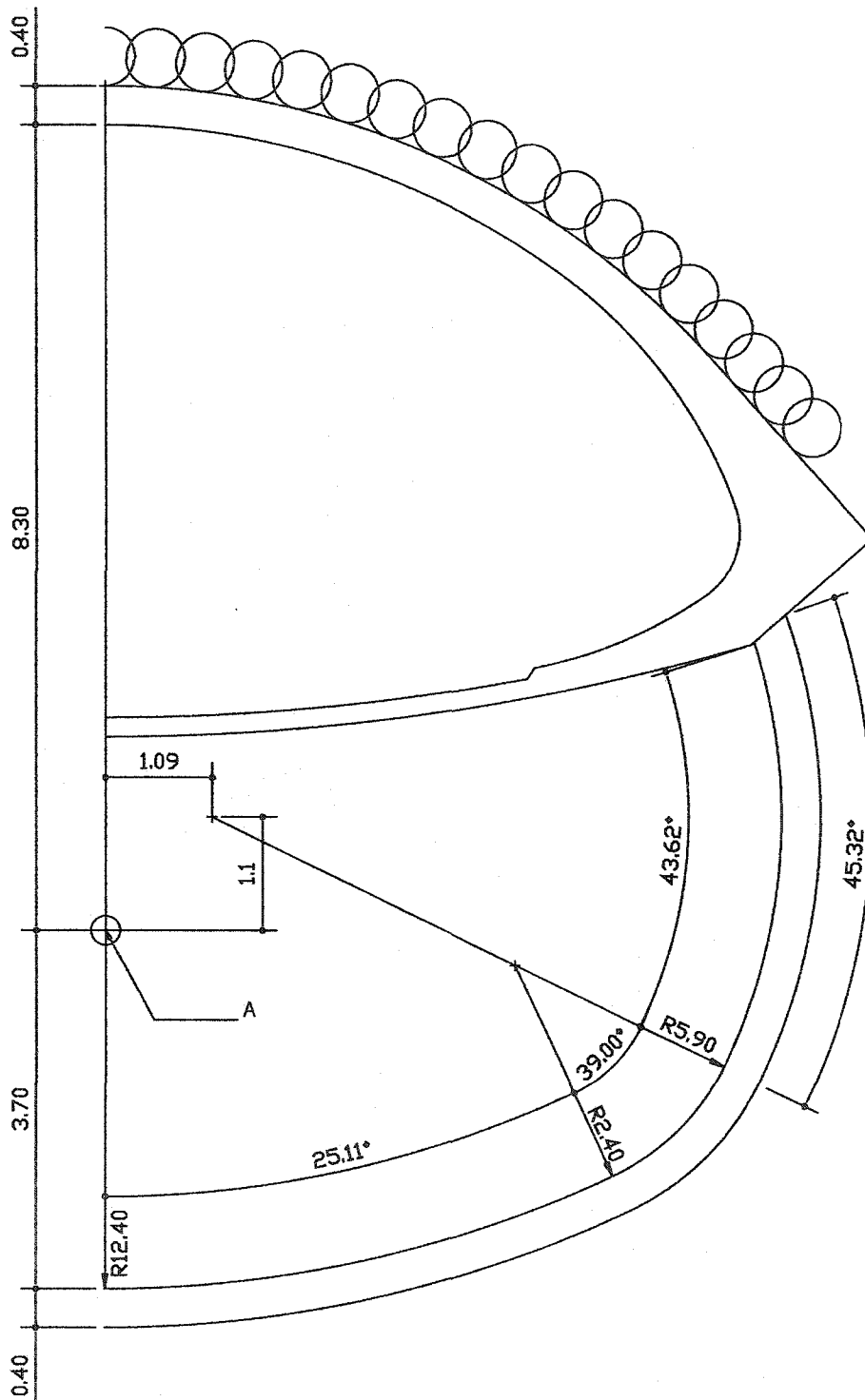


Figure A.1 Tunnel section

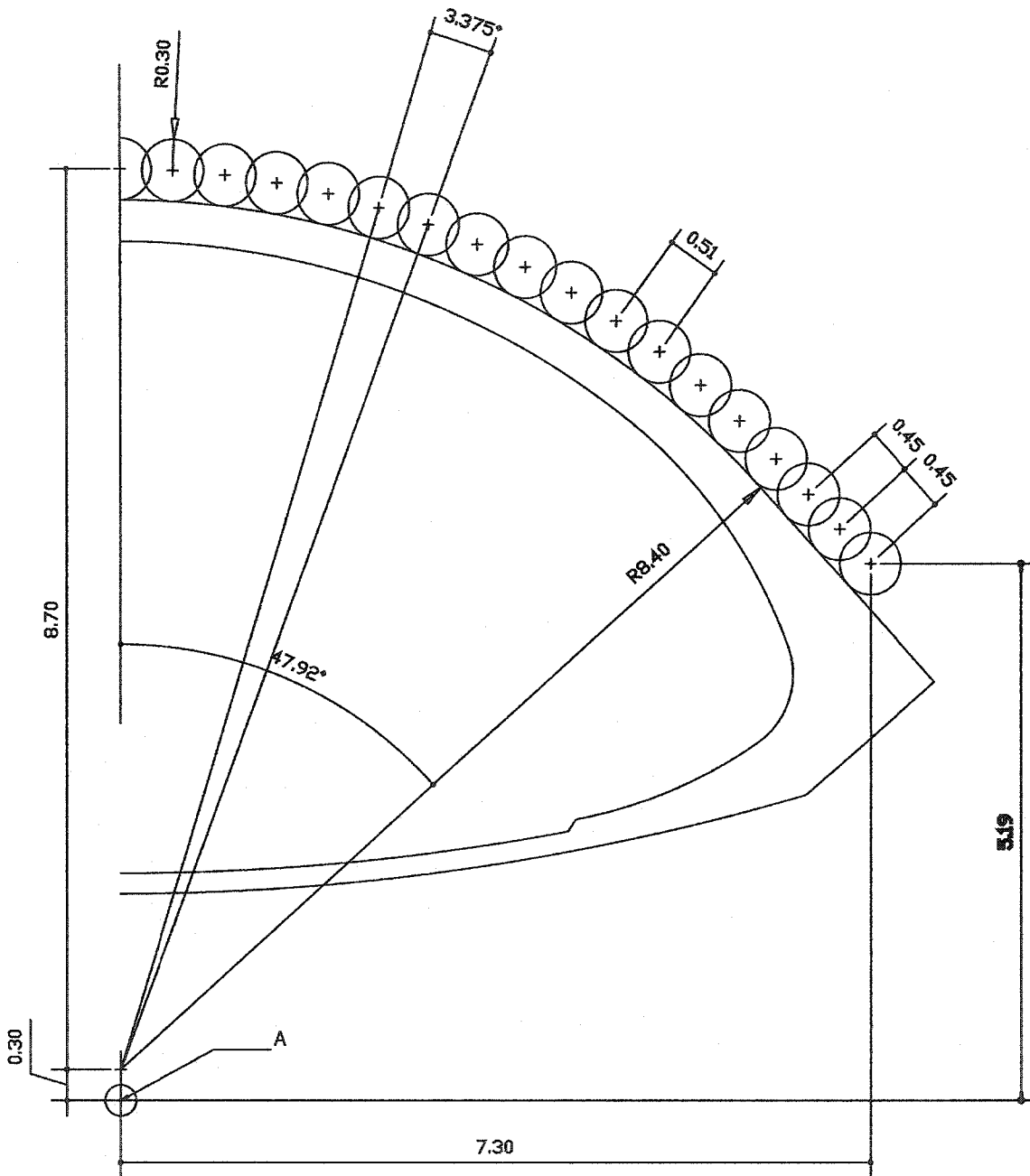


Figure A.2 Heading detail - grout



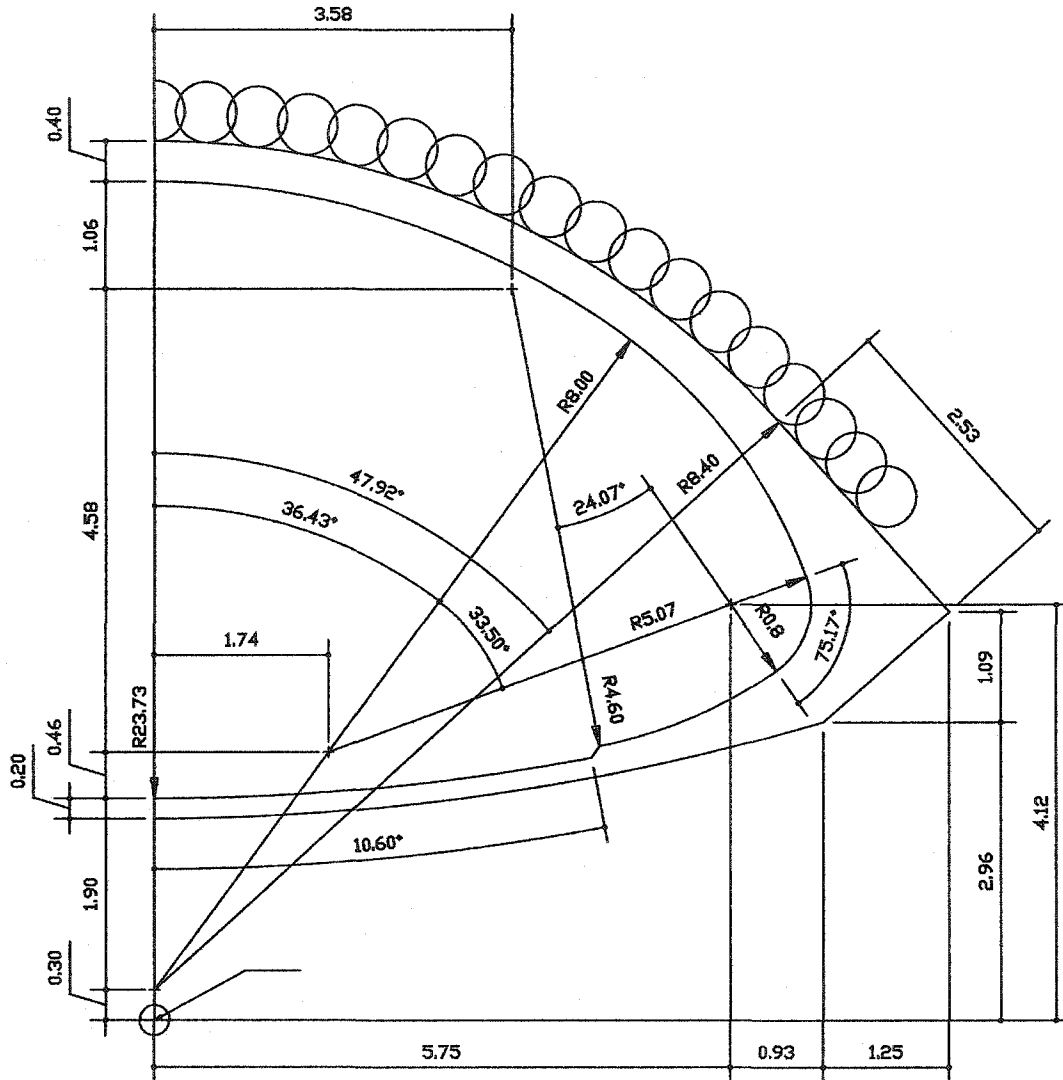


Figure A.3 Heading detail

## **B. APPENDIX Laboratory testing of grout**

This appendix includes the summaries for the uniaxial tests, the residual strength tests, and vane shear tests

**Table B.1 Uniaxial testing results**

Cast No.	1	1	2	2	2	2	2
Cyl No.	1	2	1	2	3	4	5
Time (hr)	13.4	24.2	6.0	7.1	9.7	28 day	28 day
UCS (kPa)	1777	3684	15.2	73.5	353	13300	14600
E (MPa)	347	668	0	0	116	1330	1450
Tension (kPa)						1310	1520
$\rho$ (kN/m <sup>3</sup> )		18.9	18.9	18.9	18.6	18.9	18.9

Cast No.	3	3	3	3	3	4	4
Cyl No.	1	2	3	4	5	1	2
Time (hr)	13.8	18.6	24.1	72.1	28 day	5.9	7.1
UCS (kPa)	1855	2940	3918	5597	14700	14.6	52.2
E (MPa)	375	653	718.5	1001	1490	4.84	23.3
Tension (kPa)	228	378	368	774	1450	4.0	10.7
$\rho$ (kN/m <sup>3</sup> )	19.1	18.7	18.8	18.7	19.1	18.5	19.3

Cast No.	4	4	4	5	5	5	5
Cyl No.	3	4	5	1	2	3	4
Time (hr)	8.5	10.5	47.6	13.8	18.5	24.0	72.7
UCS (kPa)	182	693	4473	1426	2728	3641	5088
E (MPa)	60.06	212	915.5	415.7	597	633	830
Tension (kPa)	56	124	1116	207	334	408	786
$\rho$ (kN/m <sup>3</sup> )	19.0	19.2	19.1	18.5	18.5	18.3	18.6

Cast No.	6	6	6	6	6	7	7
Cyl No.	1	2	3	4	5	1	2
Time (hr)	5.7	6.8	8.2	10.3	71.6	13.7	18.5
UCS (kPa)	12.3	34.0	136	481	5627	1809	2829
E (MPa)	5.7	11.79	53.3	151	865	454	672
Tension (kPa)	3.0	9.2	27	87	629	214	427
$\rho$ (kN/m <sup>3</sup> )	18.7	18.4	18.5	18.7	18.9	18.6	18.5

Cast No.	7	7	8	8	8	8	8
Cyl No.	3	4	1	2	3	4	5
Time (hr)	24.1	47.8	5.7	6.7	8.2	10.3	48.7
UCS (kPa)	3396	4000	7.8	33.6	134	497	4609
E (MPa)	745	838	5.68	24.4	36.8	125	921
Tension (kPa)	550	537	0.9	8.1	26	67	693
$\rho$ (kN/m <sup>3</sup> )	18.2	18.8	17.6	18.7	18.1	18.2	18.5

**Table B.2 Residual grout tests**

Cast No.	6	6	6	8	8	8
Cyl No.	1	2	3	1	2	3
Time 1 (hr)	6.0	7.0	8.5	6.0	7.0	8.5
Time 2 (hr)	24.6	24.5	24.7	24.6	24.5	24.7
UCS (kPa)	2680	2315	2207	2744	2313	2189
E (MPa)	556	529	474	547	456	393
$\rho$ (kN/m <sup>3</sup> )	18.5	18.5	18.1	18.0	18.2	18.1

Cast No.	9	9	9	9	9	9
Cyl No.	1	2	3	4	5	6
Time 1 (hr)	6.0	6.0	7.0	7.0	8.5	8.5
Time 2 (hr)	24.5	24.6	24.8	24.9	24.8	24.7
UCS (kPa)	2773	2998	2977	3050	3181	3263
E (MPa)	591	662	693	722	637	680
$\rho$ (kN/m <sup>3</sup> )	18.9	19.4	18.8	18.4	19.0	19.0

**Table B.3 Vane shear tests**

cast 2	Cu (kPa)	T (hh:mm)
	5.0	4:20
	5.0	4:20
	21.3	5:20
	23.1	5:25
	26.7	5:35

cast 4	Cu (kPa)	T (hh:mm)
	1.2	3:50
	1.3	3:50
	4.2	4:25
	6.1	4:37
	5.6	4:47
	7.9	5:00
	7.6	5:00
	9.1	5:07
	9.0	5:07
	12.8	5:24
	13.4	5:24
	18.3	5:31
	21.8	5:40

cast 6	Cu (kPa)	T (hh:mm)
	0.9	3:30
	1.3	3:45
	1.5	3:55
	4.6	4:30
	4.4	4:30
	11.5	5:10
	15.1	5:20

cast 8	Cu (kPa)	T (hh:mm)
	0.7	3:30
	0.7	3:30
	2.2	4:00
	3.0	4:20
	21.4	5:35

## **C. APPENDIX Numerical modeling**

This appendix includes the method used to calculate the liner properties as a composite, and the timing of the grout installations and corresponding material properties used in the numerical models.

## Calculation of liner properties

The elastic modulus and strength of the shotcrete and steel reinforcement liner were calculated as composite properties. The steel reinforcement used was 8mm diameter bars spaced 150 mm center to center on a grid formation. The crown had lattice girders at 1m spacing with two bars of 20 mm and one bar of 30mm and two layers of steel grid and 40 mm of shotcrete. The invert had one layer of steel grid and 20mm of shotcrete. The steel used had a 550 MPa yield, and the shotcrete used had a UCS of 20MPa. Table C.1 shows the equivalent Mohr-Coulomb parameters, assuming a friction angle of 35° for the shotcrete.

**Table C.1 Liner component properties**

	E (GPa)	c (MPa)	φ (deg)
Shotcrete	20	5.2	35
Steel	200	275	0

The equivalent Young's modulus was calculated based upon the relative proportions of the shotcrete and steel in the liner cross section (Equation C-1).

$$E_{composite} = \frac{A_{steel} \cdot E_{steel} + A_{shotcrete} \cdot E_{shotcrete}}{A_{steel} + A_{shotcrete}} \quad (C-1)$$

Yielding in compression results in the yielding of shotcrete first. The yield strain of the shotcrete is 0.1% and the yield strain of the steel is 0.275%. Based upon the assumption that the shotcrete will have a low residual strength the peak strength was assumed to have a steel and shotcrete component, with the load in the steel being limited to the maximum strain allowable in the shotcrete (Equation C-2). The steel component is treated as pure cohesion and the shotcrete component has cohesion and friction. The steel component of the strength is simply added to the shotcrete strength. The load in tension is assumed to only be taken up by the steel reinforcement (Equation C-3).

$$c_{comp} = c_{shotcrete} + \frac{0.1\% \cdot E_{steel} \cdot A_{steel}}{2 \cdot (A_{steel} + A_{shotcrete})} \quad (C-2)$$

$$c_{tens} = \frac{0.275\% \cdot E_{steel} \cdot A_{steel}}{2 \cdot (A_{steel} + A_{shotcrete})} \quad (C-3)$$



**Table C.2 Modelled grout timing and parameters**

Average setting time (hr)

		Model Stage				
		5	7	9	11	13
Jet grout set	1	24.3	48.8	72.8	96.8	135.4
	2		24.5	48.5	72.5	111.1
	3			24.2	48.2	86.5
	4				24.0	62.3
	5					38.3

UCS (MPa)

		Model Stage				
		5	7	9	11	13
Jet grout set	1	3.40	4.70	5.34	5.78	6.28
	2		3.42	4.68	5.33	5.98
	3			3.40	4.68	5.61
	4				3.38	5.09
	5					4.28

E (MPa)

		Model Stage				
		5	7	9	11	13
Jet grout set	1	678	860	948	1007	1075
	2		681	858	947	1035
	3			678	857	984
	4				674	915
	5					803